UCLA
UCLA Electronic Theses and Dissertations

Title
Synthesis and Assembly of Pt-based Nanocrystals and the Mechanism Study

Permalink
https://escholarship.org/uc/item/3fm6p1bx

Author
Zhu, Enbo

Publication Date
2017

Peer reviewed|Thesis/dissertation

eScholarship.org Powered by the California Digital Library
University of California

UNIVERSITY OF CALIFORNIA

Los Angeles

Synthesis and Assembly of Pt-based Nanocrystals and the Mechanism Study

A dissertation submitted in partial satisfaction of the requirements for the degree Doctor of Philosophy in Materials Science and Engineering

by

Enbo Zhu

2017

© Copyright by

Enbo Zhu

2017

ABSTRACT OF THE DISSERTATION

Synthesis and Assembly of Pt-based Nanocrystals and the Mechanism Study

by

Enbo Zhu

Doctor of Philosophy in Materials Science and Engineering

University of California, Los Angeles, 2017

Professor Yu Huang, Chair

The design and synthesis of multicomponent Pt-based nanomaterials with highly controlled structures have attracted extensive research attention, mainly due to their highly active catalytic properties. The performance enhancement of these catalytic systems largely requires the precise control over the structure with the lowest Pt amount yet high activity to mitigate the high cost of Pt-based nanomaterials. Specific surfactant molecules have been widely employed to manipulate the morphologies and assemblies of nanostructures. Thus rational designs of the surfactants become very significant. In nature, a lot of biomaterials evolved well-developed nanostructures with unique properties through long-time natural selection using biomolecules as the surfactant. Compared with traditional trial-and-error design, biomimetic design

provides more rational controls leading to new synthetic design for nanostructures. In this thesis, synthesis and assembly of Pt-based nanocrystals and the mechanisms were studied.

Chapter 2 introduces one-step synthesis of single-crystal PtNi octahedron with in situ developed highly concave feature and self-confined composition was studied which is optimal for oxygen reduction reaction (ORR). The combination of Ni facet segregation and oxygen etching of Ni-rich surface lead to the concave feature and confined Ni content. The concave PtNi nanocrystal exhibited a very high activity as well as a remarkable stability in ORR.

Chapter 3-4 explores biomimetic approaches to achieve functional Pt nanostructures and their hierarchical assembly. In Chapter 3 a rational designed peptide was utilized to prepare an ultrathin Pt multiple-twinned nanowire network (MTNN) as an efficient electrocatalyst. In Chapter 4 we further demonstrate a biomimetic approach to explore the impact of higher order structures of surfactants on NC formation and alignment. Results show that at low concentration T7 peptide molecules (Ac-TLTTLTN-$CONH_2$) form ST-turns and benefit the selective formation of cubic Pt NCs, and that β-sheets favored under high concentration readily promote linear self-assembly of the cubic NCs along [100] direction. Tailoring the formation conditions of the secondary structures of biomolecules can realize better tuning of peptide concentration controlled NC behaviors via a process that is analogous to biological regulations in

organisms. Great potential in regulating *in vivo* performance of non-biological substances and derived applications become possible.

The dissertation of Enbo Zhu is approved.

Yang Yang

Richard B. Kaner

Xiangfeng Duan

Yu Huang, Committee Chair

University of California, Los Angeles

2017

Table of contents

Acknowledgments..... xiii

Biography.....xvii

Chapter 1 General Introduction 1

Pt-based nanocrystals as catalyst 1

Biomimetic Synthesis 3

Rational selected peptides as surfactant.....4

References.....5

Chapter 2 In situ development of highly concave and compositionconfined PtNi octahedra with high oxygen reduction reaction activity and durability.....14

Introduction.....14

Results and Discussions.....16

Summary 35

Experimental Details.....36

References.....40

Chapter 3 Biomimetic synthesis of an ultrathin platinum nanowire network with a high twin density for enhanced electrocatalytic activity and durability 49

Introduction.....49

Results and Discussions.....50

Summary 65

Experimental Details.....66

References 70

Chapter 4 Anisotropic nanocrystal growth and assembly driven by molecular structural transformation 77

Introduction 77

Results and Discussions 77

Summary 110

Experimental Details 111

References 118

Figure 1.1 Specific peptide sequences selections of T7, S7 and BP7A. 5

Figure 2.1 18

Figure 2.2 The TEM images and illustrative models of the same concave octahedron nanocrystal from different directions. 19

Figure 2.3 19

Figure 2.4 The TEM images of nanocrystals synthesized under different temperature 21

Figure 2.5 The TEM images of nanocrystals synthesized with different citric acid input 21

Figure 2.6 The TEM image of nanocrystals synthesized with Ni/Pt input ratio reduced to 1:8.....21

Figure 2.7 Time evolution of concave octahedron and the composition of Ni in the final PtNi product after different reaction times. 22

Figure 2.8 24

Figure 2.9 25

Figure 2.10 25

Figure 2.11 The TEM images of nanocrystals synthesized with different NaBr input 26

Figure 2.12 The TEM image of nanocrystals grown 8 hours under a typical synthetic condition but without NaBr, using seeds generated after a 4-hours reaction in a typical synthesis. 27

Figure 2.13 The TEM image of nanocrystals grown 8 hours under a typical

synthetic condition but in nitrogen atmosphere, using seeds generated after a 4-hours reaction in a typical synthesis. 27

Figure 2.14 27

Figure 2.15 A schematic diagram demonstrating the growth mechanism of the highly concave PtNi octahedron 28

Figure 2.16 The compositions and TEM images of concave octahedron with different Ni/Pt input ratio. 29

Figure 2.17 The TEM image of concave nanocrystal well dispersed on Vulcan XC72R carbon. 31

Figure 2.18 31

Table 1 Comparison of compositions, sizes and ORR activities[a] for different Pt-Ni alloy catalysts 32

Figure 2.19 ORR polarization curves of concave octahedron/C (c-Oct/C) before and after 10000 potential cycles 34

Figure 2.20 TEM images of concave octahedron/C (c-Oct/C) before and after 10000 potential cycles 34

Figure 2.21 35

Figure 3.1 54

Figure 3.2 56

Figure 3.3 57

Figure 3.4 Pt nanoparticles synthesized at various BP7A peptide concentrations 57

Figure 3.5 TEM image of Pt MTNN loading onto carbon black. 59

Figure 3.6 59

Figure 3.7 Polarization curves of JM Pt/C and Pt MTNN catalysts 61

Figure 3.8 61

Figure 3.9 CV curves of JM Pt/C before and after accelerated durability test. 63

Figure 3.10 63

Figure 3.11 HRTEM images of Pt MTNN after accelerated durability test..... 64

Figure 3.12 65

Figure 4.1 79

Figure 4.2 T7 adopts ST-turns under low concentration..... 80

Figure 4.3 Raman spectroscopies and Fourier self-deconvolution (FSD) processed Fourier transform infrared spectroscopies (FTIR) of T7 in different states..... 82

Figure 4.4 Positive correlation of the amounts of ST turns and TLT units. 83

Figure 4.5 NC morphologies change from cubic to cuboctahedral and the turn structure fades as temperature increases. 86

Figure 4.6 Illustration of the impacts of peptide primary structure to peptide HOS conformation and NC morphology. 87

Figure 4.7 Simulated T7 variants' structures relaxed on Pt {100} facets. Distances between N and O in the hydrogen bonds are represented with red dashed lines. 88

Figure 4.8 T7 serving as templates to directionally align NCs in the <100> direction. 90

Figure 4.9 Superstructures of NCs incubated in 500 μg/mL T7 under different pH. 92

Figure 4.10 Time evolution study indicates how the 1-D assemblies are formed during the annealing process from 45 ºC to 20 ºC in 2 hours. 93

Figure 4.11 Cryo-TEM images, statistical data, and a slide model showing NCs assemble in solution and can move along one-dimensionally the linear assemblies as in a T7 β-sheets slideway. 94

Figure 4.12 96

Figure 4.13 96

Figure 4.14 Comparison of T7 secondary structures on Pt-{100} surfaces. 99

Figure 4.15 Representative snapshots of the first layer of peptides on Pt-{100} surface after relaxation in the simulation of perpendicular β-sheets. 100

Figure 4.16 Preferred conformation of T7 molecules between Pt NCs of a 1-D assembly. 101

Figure 4.17 Alternative T7 conformations between Pt NCs from the initial to the equilibrated states in the direction of 1D assembly. 101

Figure 4.18 Zoom-in snapshots showing the change of alternative T7 conformations between Pt NCs from the initial to the equilibrated states. 103

Figure 4.19 ST turns on NC surfaces are necessary for assembly in 800 μg/mL T7. 104

Figure 4.20 The T7 assembly method extended to Au and Pd NC systems. 105

Table 1: Molecular dynamics simulation of T7 adsorption energies 108

Table 2: Schematics of different situations from start units to 1-D assembly.....109

Figure 4.21 Method of determining the adsorption energy between two β-strands in the β-sheet. 115

Figure 4.22 Method of determining the adsorption energy between peptides.....116

Acknowledgments

It is such a pleasure to be a Ph.D student in the Department of Material Science and Engineering and work under the guidance of Prof. Yu Huang. I really appreciate the help she gave me these years. She gave me a lot of support and showed great patience when I just started my Ph.D research. Her broad knowledge and deep insight to science help me solve lots of problems I met in research. Her judicious advices keep me on the big picture of science (maybe not as big as she wants me to have, but much bigger than what I had before). She gave me freedom to generate my own ideas and encouraged me to go for them. Even for the ideas she did not think would work, she still supported me. At the same time if I need help, she always gave me suggestions without hesitation to extricate me from the predicament. Her patience and advices gave me encouragement and confidence to pursue deeper in science. As a mentor, I benefit not only in research but also in my life. I got many suggestions on my career plan and got encouraged when I met grief in my life. I really appreciate what she did for me these years.

I want to thank my thesis committee: Prof. Xiangfeng Duan, Prof. Richard B. Kaner and Prof. Yang Yang. Prof. Duan gave me a lot of advices in my research. Prof. Kaner showed great patience when I have questions about Chemistry and taught me a lot. Prof. Yang Yang not only gave me suggestions on research but also shared the

philosophy on my life and future. I appreciate their time on my qualification, defense, study, research and life.

I want to thank my grandparents with whom I grew up with. They showed me how to be a kind person. They supported me on my goal to be a scientist all the time. Although they passed away 3 years ago, I can still see them sometimes in my dreams and I get power from them. Maybe in the future I will not be a successful person, but I will be a good person they wanted me to be! I also want to thank my parents. It is their encouragement and advice make me clear about what I should do and what I want to do. I wish them in good health all the time. I want to thank my wife, Gege Wang. She sacrificed so much for me and supported me so much in my life. I wish her good health and wish our love can last forever.

I want to thank all my colleagues in Professor Huang and Professor Duan's groups. Dr. Yujing Li is the senior student I worked with at the beginning of my Ph.D research. He helped me so much that it is influential on my whole career and life. I also appreciate Dr. Chin-Yi Chiu's kind suggestions on my research. Dr. Xiaoqing Huang is such an experienced researcher and I learnt a lot from him. Dr. Lingyan Ruan taught me a lot and gave me a lot of help at the beginning of my Ph.D research. At that time I did not notice how significant it is, but now I realize its influence and I appreciate it very much. I appreciate Dr. Yu Chen teaching me the TEM. It helps me a lot in my research. Dr. Yongjia Li is a trustworthy friend and we supported each other

on many things in these years. Dr. Shan Jiang and Dr. Rui Cheng are reliable seniors and friends. I learnt a lot from them and I really enjoyed eating with Dr. Rui Cheng. Dr. Yuan Liu is an interesting friend. We cooperated a lot on research and shared our happiness in life. No matter how sad I am he can always cheer me up. He also gave me a lot of suggestions, although many of them were proved to be wrong. Mr. Mufan Li also helped me a lot and I love his dog Simon. Dr. Chen Wang supported me so much in my research. I also want to thank Xucheng Yan. He is very young, easy to communicate and responsible. He helped me a lot in the research at the end of my Ph.D study. Other friends like Jianjin Dong, Hao Wu, Dr. Hung-Chieh Cheng, Jian Guo, Dr. Dehui Li, Dr. Gongming Wang, Huiying Shiu, Sen Yang, Yiliu Wang, Qiao Su, Dr. Zipeng Zhao, Dr. Zhaoyang Lin, Dr. Teng Xue, Dr. Nathan Weiss and many others, have all helped me a lot in my research and life. It is a very happy and memorable experience working with you all.

Besides people in our group, I want to thank Ruining Wang, Yue Zhao, Dr. Chao Liu, Dr Qi Chen, Dr. Jinda Zhuang, Chezheng Cao, Dr. Wei Zhang, Dr. Chao Li, Dr. Pei Zhang, Dr Zhi Ren, Dr. Xiaoxing Lu, Dr. Huier Gao, Dr. Pengyu Sun Dr. Li Li and Prof. Yi Tang. I really enjoyed the time I spent with you and appreciate your help on my research and life. I appreciate Prof. Yung-Ya Lin who encourages me a lot in his class and in my life. I want to thank the Life Science core office for providing me great opportunities as teaching assistant. I enjoy the time I worked as teaching assistant with Prof. Stacie Nakamoto, Prof. Rana Khankan and Prof. Amy Fluitt. I

want to thank my collaborators, Prof. Hendrik Heinz and Shiyi Wang for the help in simulation. Without them, many results cannot be interpreted quantitatively.

Lastly, I want to thank the aid I got, including the National Science Foundation, the Office of Naval Research, U.S. Department of Energy, Office of Basic Energy Sciences, Division of Materials Science and Engineering. And I appreciate UCLA facilities like California NanoSystems Institute and Molecular Instrument Center. I also want to say thank you to all the professors in different departments who ever taught me.

Enbo Zhu

University of California, Los Angeles

September 2017

Biography

Enbo Zhu received his B.S. degrees in both Chemistry and Biotechnology from Jilin University, China in 2011. He received Honorable Mention (top 30% in all the qualified teams of the world) in the Mathematical Contest in Modeling, the Consortium for Mathematics and its Applications in 2011. He then joined the Ph.D. program in Materials Science and Engineering at University of California, Los Angeles. He conducted research under the guidance of Prof. Yu Huang on synthesis, assembly and applications of Pt-based nanocrystals and especially on the fundamental mechanism study of nanocrystal synthesis and assembly. He authored and co-authored nineteen papers in peer reviewed journals during his graduate study. His research interests include nanocrystals, biomimetic syntheses, organic-inorganic interface, nanocrystal assembly and related applications.

Chapter 1 General Introduction

Pt-based nanocrystals as catalyst

Nanocrystals are defined as crystals with one or more dimension between 1 and 100 nm.[1] The size of nanocrystals is between atomic and macroscopic scale, they have shown unique optical, electronic, and magnetic properties, drawing a lot of attentions.[2-5] Those properties are determined by the composition, size and shape.[6-8] Among different composition, metallic nanocrystals are very promising since most elements belong to metal. The typical structures of metallic crystals are cubic close-packed or face-centered cubic, which is simple and easy to characterize. By finely tuning the size and shape of metal nanocrystals, the properties can be controlled. Therefore, a lot of attentions were paid to the controlled synthesis of metal nanocrystals.

Metal nanocrystals based on Pt have attracted tremendous research attention owing to their broad applications, including highly active catalysts in chemical reactions, sensors, and electrocatalytic catalysts in fuel cells.[9-14] Among various applications, fuel cells are considered as a potential power source for automotives and portable electronic devices.[15,16] However, the promise of their practical application is heavily hindered by the high usage and cost of Pt in the cathode catalysts and the slow kinetics of oxygen reduction reaction.[17-19] Therefore, it is highly desirable to develop effective strategies for preparing cathode electrocatalysts with largely reduced content

of Pt while still showing superior performance.[9,10]

One effective technique to improve the activity of cathode electrocatalysts is to partially substitute Pt with a secondary metal.[20,21] Bimetallic nanostructures with a lower content of expensive Pt metal can not only inherit the properties of the Pt constituent but also usually show a superior performance when compared with monometallic Pt nanostructures.[20,21] Accordingly, significant progress has been made in the controlled synthesis of bimetallic Pt-based electrocatalysts with a wide range of compositions, such as PtPd, PtAu, PtAg, PtCu, PtFe, PtNi, and PtMn.[22-36] Pt-based bimetallic nanocrystals usually show improved activity compared with their pure Pt counterparts.[20,21] Among various reported Pt-based bimetallic nanostructures, bimetallic PtNi nanocrystals represent an emerging class of newly discovered electrocatalysts that exhibit exciting oxygen reduction reaction activity.[20,22,23,32-34] Stamenkovic and co-workers reported that the (111) surface of Pt_3Ni (bulk single crystal) exhibits an extremely high oxygen reduction reaction activity that is 10-fold higher than Pt(111) and 90-fold higher than the commercial Pt/C catalysts,[20] a pioneering work that has triggered great efforts in the development of controllable PtNi synthesis.[22,23,32-34] Despite the above successful demonstrations, it should be pointed out that the majority of PtNi nanostructures that have been prepared to date are polyhedral nanocrystals and the particle sizes are still relatively large, which are however not beneficial for further improving the utilization efficiency of Pt atoms. Furthermore, the electrochemical durability of this kind of PtNi nanocrystals is even

rarely studied. Therefore, the synthesis of PtNi nanocrystals with enhanced catalytic activity and utilization efficiency is still costly and far from trivial.

Biomimetic Synthesis

The organic-inorganic interface in various systems has been a subject of intense research interest and can impact a wide range of applications from syntheses, catalysis, sensing to energy devices. In colloidal nanocrystal syntheses, one important key to achieve desired shape control is the use of organic surfactants that can judiciously stabilize NC surfaces.[37-39] Under this guidance, a number of surfactants have been explored to manipulate NC shapes and further to construct sophisticated architectures.[40-44] However, mechanisms regarding the selective adsorption of surfactants remain unclear, which limit the choice of suitable surfactants.[37-39] During the past decade, molecular evolution approaches borrowed from biochemistry render useful tools to identify artificial biomolecules with exquisite recognition properties to a variety of material surfaces therefore enriching the pool of surfactants for material fabrication and functionilization.[14,45-51] Nevertheless, most efforts have been focused on identifications and utilizations of biomolecules, while the fundamental investigation of interactions between biomolecules and materials represents a formidable task that has been less touched upon due to the complexity of the system.[52-54]

Recently, more attention has been directed to the inspection of biomolecular behavior at various material surfaces and interfaces including specific surface binding and self-assembly processes.[55,56] Despite extensive studies and various evidence, one of the key questions regarding how biomolecules recognize specific materials and crystal facets still exists in biomimetics.[52-54,57] The development of the state-of-the-art interface detection techniques greatly aid the studies on organic-inorganic interfaces,[58] however, great challenges remain including the complexity and the inaccessibility of the interface, for example, the multifunctionality of the molecules and the distinct atomic coordination on different material surface or crystal facets. Clarifications are often possible using simulation techniques in which interfaces can be well-defined, although reliable insight also strongly depends on the availability of robust binding couples as well as suitable interaction potentials for organic-inorganic interfaces.[59]

Rational selected peptides as surfactant

Peptides were selected though biopanning with a phage display technique.[14,60] Peptide BP7A (Thr-Leu-His-Val-Ser-Ser-Tyr) was selected towards a 0.25mm diameter, 99.99% pure platinum wire.[60] Pt{100} binding peptide T7 (Thr-Leu-Thr-Thr-Leu-Thr-Asn) and a Pt{111} binding peptide S7 (Ser-Ser-Phe-Pro-Glu-Pro-Asp) were selected towards Pt nanocubes (exclusively {100} facet enclosed) and nanotetrahedra (exclusively {111} facet bounded) respectively.[14] As predicted, T7 and S7 show the ability to exclusively produce Pt nanocubes and nanotetrahedra. The peptide selection

process was shown in Figure 1.1.

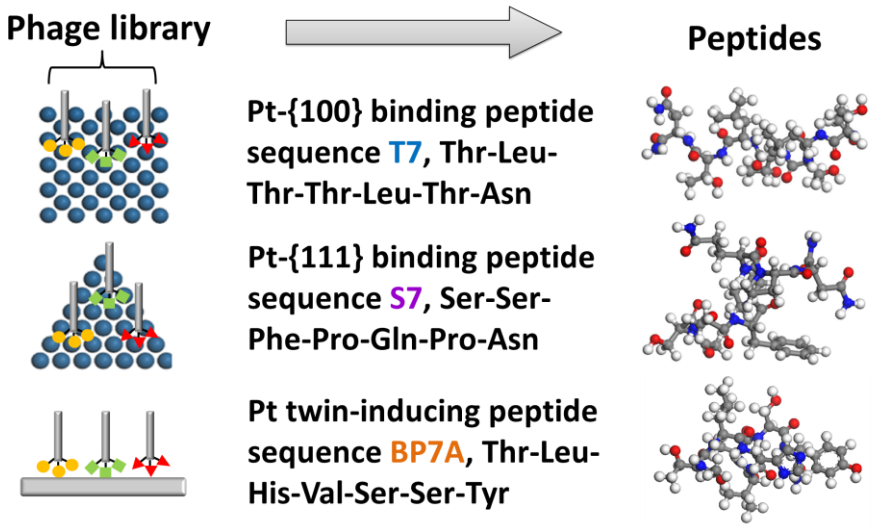

Figure 1.1 Specific peptide sequences selections of T7, S7 and BP7A.

In my PhD research, the synthesis (Chapter 2-4) and assembly (Chapter 3 and 4) of Pt-based nanocrystals and the mechanism were studied. In the synthesis, both conventional solvothermal methods (Chapter 2) and rationally designed biomimetic methods (Chapter 3 and 4) were used. Moreover, a higher catalytic activity (Chapter 2 and 3) as well as a deeper understanding of the mechanism involved in the synthesis (Chapter 2) and assembly (Chapter 4) were pursued.

References

1. Fahlman, B. D. (2011). Nanomaterials. In *Materials Chemistry* (pp. 457-583). Springer Netherlands.
2. Avouris, P., Chen, Z., & Perebeinos, V. (2007). Carbon-based electronics. *Nature nanotechnology*, *2*(10), 605-615.

3. Nozik, A. J. (2010). Nanoscience and nanostructures for photovoltaics and solar fuels. *Nano letters*, *10*(8), 2735-2741.
4. Xia, Y., Yang, P., Sun, Y., Wu, Y., Mayers, B., Gates, B., ... & Yan, H. (2003). One‐dimensional nanostructures: synthesis, characterization, and applications. *Advanced materials*, *15*(5), 353-389.
5. Lohse, S. E., & Murphy, C. J. (2012). Applications of colloidal inorganic nanoparticles: from medicine to energy. *Journal of the American Chemical Society*, *134*(38), 15607-15620.
6. Lu, G., Li, H., & Zhang, H. (2012). Gold‐Nanoparticle‐Embedded Polydimethylsiloxane Elastomers for Highly Sensitive Raman Detection. *Small*, *8*(9), 1336-1340.
7. Zhou, K., & Li, Y. (2012). Catalysis Based on Nanocrystals with Well‐Defined Facets. *Angewandte Chemie International Edition*, *51*(3), 602-613.
8. Chen, H., Shao, L., Li, Q., & Wang, J. (2013). Gold nanorods and their plasmonic properties. *Chemical Society Reviews*, *42*(7), 2679-2724.
9. Chen, A., & Holt-Hindle, P. (2010). Platinum-based nanostructured materials: synthesis, properties, and applications. *Chem. Rev*, *110*(6), 3767-3804.
10. Peng, Z., & Yang, H. (2009). Designer platinum nanoparticles: Control of shape, composition in alloy, nanostructure and electrocatalytic property. *Nano Today*, *4*(2), 143-164.
11. Larsson, E. M., Langhammer, C., Zorić, I., & Kasemo, B. (2009). Nanoplasmonic probes of catalytic reactions. *Science*, *326*(5956), 1091-1094.

12. Tian, N., Zhou, Z. Y., Sun, S. G., Ding, Y., & Wang, Z. L. (2007). Synthesis of tetrahexahedral platinum nanocrystals with high-index facets and high electro-oxidation activity. *science*, *316*(5825), 732-735.
13. Lim, B., Jiang, M., Camargo, P. H., Cho, E. C., Tao, J., Lu, X., ... & Xia, Y. (2009). Pd-Pt bimetallic nanodendrites with high activity for oxygen reduction. *science*, *324*(5932), 1302-1305.
14. Chiu, C. Y., Li, Y., Ruan, L., Ye, X., Murray, C. B., & Huang, Y. (2011). Platinum nanocrystals selectively shaped using facet-specific peptide sequences. *Nature chemistry*, *3*(5), 393-399.
15. Winter, M., & Brodd, R. J. (2004). What are batteries, fuel cells, and supercapacitors. *Chem. Rev.*, *104*(10) , 4245-4270.
16. Dresselhaus, M. S., & Thomas, I. L. (2001). Alternative energy technologies. *Nature*, *414*(6861), 332.
17. Gasteiger, H. A. & Markovic, N. M. (2009). Just a Dream-or Future Reality? *Science*, *324*(5923), 48-49.
18. Gasteiger, H. A., Kocha, S. S., Sompalli, B., & Wagner, F. T. (2005). Activity benchmarks and requirements for Pt, Pt-alloy, and non-Pt oxygen reduction catalysts for PEMFCs. *Applied Catalysis B: Environmental*, *56*(1), 9-35.
19. De Bruijn, F. A., Dam, V. A. T., & Janssen, G. J. M. (2008). Durability and degradation issues of PEM fuel cell components. *Fuel cells*, *8*(1), 3-22.
20. Stamenkovic, V. R., Fowler, B., Mun, B. S., Wang, G., Ross, P. N., Lucas, C. A., & Marković, N. M. (2007). Improved oxygen reduction activity on Pt_3Ni (111) via

increased surface site availability. *science*, *315*(5811), 493-497.

21. Greeley, J., Stephens, I. E. L., Bondarenko, A. S., Johansson, T. P., Hansen, H. A., Jaramillo, T. F., ... & Nørskov, J. K. (2009). Alloys of platinum and early transition metals as oxygen reduction electrocatalysts. *Nature chemistry*, *1*(7), 552-556.
22. Wu, J., Gross, A., & Yang, H. (2011). Shape and composition-controlled platinum alloy nanocrystals using carbon monoxide as reducing agent. *Nano letters*, *11*(2), 798-802.
23. Zhang, J., & Fang, J. (2009). A general strategy for preparation of Pt 3d-transition metal (Co, Fe, Ni) nanocubes. *Journal of the American Chemical Society*, *131*(51), 18543-18547.
24. Kang, Y., & Murray, C. B. (2010). Synthesis and electrocatalytic properties of cubic Mn-Pt nanocrystals (nanocubes). *Journal of the American Chemical Society*, *132*(22), 7568-7569.
25. Kim, J., Lee, Y., & Sun, S. (2010). Structurally ordered FePt nanoparticles and their enhanced catalysis for oxygen reduction reaction. *Journal of the American Chemical Society*, *132*(14), 4996-4997.
26. Xu, D., Liu, Z., Yang, H., Liu, Q., Zhang, J., Fang, J., ... & Sun, K. (2009). Solution‐Based Evolution and Enhanced Methanol Oxidation Activity of Monodisperse Platinum–Copper Nanocubes. *Angewandte Chemie International Edition*, *48*(23), 4217-4221.
27. Chen, J., Wiley, B., McLellan, J., Xiong, Y., Li, Z. Y., & Xia, Y. (2005). Optical

properties of Pd-Ag and Pt-Ag nanoboxes synthesized via galvanic replacement reactions. *Nano letters*, *5*(10), 2058-2062.

28. Peng, Z., & Yang, H. (2009). Synthesis and oxygen reduction electrocatalytic property of Pt-on-Pd bimetallic heteronanostructures. *Journal of the American Chemical Society*, *131*(22), 7542-7543.
29. Wang, L., Nemoto, Y., & Yamauchi, Y. (2011). Direct synthesis of spatially-controlled Pt-on-Pd bimetallic nanodendrites with superior electrocatalytic activity. *Journal of the American Chemical Society*, *133*(25), 9674-9677.
30. Teng, X., Feygenson, M., Wang, Q., He, J., Du, W., Frenkel, A. I., ... & Aronson, M. (2009). Electronic and magnetic properties of ultrathin Au/Pt nanowires. *Nano letters*, *9*(9), 3177-3184.
31. Ataee-Esfahani, H., Wang, L., Nemoto, Y., & Yamauchi, Y. (2010). Synthesis of bimetallic Au@ Pt nanoparticles with Au core and nanostructured Pt shell toward highly active electrocatalysts. *Chemistry of Materials*, *22*(23), 6310-6318.
32. Zhang, J., Yang, H., Fang, J., & Zou, S. (2010). Synthesis and oxygen reduction activity of shape-controlled Pt3Ni nanopolyhedra. *Nano Lett*, *10*(2), 638-644.
33. Wu, J., Zhang, J., Peng, Z., Yang, S., Wagner, F. T., & Yang, H. (2010). Truncated octahedral Pt3Ni oxygen reduction reaction electrocatalysts. *Journal of the American Chemical Society*, *132*(14), 4984-4985.
34. Wu, Y., Cai, S., Wang, D., He, W., & Li, Y. (2012). Syntheses of water-soluble octahedral, truncated octahedral, and cubic Pt–Ni nanocrystals and their structure–

activity study in model hydrogenation reactions. *Journal of the American Chemical Society*, *134*(21), 8975-8981.

35. Kuttiyiel, K. A., Sasaki, K., Choi, Y., Su, D., Liu, P., & Adzic, R. R. (2012). Nitride stabilized PtNi core-shell nanocatalyst for high oxygen reduction activity. *Nano letters*, *12*(12), 6266-6271.
36. Sasaki, K., Naohara, H., Choi, Y., Cai, Y., Chen, W. F., Liu, P., & Adzic, R. R. (2012). Highly stable Pt monolayer on PdAu nanoparticle electrocatalysts for the oxygen reduction reaction. *Nature communications*, *3*, 1115.
37. Yin, Y., & Alivisatos, A. P. (2005). Colloidal nanocrystal synthesis and the organic-inorganic interface. *Nature*, *437*(7059), 664.
38. Xia, Y., Xiong, Y., Lim, B., & Skrabalak, S. E. (2009). Shape-controlled synthesis of metal nanocrystals: Simple chemistry meets complex physics? *Angewandte Chemie International Edition*, *48*(1), 60-103.
39. Tao, A. R., Habas, S., & Yang, P. (2008). Shape control of colloidal metal nanocrystals. *small*, *4*(3), 310-325.
40. Zhang, J., Langille, M. R., & Mirkin, C. A. (2010). Photomediated synthesis of silver triangular bipyramids and prisms: the effect of pH and BSPP. *Journal of the American Chemical Society*, *132*(35), 12502-12510.
41. Zhuang, Z., Lu, X., Peng, Q., & Li, Y. (2010). Direct synthesis of water-soluble ultrathin CdS nanorods and reversible tuning of the solubility by alkalinity. *Journal of the American Chemical Society*, *132*(6), 1819-1821.
42. Ye, X., Jin, L., Caglayan, H., Chen, J., Xing, G., Zheng, C., ... & Murray, C. B.

(2012). Improved size-tunable synthesis of monodisperse gold nanorods through the use of aromatic additives. *ACS nano*, *6*(3), 2804-2817.

43. Teng, X., & Yang, H. (2005). Synthesis of platinum multipods: an induced anisotropic growth. *Nano letters*, *5*(5), 885-891.
44. Sau, T. K., & Murphy, C. J. (2004). Room temperature, high-yield synthesis of multiple shapes of gold nanoparticles in aqueous solution. *Journal of the American Chemical Society*, *126*(28), 8648-8649.
45. Aizenberg, J. (2010). New nanofabrication strategies: inspired by biomineralization. *MRS bulletin*, *35*(4), 323-330.
46. Whaley, S. R., English, D. S., Hu, E. L., Barbara, P. F., & Belcher, A. M. (2000). Selection of peptides with semiconductor binding specificity for directed nanocrystal assembly. *Nature*, *405*(6787), 665.
47. Naik, R. R., Stringer, S. J., Agarwal, G., Jones, S. E., & Stone, M. O. (2002). Biomimetic synthesis and patterning of silver nanoparticles. *Nature materials*, *1*(3), 169.
48. Gugliotti, L. A., Feldheim, D. L., & Eaton, B. E. (2004). RNA-mediated metal-metal bond formation in the synthesis of hexagonal palladium nanoparticles. *Science*, *304*(5672), 850-852.
49. Li, Y., & Huang, Y. (2010). Morphology-controlled synthesis of platinum nanocrystals with specific peptides. *Advanced Materials*, *22*(17), 1921-1925.
50. Ruan, L., Chiu, C. Y., Li, Y., & Huang, Y. (2011). Synthesis of platinum single-twinned right bipyramid and {111}-bipyramid through targeted control

over both nucleation and growth using specific peptides. *Nano letters*, *11*(7), 3040-3046.

51. Chung, W. J., Kwon, K. Y., Song, J., & Lee, S. W. (2011). Evolutionary screening of collagen-like peptides that nucleate hydroxyapatite crystals. *Langmuir*, *27*(12), 7620-7628.
52. Slocik, J. M., & Naik, R. R. (2010). Probing peptide-nanomaterial interactions. *Chemical Society Reviews*, *39*(9), 3454-3463.
53. Sanchez, C., Arribart, H., & Guille, M. M. G. (2005). Biomimetism and bioinspiration as tools for the design of innovative materials and systems. *Nature materials*, *4*(4), 277.
54. Vallee, A., Humblot, V., & Pradier, C. M. (2010). Peptide interactions with metal and oxide surfaces. *Accounts of Chemical Research*, *43*(10), 1297-1306.
55. So, C. R., Kulp III, J. L., Oren, E. E., Zareie, H., Tamerler, C., Evans, J. S., & Sarikaya, M. (2009). Molecular recognition and supramolecular self-assembly of a genetically engineered gold binding peptide on Au {111}. *Acs Nano*, *3*(6), 1525-1531.
56. Rothenstein, D., Claasen, B., Omiecienski, B., Lammel, P., & Bill, J. (2012). Isolation of ZnO-binding 12-mer peptides and determination of their binding epitopes by NMR spectroscopy. *Journal of the American Chemical Society*, *134*(30), 12547-12556.
57. Liang, M. K., Deschaume, O., Patwardhan, S. V., & Perry, C. C. (2011). Direct evidence of ZnO morphology modification via the selective adsorption of

ZnO-binding peptides. *Journal of Materials Chemistry*, *21*(1), 80-89.

58. Somorjai, G. A., Frei, H., & Park, J. Y. (2009). Advancing the frontiers in nanocatalysis, biointerfaces, and renewable energy conversion by innovations of surface techniques. *Journal of the American Chemical Society*, *131*(46), 16589-16605.
59. Di Felice, R., & Corni, S. (2011). Simulation of peptide–surface recognition. *The Journal of Physical Chemistry Letters*, *2*(13), 1510-1519.
60. Li, Y., Whyburn, G. P., & Huang, Y. (2009). Specific peptide regulated synthesis of ultrasmall platinum nanocrystals. *Journal of the American Chemical Society*, *131*(44), 15998-15999.

Chapter 2 In situ development of highly concave and compositionconfined PtNi octahedra with high oxygen reduction reaction activity and durability

Introduction

Cost-effective proton exchange membrane fuel cells represent a revolutionary clean energy generation approach, running on hydrogen fuel and air.[1-3] Given their promising potential, substantial research efforts have been devoted in recent years to electrocatalysts in proton exchange membrane fuel cells. Specifically, their cathodic reaction, or the oxygen reduction reactions (ORR), is the key issue since the sluggish reaction kinetics of this step has been long considered a major obstacle to overall fuel cell performance. As discussed in Chapter 1, although a Pt catalyst is a suitable candidate in this application,[4-6] the high cost and scanty reserves of Pt make it imperative to moderate the usage of Pt in the application process while preserving the same or achieving even better activity.[7] Moreover, Pt is criticized for its declining activity over time.[8-14] Both experimental and theoretical studies have revealed that Pt-based bimetallic nanostructures are a possible solution.[15-18] By alloying Pt with a second metallic component, bimetallic nanostructures with less Pt content can not only lead to superior performance compared to monometallic Pt nanostructures,[9, 15, 19-31] but also largely preserve the activity.[32-34] Marković et al. have reported that the Pt-alloy structure showed a better d-band center position, which leads to enhanced ORR activity.[19]

Significant progress has been made in the controlled synthesis of bimetallic Pt-based electrocatalysts with a wide range of compositions.[16, 17, 30, 35-37] Among the different Pt-based bimetallic nanostructures reported, PtNi nanocrystals are well-regarded electrocatalysts with excellent ORR activity.[16, 17, 19, 24, 30, 38] However, the majority of PtNi nanostructures documented to date are convex nanocrystals, which are not optimal for the utilization efficiency of the surface atoms. To achieve improved atom utilization efficiency, a number of unique structures with large surface areas per unit volume, such as porous structures,[25] concave structures,[26,39] and nanoframes,[32] have been developed. Although porous PtNi nanostructures possess more surface active sites, they demonstrate relatively low ORR activity, possibly owing to the indeterminate morphology.[25] Comparatively, PtNi nanoframes show impressive activity and durability simultaneously. Nonetheless, the process involves a separate step to develop the nanoframe from the convex dodecahedron, which makes the overall process time-consuming.[32] Strasser et al. found that PtNi octahedral nanocatalysts can develop a concave shape naturally during electrochemical activation. This transient state is characteristic of outstanding activity but also poor stability, as it will transform either back to an octahedron or to an orthogonal skeleton structure.[27] This makes the utilization of this concave morphology impractical. Therefore, developing a simple synthetic approach to achieve a stable concave PtNi electrocatalyst with superb ORR activity and stability is of great importance.

Herein, we report a highly concave PtNi nanocrystal obtained through a facile one-pot

synthesis method. Our study revealed the following findings. First, unlike most nanocrystals, which are convex, the synthesized octahedra adopted an *in situ*-developed concave structure. The concave structure, compared to the convex ones, gave rise to a high surface area per volume and excellent utilization efficiency of metal atoms. Secondly, the concave PtNi octahedra exhibited very high activity owing to the exposed high-index facets. Thirdly, the catalyst demonstrated very high stability in the accelerated durability test, and maintained the concave morphology, in contrast to the fast deterioration reported previously.[26] Interestingly, the Ni content in the concave octahedra was selfconfined to ~44% even with higher Ni precursor dosages or prolonged reaction times, which was within the optimal range (40%–50%) to achieve high ORR activity for a PtNi octahedron.[26, 40–42]

In a typical synthesis, equimolar amounts of $Pt(acac)_2$ (acetylacetonate) and $Ni(acac)_2$ were mixed with citric acid and sodium bromide (NaBr) in N,N-dimethylformamide (DMF). The resulting homogeneous solution was transferred to a 30 mL vial, which was then sealed and heated at 155 °C for 12 h in an air atmosphere. The resulting products were collected by centrifugation and washed several times with ethanol.

Results and Discussions

The representative transmission electron microscope (TEM) image (Figure 2.1a) and High Angle Annular Dark Field-scanning transmission electron microscope

(HAADF-STEM) analysis (Figure 2.1b) of the prepared PtNi nanocrystals show a high yield concave morphology (nearly 100%), with a uniform size distribution of 24±2 nm (inset of Figure 2.1b, the size is defined as the distance between the two most remote vertices). The composition is determined as $Pt_{56}Ni_{44}$ by examining 6 parallel experiments (more than 300 nanocrystals in total) using HAADF-STEM-energy dispersive X-ray spectroscopy (HAADF-STEM-EDS). Inductively coupled plasma optical emission spectrometry (ICP-OES) confirms the composition (46.27% Ni and 53.73% Pt). Powder X-ray diffraction (XRD) data (Figure 2.1i) confirms the crystalline structure and the composition of the PtNi concave octahedra (Reference: Pt 00-004-0802, Ni 00-004-0850). The single-crystalline nature of the individual particles is confirmed by high resolution TEM (HRTEM) (Figure 2.1c, Figure 2.1d) and the corresponding fast Fourier transform (FFT) diffraction patterns (Figure 2.1e, Figure 2.1g) from zone axis [110] and [100], respectively. The lattice fringes with interplanar spacings of 0.217 nm and 0.188 nm correspond to {111} planes (Figure 2.1c) and {200} planes (Figure 2.1d) of the face-centered cubic (fcc) PtNi alloy, respectively. The HRTEM images of the same single nanocrystal projected from different directions (Figure 2.1c, Figure 2.1d, Figure 2.2) confirm the proposed structure model. The linear scan profile of a PtNi nanocrystal (Figure 2.1j) and element mapping (Figure 2.3) showing higher Pt and Ni signal from the vertex of the octahedron and lower signal from the concave area, further confirms the concave morphology and suggests a uniform PtNi alloy structure. A rough estimation gives 3.6 times higher surface to volume ratio of the concave

octahedron (1.535 nm^{-1}) than that of the non-concave octahedron with the same size (0.432 nm^{-1}), suggesting improved utilization efficiency of metal atoms in the concave structure.

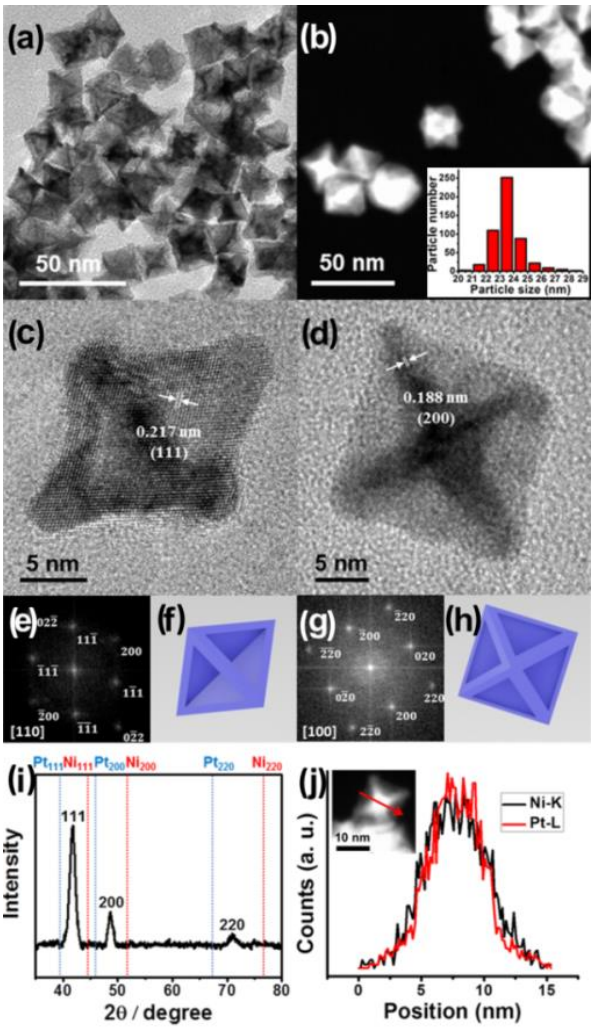

Figure 2.1 (a) and (b) TEM and HAADF images of concave octahedra. The inset shows the size distribution. (c) and (d) HRTEM images of the same individual nanocrystal from zone axis [110] and [100]. (e) and (g) Diffraction patterns after FFT from zone axis [110] and [100]. (f) and (h) Models of concave nanocrystals from zone axis [110] and [100]. (i) X-ray diffraction pattern of the concave nanocrystals. (j) The linear scan profile of an individual concave nanocrystal.

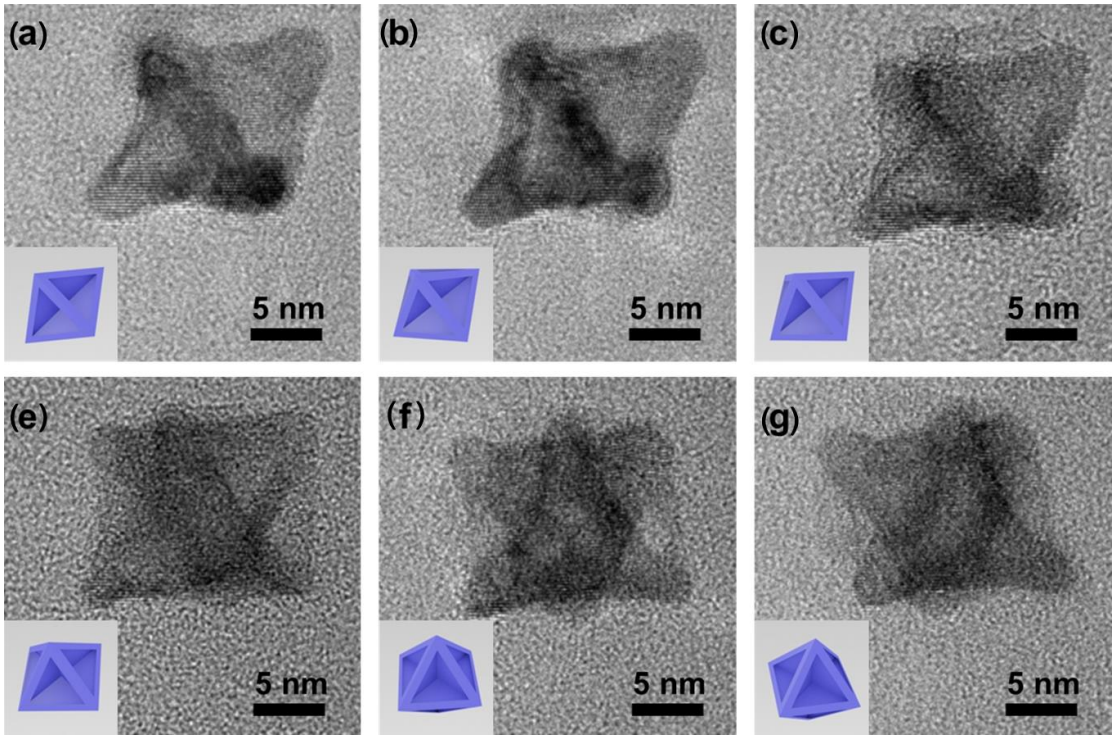

Figure 2.2 The TEM images and illustrative models of the same concave octahedron nanocrystal from different directions.

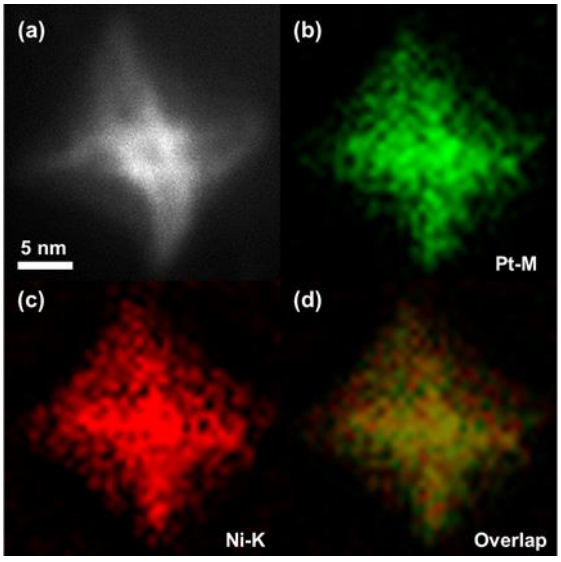

Figure 2.3 (a) The HAADF image of a concave nanocrystal. (b) Element mappings of Pt and (c) element mappings of Ni of the nanocrystal shown in (a). (d) The overlapped element mapping of the nanocrystal shown in (a).

We investigated the influence of different synthesis conditions on the morphology and composition of the PtNi product. First, it was found that lowering temperature from 155 to 150 °C led to not only the loss of concave octahedron morphology, but also the deficiency of Ni in the final product (Figure 2.4). This can be attributed to the difficulty in reducing Ni ions at lower temperatures due to its relatively low redox potential. Similarly decreasing the amount of the reducing agent citric acid, or reducing $Ni(acac)_2$ input, also led to the loss of the concave feature and eventually the octahedron structure (Figure 2.5-2.6); while increment of citric acid led to over-grown morphology of the concave octahedron. In addition the composition plot of the PtNi products (Figure S2.5e) shows that the final Ni content in the products also decreases with decreasing amount of citric acid or $Ni(acac)_2$, confirming Ni is important in maintaing the octahedron morphology. These observations may be explained by the fact that Ni helps stabilize PtNi {111} surfaces, and hence helps produce and maintain the octahedron morphology.[43] Meanwhile, citric acid may play a role as the surfactant molecule to help achieve the octahedron and stabilize the nanocrystals. Without citric acid, the resulting particles seem to adopt irregular shapes and aggregate (Figure 2.5a).

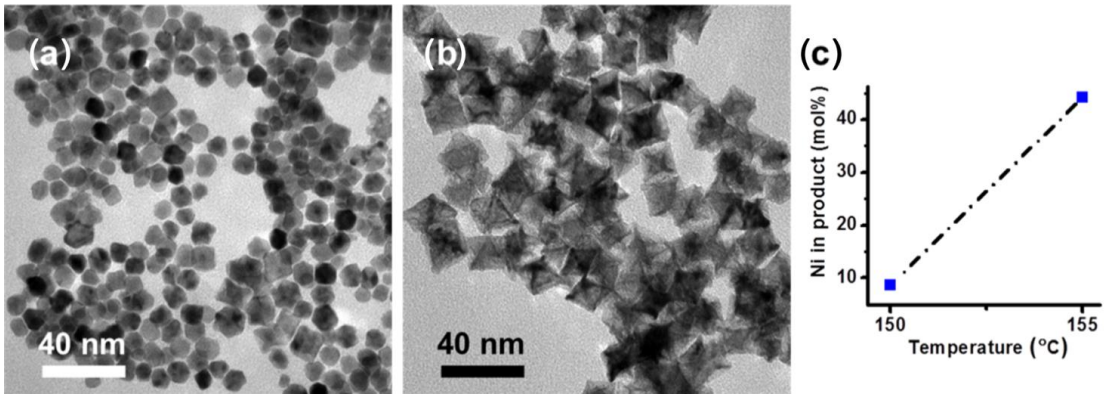

Figure 2.4 The TEM images of nanocrystals synthesized under different temperature: (a) 150 °C, (b) 155 °C. (c) The compositions of nanocrystals synthesized under different temperature.

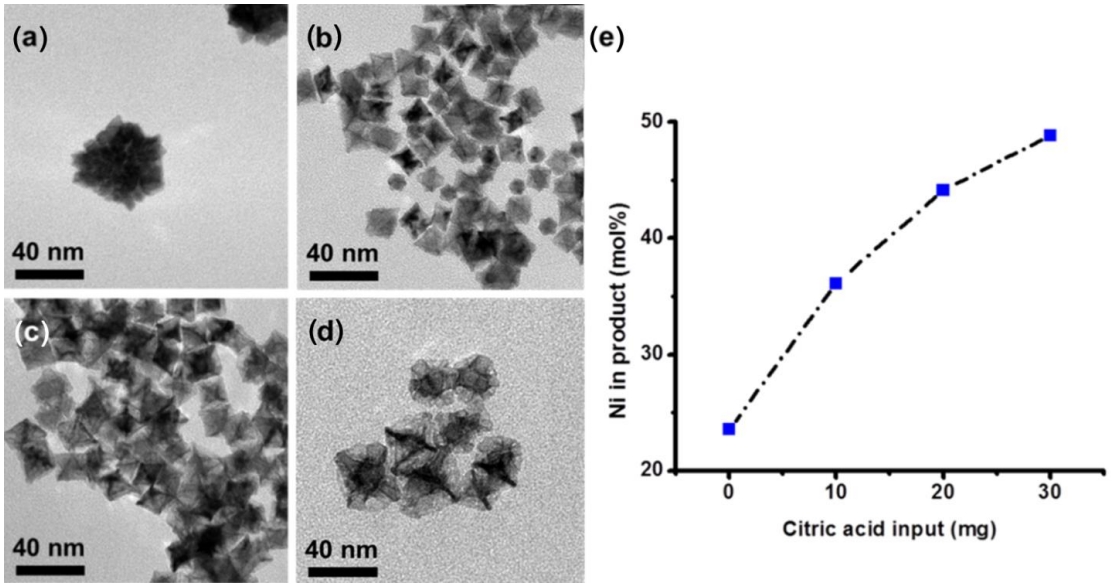

Figure 2.5 The TEM images of nanocrystals synthesized with different citric acid input: (a) 0 mg, (b) 10 mg, (c) 20 mg, (d) 30 mg. (e) The compositions of nanocrystals synthesized with different citric acid input.

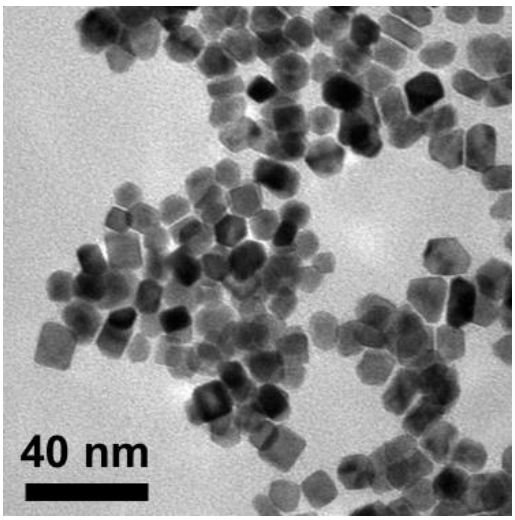

Figure 2.6 The TEM image of nanocrystals synthesized with Ni/Pt input ratio reduced to 1:8 (2.5 mg $Pt(acac)_2$ and 0.2 mg $Ni(acac)_2$).

Furthermore, the nanocrystals produced at different reaction length are collected to trace the development of the concave structure in reaction. Figure 2.7 demonstrates the morphology and composition evolution of the PtNi nanocrystals. It was observed that with growing nanocrystal size, the concave structure gradually developed *in situ*. The plot also indicates that a Pt-rich seed formed first in the seeding stage, probably due to the higher redox potential of Pt^{2+}/Pt (1.188 V) compared to Ni^{2+}/Ni (-0.257 V).[44,45] The Ni content in the nanocrystals reaches 44.16% after 12 hours, and then to 48.66% after 36 hours, approaching the input ratio of Pt and Ni precursors (1:1); and the size of the nanocrystal does not increase much further. These suggest Ni^{2+} is mostly reduced after the formation of Pt-rich seeds, and that the main Ni reduction process happens within the first 12 hours during the growth stage. Though the reduction of Pt and Ni is not concurrent, the elemental distribution of Pt and Ni in final concave nanocrystal is uniform (Figure 2.1j) possibly due to the excellent inter-diffusivity between Pt and Ni and the thermodynamic preference to generate PtNi alloy.[46]

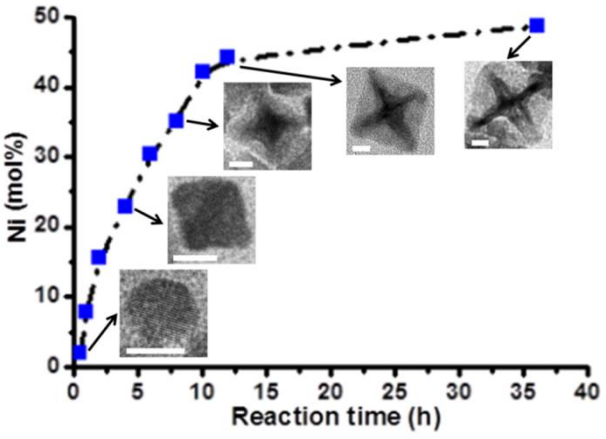

Figure 2.7 Time evolution of concave octahedron and the composition of Ni in the final PtNi product after different reaction times. Scale bars = 5 nm.

Bromide ion (Br^-) and oxygen were found to play important roles in the formation of the concave morphology. Specifically, both of them influence the nucleation process, while oxygen exhibits more profound effect in later growth stage to develop the concave octahedrons. Firstly, it became apparent in our studies that Br^- and oxygen work together to eliminate twinned seeds and promote single crystal growth during the nucleation stage. Without Br^- or oxygen or both, the syntheses yield large quantities of icosahedral twin structures (Figure 2.8-2.9). This can be explained by synergistic effect of halogen ions and oxygen molecules, which effectively etches twin structures during the seeding stage.[47] Replacing NaBr with NaCl in the reaction, where Cl^- can perform the same etching effect as Br^-,[47] led to similarly concave octahedron products as expected (Figure 2.10), confirming this hypothesis. However, though the presence of NaBr plays an important role in seeding, its input amount had little influence on the morphology and composition of the final product, indicating its limited contribution to the growth of the concave structure. (Figure 2.11) To further investigate the roles of Br^- and oxygen during the growth stage, we use the small nanocrystals obtained after 4 hours reaction as seeds, and conduct the growth experiment for another 8 hours without the presence of NaBr or oxygen. Our results showed that without NaBr concave PtNi octahedra were still obtained (Figure 2.12), while in the absence of oxygen PtNi octahedron without concave feature were observed (Figure 2.13). This indicates oxygen is essential in concaving the PtNi octahedron nanocrystals during growth while Br^- is not. PtNi nanocrystals synthesized

without the presence of NaBr at the growth stage generally exhibit high ORR activity due to the clean surface without Br^- binding. Elemental mapping and linear scan profile studies of the distribution of Pt and Ni on a non-concave octahedron (Figure 2.13) showed clearly Ni segregation on the {111} facet (Figure 2.14).[26] This distinctively differs from the concave octahedron, where both Pt and Ni element distribution is uniform (Figure 2.1j). It is believed the Ni-rich segregation on the facet is much less stable than the Pt-rich skeleton, which is then subject to oxidative etching by oxygen.[46] At the same time, the Pt-richer edge maintains relatively faster growth rate, leading to the observed highly concave structure. (Figure 2.15) An atomic model proposed previously based on DFT simulation supports our hypothesis of chemical etching.[39]

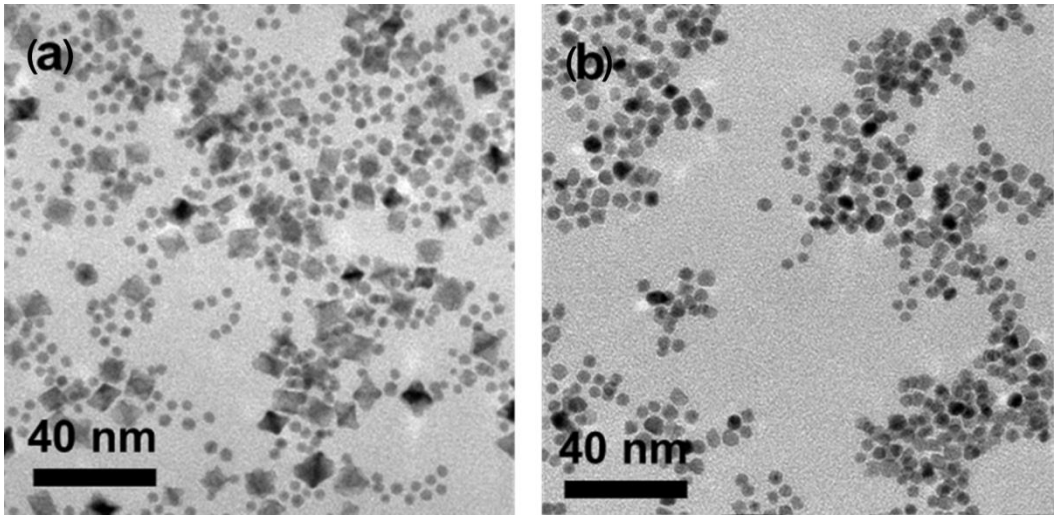

Figure 2.8 The TEM images of nanocrystals synthesized under typical synthetic conditions except that (a) no NaBr was added, (b) no air was introduced and nitrogen protection was adopted.

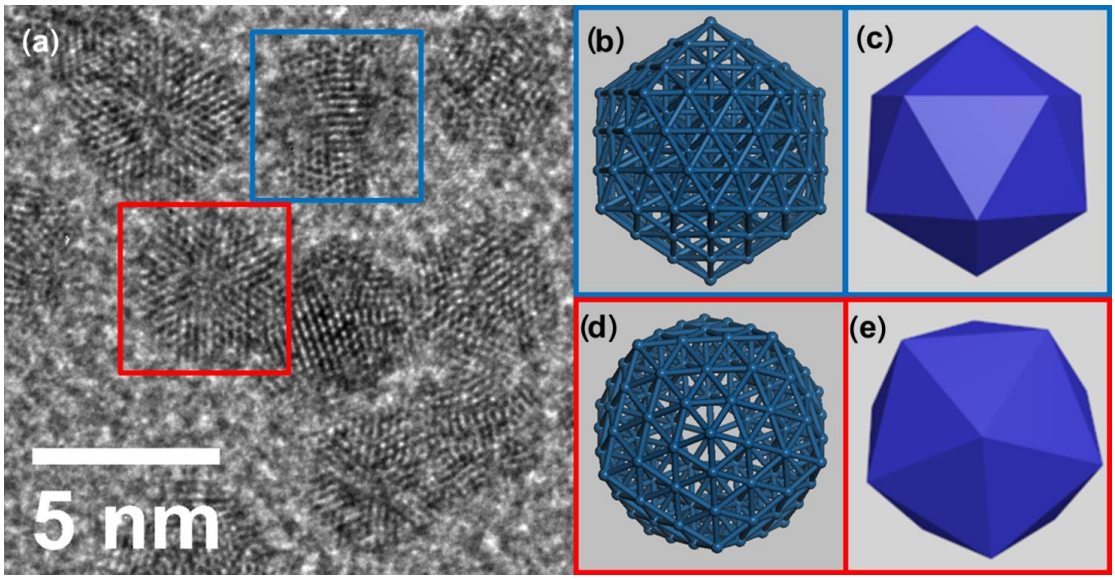

Figure 2.9 (a) The TEM image of typical icosahedra produced under typical synthetic conditions but without NaBr or air (under nitrogen protection). (b,c) and (d,e): Schematics of the icosahedron framed in blue and red in (a) respectively.

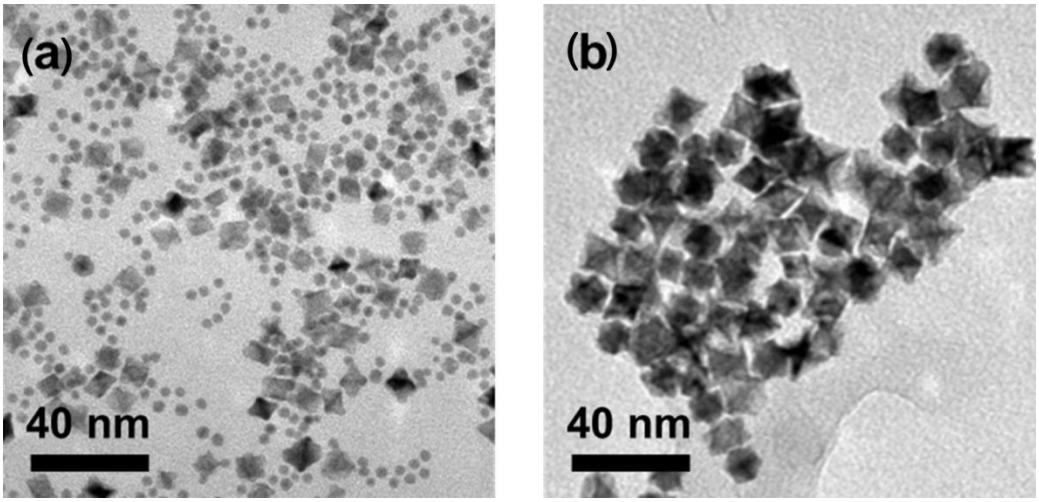

Figure 2.10 The TEM images of nanocrystals synthesized under typical synthetic conditions except (a) with no NaBr or NaCl, and (b) substituting NaBr with saturated NaCl.

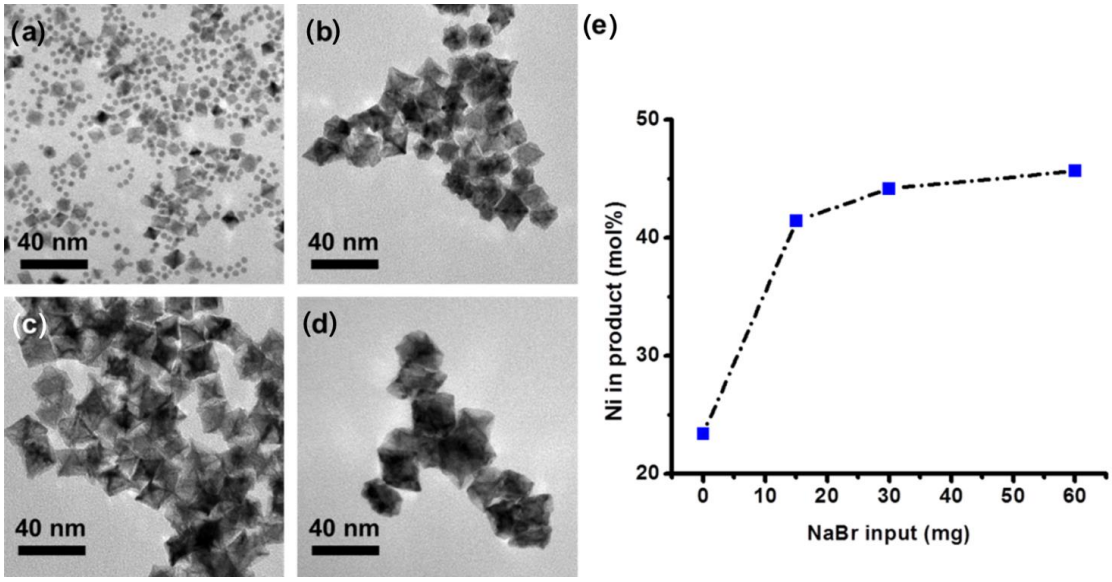

Figure 2.11 The TEM images of nanocrystals synthesized with different NaBr input: (a) 0 mg, (b) 15 mg, (c) 30 mg , (d) 60 mg. (e) The compositions of nanocrystals synthesized with different NaBr input.

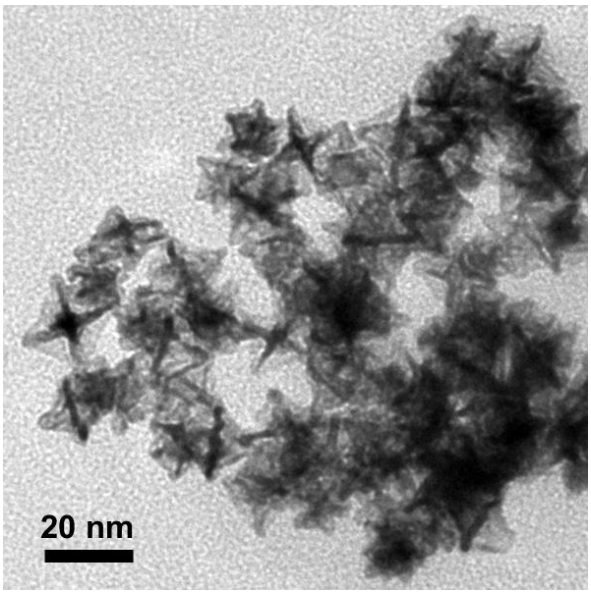

Figure 2.12 The TEM image of nanocrystals grown 8 hours under a typical synthetic condition but without NaBr, using seeds generated after a 4-hours reaction in a typical synthesis.

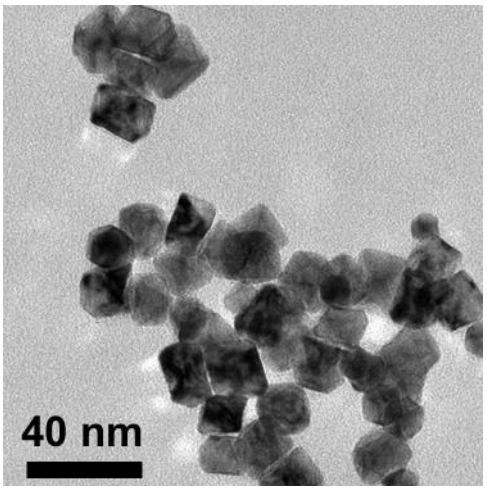

Figure 2.13 The TEM image of nanocrystals grown 8 hours under a typical synthetic condition but in nitrogen atmosphere, using seeds generated after a 4-hours reaction in a typical synthesis.

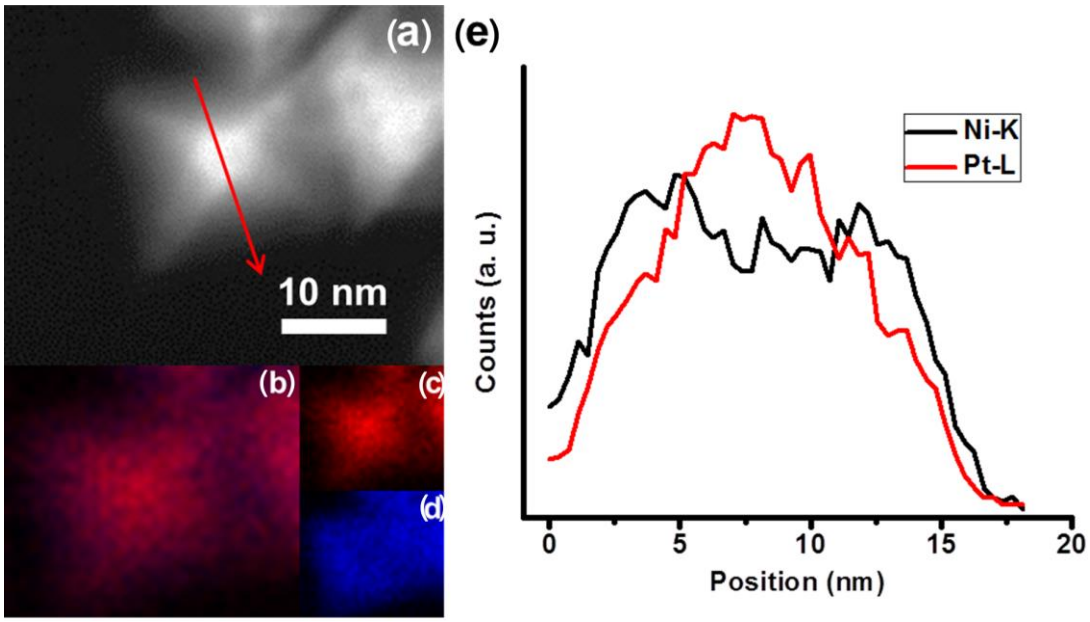

Figure 2.14 (a) The HAADF image of a nanocrystal synthesized under nitrogen protection in the growth stage. (b) The overall element mapping of the nanocrystal shown in (a). (c) Element mappings of Pt and (d) element mappings of Ni of the

nanocrystal shown in (a). (e) The linear scan profile of Pt and Ni following the scan route shown in (a).

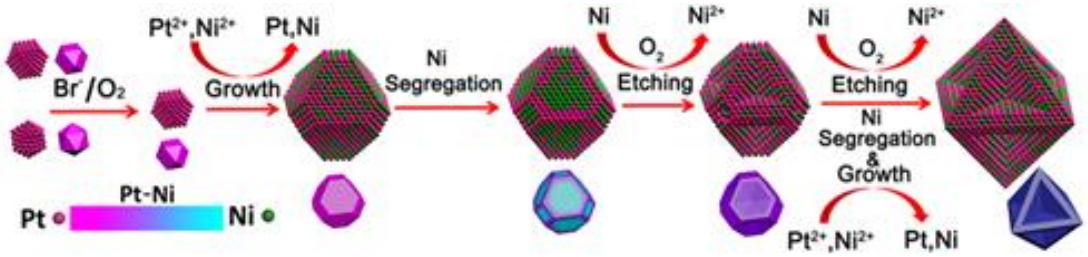

Figure 2.15 A schematic diagram demonstrating the growth mechanism of the highly concave PtNi octahedron, including Pt-rich seeding, Br-/O_2 etching of the twinned seeds, growth of PtNi octahedron, Ni segregation, and the simultaneous oxygen etching of Ni-rich surface and the continued growth of concave PtNi octahedron

Interestingly, it was found that the Ni content in the concave nanocrystals did not exceed about 44% even with sufficient $Ni(acac)_2$ precursor input (Figure 2.16). Coincidently, previous experimental[46] and computational results[48,49] have suggested that PtNi alloy is most stable against phase segregation and oxidative etching when Ni content is around 50%. We hence attribute the self-limiting Ni content in our PtNi product to the phase stability at this composition.

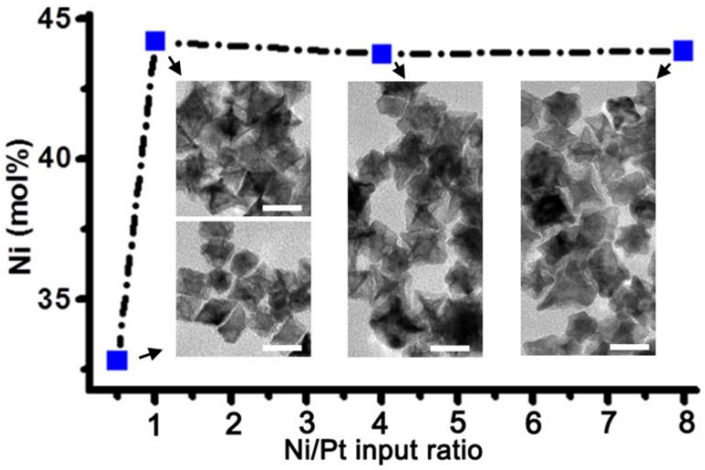

Figure 2.16 The compositions and TEM images of concave octahedron with different Ni/Pt input ratio. The dosages of $Pt(acac)_2$ are fixed at 2.5 mg. Scale bars = 20 nm.

It has been demonstrated that the catalytic activities of noble metal nanocrystals are highly dependent on their surface structure and composition. These single-crystalline PtNi nanocrystals with concave feature can be highly desirable for improving the ORR catalytic activities due to its high surface-volume ratio, optimized composition and the reduced Pt content.[19] To investigate the ORR activities of these highly concave octahedron, we well dispersed (Figure 2.17) the nanocrystals on Vulcan XC72R carbon and compared the ORR performance among the commercial Pt/C, the concave octahedron/C (denoted as c-Oct/C, 46.27% Ni by ICP-OES), and non-concave octahedron (denoted as Oct/C, 49.33% Ni by ICP-OES). The cyclic voltammetries and polarization curves are shown in Figure 2.18a-b. As indicated in Figure 2.18c, at 0.9 V the activity of c-Oct/C (specific activity 6.41 mA/cm^2, mass activity 2.22 mA/μg) and Oct/C (specific activity 2.94 mA/cm^2, mass activity 0.37 mA/μg) is superior to commercial Pt/C (specific activity 0.22 mA/cm^2, mass activity

0.17 mA/μg). The improvement of ORR activity with respect to pure Pt such as Pt/C is expected due to the adjustment of the d-band center through alloying with transition metals, which leads to a higher activity.[19] Importantly we observed that the specific activity of the PtNi Oct/C is also superior to most of Pt_3Ni octahedron reported. (Table 1) This can be attributed to the close to one Pt/Ni ratio in these PtNi octahdron, which has been suggested to be optimal for ORR activity.[26, 40-42] The concave PtNi octahedron show even higher specific ORR activity than the non-concave ones with similar composition (Figure 2.18c and Table 1). An enhancement factor of two in specific activity and an enhancement factor of six in mass activity were recorded for PtNi c-Oct/C over PtNi Oct/C (Figure 2.18c). This enhancement may be attributed to the exposure of active high-index surfaces and the surface strain effect in the concave morphology,[50-57] as well as the higher atom efficiency in the concave octahedron.

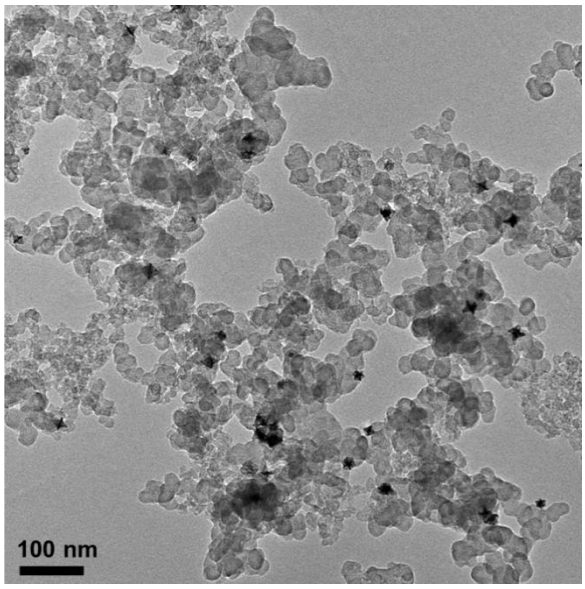

Figure 2.17 The TEM image of concave nanocrystal well dispersed on Vulcan XC72R carbon.

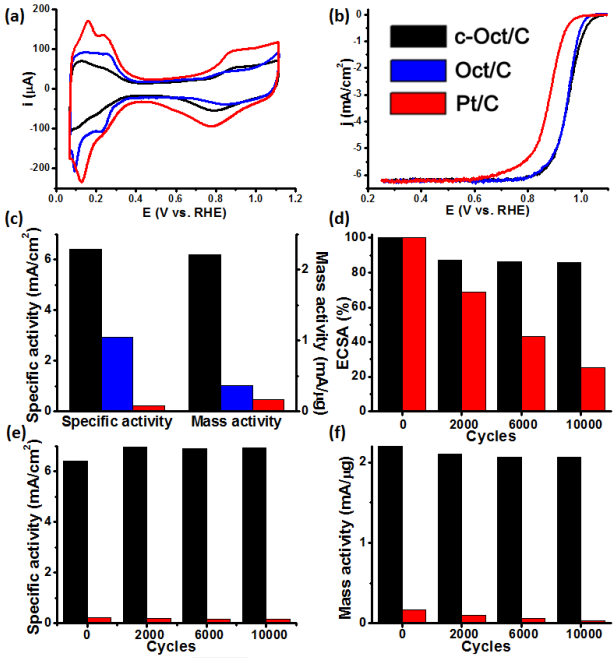

Figure 2.18 (a) The cyclic voltammogram and (b) the polarization curve of concave octahedron/C (c-Oct/C), non-concave octahedron/C (Oct/C), and commercial Pt/C (Pt/C). (c) The specific activities and the mass activities of c-Oct/C, Oct/C and Pt/C at 0.9 V (vs. RHE). (d) The electrochemical surface areas (ECSAs), (e) the specific activities and (f) the mass activities of c-Oct/C and Pt/C in different accelerating durability test (ADT) cycles at 0.9 V (vs. RHE).

Table 1 Comparison of compositions, sizes and ORR activities[a] for different Pt-Ni alloy catalysts

Reference	Catalyst	Ni %	Size (nm)[b]	Specific activity (mA/cm^2)	Mass activity (mA/μg)
This work	PtNi c-Oct/C	46.27	24±2	6.41	2.22
This work	PtNi Oct/C	49.33	23±3	2.94	0.37
[26]	PtNi/C[c]	~50	12±0.8	~3.78	~1.66
[41]	PtNi/C[d]	54	9.5±0.8	~3.14	~1.45
[22]	Pt_3Ni/C[e]	26	5.9±0.3	2.7	1.8
[33]	Pt_3Ni/C[e]	~25	~11	~0.74	~0.11
[39]	Pt_3Ni[f]	24	~5-7	0.85	0.53
This work	Pt/C	0	~2-5	0.22	0.17

a: ORR activities are measured at 0.9 V versus RHE in 0.1 M $HClO_4$, 1600 rpm
b: the size is defined as the distance between the two most remote vertices
c: PtNi octahedron on Vulcan XC-72 carbon
d: PtNi octahedron on Vulcan XC-72 carbon with surface composition of about 40 at. % Pt
e: Pt_3Ni octahedron on carbon black
f: Pt_3Ni truncated octahedron

We further evaluated the electrochemical durability of the PtNi c-Oct/C catalyst using the accelerated durability test between 0.6 and 1.1 V (versus RHE, 2000, 6000 and 10000 cycles) in O_2-saturated 0.1 M $HClO_4$ at a scan rate of 50 mV/s. After 10000 potential cycles, the c-Oct/C catalyst largely retained its electrochemical surface area (89%), specific activity (108%) and mass activity (93%) (Figure 2.18d-f, Figure 2.19). In addition, the highly concave structure was preserved after 10000 cycles (Figure 2.20), without degradation to octahedron or orthogonal skeleton structure as previous

reported.[26,32] STEM mapping confirms that the morphology of the concave octahedron was preserved and the distributions of Pt and Ni were still uniform over the nanocrystal after 10000 cycles of ADT (Figure 2.21). It was reported that the formation of terrace vacancies via dissolution of less noble component is rate-limiting in the dealloying of an alloy, and that the diffusion of the noble element to step edges may deter the dealloying process[58] Compared with the concave feature developed through fast electrochemical dissolution of Ni segregation[26], the PtNi concave feature reported here was developed gradually during the synthesis over 12 hrs. We suggest this prolonged process had allowed uniform Pt-Ni alloying, and allowed Pt to diffuse to and occupy less coordinated sites, rendering the system more stable during electrochemical reactions. In addition, the uniformly distributed Pt and Ni in the PtNi c-Oct/C may also shorten the time required for the diffusion of Pt to passivate vacancies formed via dissolution of Ni.[58] The above-mentioned characteristics in our PtNi c-Oct/C developed in situ during synthesis can hence lead to the excellent ORR durability.

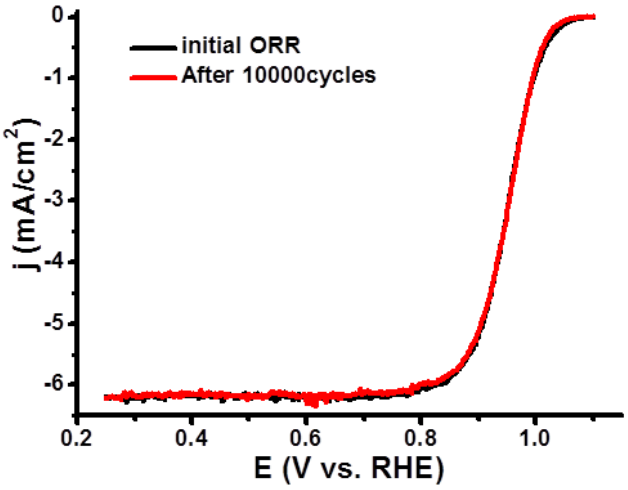

Figure 2.19 ORR polarization curves of concave octahedron/C (c-Oct/C) before and after 10000 potential cycles between 0.6 and 1.1 V.

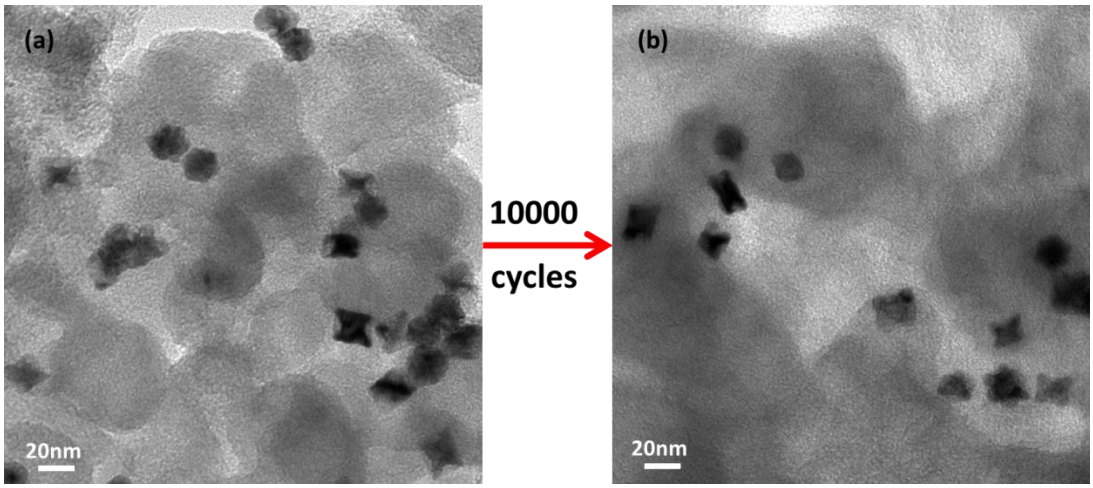

Figure 2.20 TEM images of concave octahedron/C (c-Oct/C) before and after 10000 potential cycles between 0.6 and 1.1 V.

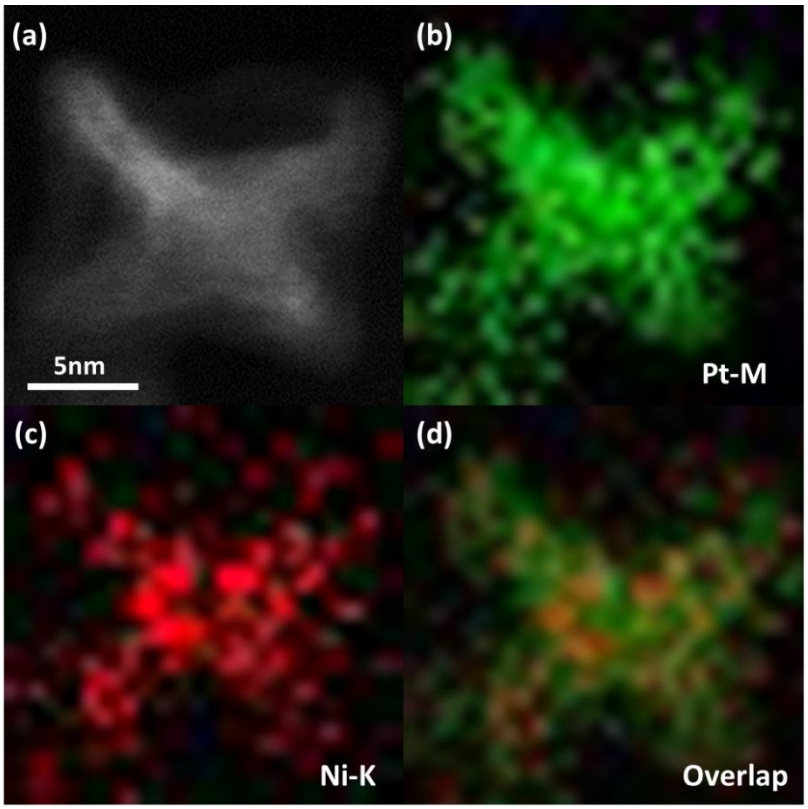

Figure 2.21 (a) The HAADF image of a concave nanocrystal after 10000 potential cycles between 0.6 and 1.1 V. (b) Element mappings of Pt and (c) element mappings of Ni of the nanocrystal shown in (a). (d) The overlapped element mapping of the nanocrystal shown in (a).

Summary

We have demonstrated a facile synthetic strategy to prepare single-crystalline PtNi octahedron nanocrystals with highly concave structure developed *in situ*. A plausible formation mechanism of the concave feature was also proposed (Figure 2.15). Under the reductive atmosphere provided by citric acid and DMF, Pt precursor was first reduced to form the seeds, during which stage NaBr together with oxygen etched out

the twinned seeds to produce octahedral single crystals. In the growth stage, the Ni^{2+} was massively reduced and incorporated into the PtNi alloy octahedral nanocrystals. Subsequent Ni segregation results in a Pt-rich skeleton along the edges of the octahedron and a Ni-rich surface in the center of each (111) facet of the octahedron. The Ni-rich surface was subject to oxidative etching by the oxygen in the solution, which leads to the *in situ* formation of the concave octahedron with self-limited Pt-Ni composition that is most resistant to phase-segregation and subsequent oxidative etching. The PtNi concave octahedron is rich in Ni (~44%), and exhibits outstanding activity and durability for the ORR. It may be attributed to the exposure of high-index surfaces and the passivation of the terrace vacancies by the uniformly alloyed structure developed during the synthesis. We expect this work will inspire rational design of PtNi catalysts for various chemical reactions with unique morphology, less Pt content and high performance.

Experimental Details

Synthesis of concave Pt-Ni nanocrystals: In a typical synthesis of concave Pt-Ni nanocrystals, 2.5 mg $Pt(acac)_2$, 1.6 mg $Ni(acac)_2$, 20 mg citric acid and 30 mg NaBr were mixed together with 10 mL DMF. The resulting homogeneous yellow-green solution was transferred to a 30-mL vial. The vial was then heated at 155 °C for 12 hours in an air atmosphere with no inert gas protection before it was cooled to room temperature. The black nanoparticles were precipitated, separated via centrifugation

and further purified by ethanol.

Synthesis of Pt-rich nanocrystal seeds: Small single-crystal seeds were prepared by adopting similar procedure as in the synthesis of concave Pt-Ni nanocrystals except the reaction time was changed to 4 hours. The seeds were precipitated, separated via centrifugation and thoroughly washed by water and ethanol.

Synthesis of non-concave Pt-Ni nanocrystals: 2 mg $Pt(acac)_2$, 1.6 mg $Ni(acac)_2$, 15 mg citric acid were mixed together with 10 mL DMF. The reaction was conducted for another 8 hour with the seeds introduced, during which the reaction was protected by nitrogen to eliminate air. The black nanoparticles produced were precipitated, separated via centrifugation and further purified by ethanol.

Synthesis of concave Pt-Ni nanocrystals with little NaBr: 2 mg $Pt(acac)_2$, 1.6 mg $Ni(acac)_2$, 15 mg citric acid were mixed together with 10 mL DMF. The reaction was conducted for another 8 hour with the seeds introduced, during which the reaction was in an air atmosphere with no inert gas protection before it was cooled to room temperature. The black nanoparticles produced were precipitated, separated via centrifugation and further purified by ethanol.

Disperse nanocrystals on carbon: Nanocrystals were dispersed on Vulcan XC72R carbon by mixing them together and sonicate overnight. The Pt loading was

controlled in the range of ~20 wt%.

Electrochemical measurements: Ethanol dispersion of purified nanoparticles was deposited on a glassy carbon electrode to obtain the working electrodes after the solvent is dried. The loading amount is 3 μg for c-Oct/C, 15 μg for Oct/C and 3.5μg for Pt/C. A silver chloride electrode (Ag/AgCl, 3 M NaCl) was used as the reference electrode and all the potentials measured were transformed to the value versus reversible hydrogen electrode (RHE). A platinum wire was used as the counter electrode. After bubbling nitrogen for 0.5 hour, the cyclic voltammgrams at a sweep rate of 50 mV/s were conducted in 0.1 M perchloric acid under the protection of nitrogen until the curves between 2 measurements are identical. The stable curve was then recorded. After bubbling oxygen for 0.5 h, the polarization curves was recorded at a sweep rate of 20 mV/s in an oxygen-saturated atmosphere with the working electrode rotating at 1600 rpm. The current is normalized with the geometric area of the electrode (0.196 cm^2) to get the current density. All electrode potentials were recorded with respect to the reversible hydrogen electrode (RHE) after IR correction[59]. The accelerated durability test (ADT) was conducted by cycling the potential between 0.6 and 1.1 V (vs. RHE) in oxygen saturated solutions.

Electrochemical surface area (ECSA) is estimated by measuring the charge associated with H_{upd} adsorption (Q_H) and assuming 210 μC/cm^2 for the adsorption of a monolayer of hydrogen on the surface. The H_{upd} adsorption charge (Q_H) can be

determined using $Q_H = 0.5 \times Q$, where Q is the charge in the H_{upd} adsorption/desorption area obtained after double-layer correction. Then, the specific ECSA was calculated based on the following relation:

$$\mathrm{ECSA} = \frac{\mathrm{Q_H}}{210\ \mu\mathrm{C/cm^2}}$$

For the ORR at a RDE, the Koutecky-Levich equation can be described as follows:

$$\frac{1}{i} = \frac{1}{i_k} + \frac{1}{i_d}$$

where i is the experimentally measured current, i_d is the diffusion-limiting current, and i_k is the kinetic current. Then, the kinetic current was calculated based on the following equation:

$$i_k = \frac{i \times i_d}{i_d - i}$$

And the specific activity at 0.9 V is the kinetic current at 0.9 V normalized to the ECSA.

References

1. Bing, Y., Liu, H., Zhang, L., Ghosh, D., & Zhang, J. (2010). Nanostructured Pt-alloy electrocatalysts for PEM fuel cell oxygen reduction reaction. *Chemical Society Reviews*, *39*(6), 2184-2202.
2. Su, D. S., & Sun, G. (2011). Nonprecious‐Metal Catalysts for Low‐Cost Fuel Cells. *Angewandte Chemie International Edition*, *50*(49), 11570-11572.
3. Chen, Z., Higgins, D., Yu, A., Zhang, L., & Zhang, J. (2011). A review on non-precious metal electrocatalysts for PEM fuel cells. *Energy & Environmental Science*, *4*(9), 3167-3192.
4. Chen, J., Lim, B., Lee, E. P., & Xia, Y. (2009). Shape-controlled synthesis of platinum nanocrystals for catalytic and electrocatalytic applications. *Nano Today*, *4*(1), 81-95.
5. Wu, J., & Yang, H. (2013). Platinum-based oxygen reduction electrocatalysts. *Accounts of chemical research*, *46*(8), 1848-1857.
6. Porter, N. S., Wu, H., Quan, Z., & Fang, J. (2013). Shape-control and electrocatalytic activity-enhancement of Pt-based bimetallic nanocrystals. *Accounts of chemical research*, *46*(8), 1867-1877.
7. Morozan, A., Jousselme, B., & Palacin, S. (2011). Low-platinum and platinum-free catalysts for the oxygen reduction reaction at fuel cell cathodes. *Energy & Environmental Science*, *4*(4), 1238-1254.
8. Gasteiger, H. A., Kocha, S. S., Sompalli, B., & Wagner, F. T. (2005). Activity benchmarks and requirements for Pt, Pt-alloy, and non-Pt oxygen reduction

catalysts for PEMFCs. *Applied Catalysis B: Environmental*, *56*(1), 9-35.

9. De Bruijn, F. A., Dam, V. A. T., & Janssen, G. J. M. (2008). Durability and degradation issues of PEM fuel cell components. *Fuel cells*, *8*(1), 3-22.
10. Greeley, J., Stephens, I. E. L., Bondarenko, A. S., Johansson, T. P., Hansen, H. A., Jaramillo, T. F., ... & Nørskov, J. K. (2009). Alloys of platinum and early transition metals as oxygen reduction electrocatalysts. *Nature chemistry*, *1*(7), 552-556.
11. Gasteiger, H. A. & Markovic, N. M. (2009). Just a Dream-or Future Reality? *Science*, *324*(5923), 48-49.
12. Nørskov, J. K., Bligaard, T., Rossmeisl, J., & Christensen, C. H. (2009). Towards the computational design of solid catalysts. *Nature chemistry*, *1*(1), 37-46.
13. Lee, I., Zhang, Q., Ge, J., Yin, Y., & Zaera, F. (2011). Encapsulation of supported Pt nanoparticles with mesoporous silica for increased catalyst stability. *Nano Research*, *4*(1), 115-123.
14. Li, Y., Li, Y., Zhu, E., McLouth, T., Chiu, C. Y., Huang, X., & Huang, Y. (2012). Stabilization of high-performance oxygen reduction reaction Pt electrocatalyst supported on reduced graphene oxide/carbon black composite. *Journal of the American Chemical Society*, *134*(30), 12326-12329.
15. Stamenkovic, V. R., Mun, B. S., Arenz, M., Mayrhofer, K. J., Lucas, C. A., Wang, G., ... & Markovic, N. M. (2007). Trends in electrocatalysis on extended and nanoscale Pt-bimetallic alloy surfaces. *Nature materials*, *6*(3), 241.
16. Wu, J., Gross, A., & Yang, H. (2011). Shape and composition-controlled platinum

alloy nanocrystals using carbon monoxide as reducing agent. *Nano letters*, *11*(2), 798-802.

17. Zhang, J., & Fang, J. (2009). A general strategy for preparation of Pt 3d-transition metal (Co, Fe, Ni) nanocubes. *Journal of the American Chemical Society*, *131*(51), 18543-18547.
18. Chen, G., Zhao, Y., Fu, G., Duchesne, P. N., Gu, L., Zheng, Y., ... & Lee, J. F. (2014). Interfacial effects in iron-nickel hydroxide-platinum nanoparticles enhance catalytic oxidation. *Science*, *344*(6183), 495-499.
19. Stamenkovic, V. R., Fowler, B., Mun, B. S., Wang, G., Ross, P. N., Lucas, C. A., & Marković, N. M. (2007). Improved oxygen reduction activity on Pt_3Ni (111) via increased surface site availability. *science*, *315*(5811), 493-497.
20. Aricò, A. S., Bruce, P., Scrosati, B., Tarascon, J. M., & Van Schalkwijk, W. (2005). Nanostructured materials for advanced energy conversion and storage devices. *Nature materials*, *4*(5), 366-377.
21. Guo, S., Zhang, S., & Sun, S. (2013). Tuning nanoparticle catalysis for the oxygen reduction reaction. *Angewandte Chemie International Edition*, *52*(33), 8526-8544.
22. Huang, X., Zhao, Z., Cao, L., Chen, Y., Zhu, E., Lin, Z., ... & Duan, X. (2015). High-performance transition metal–doped Pt3Ni octahedra for oxygen reduction reaction. *Science*, *348*(6240), 1230-1234.
23. Choi, S. I., Xie, S., Shao, M., Odell, J. H., Lu, N., Peng, H. C., ... & Wang, J. (2013). Synthesis and characterization of 9 nm Pt–Ni octahedra with a record high activity of 3.3 A/mgPt for the oxygen reduction reaction. *Nano letters*, *13*(7),

3420-3425.

24. Zhang, J., Yang, H., Fang, J., & Zou, S. (2010). Synthesis and oxygen reduction activity of shape-controlled Pt3Ni nanopolyhedra. *Nano Lett*, *10*(2), 638-644.
25. Huang, X., Zhu, E., Chen, Y., Li, Y., Chiu, C. Y., Xu, Y., ... & Huang, Y. (2013). A facile strategy to Pt3Ni nanocrystals with highly porous features as an enhanced oxygen reduction reaction catalyst. *Advanced materials*, *25*(21), 2974-2979.
26. Cui, C., Gan, L., Heggen, M., Rudi, S., & Strasser, P. (2013). Compositional segregation in shaped Pt alloy nanoparticles and their structural behaviour during electrocatalysis. *Nature materials*, *12*(8), 765.
27. Carpenter, M. K., Moylan, T. E., Kukreja, R. S., Atwan, M. H., & Tessema, M. M. (2012). Solvothermal synthesis of platinum alloy nanoparticles for oxygen reduction electrocatalysis. *Journal of the American Chemical Society*, *134*(20), 8535-8542.
28. Wang, X., Choi, S. I., Roling, L. T., Luo, M., Ma, C., Zhang, L., ... & Mavrikakis, M. (2015). Palladium-platinum core-shell icosahedra with substantially enhanced activity and durability towards oxygen reduction. *Nature communications*, *6*.
29. Zhang, L., Roling, L. T., Wang, X., Vara, M., Chi, M., Liu, J., ... & Mavrikakis, M. (2015). Platinum-based nanocages with subnanometer-thick walls and well-defined, controllable facets. *Science*, *349*(6246), 412-416.
30. Li, Y., Quan, F., Zhu, E., Chen, L., Huang, Y., & Chen, C. (2015). PtxCuy nanocrystals with hexa-pod morphology and their electrocatalytic performances towards oxygen reduction reaction. *Nano Research*, *8*(10), 3342-3352.

31. Liu, X., Wang, W., Li, H., Li, L., Zhou, G., Yu, R., ... & Li, Y. (2013). One-pot protocol for bimetallic Pt/Cu hexapod concave nanocrystals with enhanced electrocatalytic activity. *Scientific reports*, *3*.

32. Chen, C., Kang, Y., Huo, Z., Zhu, Z., Huang, W., Xin, H. L., ... & Chi, M. (2014). Highly crystalline multimetallic nanoframes with three-dimensional electrocatalytic surfaces. *Science*, *343*(6177), 1339-1343.

33. Li, Y.; Quan, F.; Chen, L.; Zhang, W.; Yu, H.; and Chen C. Synthesis of Fe-doped Octahedral Pt3Ni Nanocrystals with High Electrocatalytic Activity and Stability Towards Oxygen Reduction Reaction. RSC Adv. 2014, 4, 1895-1899.

34. Colón-Mercado, H. R., & Popov, B. N. (2006). Stability of platinum based alloy cathode catalysts in PEM fuel cells. *Journal of Power Sources*, *155*(2), 253-263.

35. Kang, Y., & Murray, C. B. (2010). Synthesis and electrocatalytic properties of cubic Mn-Pt nanocrystals (nanocubes). *Journal of the American Chemical Society*, *132*(22), 7568-7569.

36. Wu, Y., Cai, S., Wang, D., He, W., & Li, Y. (2012). Syntheses of water-soluble octahedral, truncated octahedral, and cubic Pt–Ni nanocrystals and their structure–activity study in model hydrogenation reactions. *Journal of the American Chemical Society*, *134*(21), 8975-8981.

37. Wang, D., Xin, H. L., Hovden, R., Wang, H., Yu, Y., Muller, D. A., ... & Abruña, H. D. (2013). Structurally ordered intermetallic platinum-cobalt core-shell nanoparticles with enhanced activity and stability as oxygen reduction electrocatalysts. *Nature materials*, *12*(1), 81.

38. Wu, J., Zhang, J., Peng, Z., Yang, S., Wagner, F. T., & Yang, H. (2010). Truncated octahedral Pt3Ni oxygen reduction reaction electrocatalysts. *Journal of the American Chemical Society*, *132*(14), 4984-4985.

39. Wu, Y., Wang, D., Niu, Z., Chen, P., Zhou, G., & Li, Y. (2012). A strategy for designing a concave Pt–Ni alloy through controllable chemical etching. *Angewandte Chemie International Edition*, *51*(50), 12524-12528.

40. Cui, C., Gan, L., Li, H. H., Yu, S. H., Heggen, M., & Strasser, P. (2012). Octahedral PtNi nanoparticle catalysts: exceptional oxygen reduction activity by tuning the alloy particle surface composition. *Nano letters*, *12*(11), 5885-5889.

41. Yang, H., Vogel, W., Lamy, C., & Alonso-Vante, N. (2004). Structure and electrocatalytic activity of carbon-supported Pt− Ni alloy nanoparticles toward the oxygen reduction reaction. *The Journal of Physical Chemistry B*, *108*(30), 11024-11034.

42. Fortunelli, A., Goddard III, W. A., Sementa, L., Barcaro, G., Negreiros, F. R., & Jaramillo-Botero, A. (2015). The atomistic origin of the extraordinary oxygen reduction activity of Pt 3 Ni 7 fuel cell catalysts. *Chemical Science*, *6*(7), 3915-3925.

43. Vitos, L., Ruban, A. V., Skriver, H. L., & Kollar, J. (1998). The surface energy of metals. *Surface Science*, *411*(1), 186-202.

44. Gan, L., Cui, C., Heggen, M., Dionigi, F., Rudi, S., & Strasser, P. (2014). Element-specific anisotropic growth of shaped platinum alloy nanocrystals. *Science*, *346*(6216), 1502-1506.

45. Speight, J. G. (2005). *Lange's handbook of chemistry* (Vol. 1). New York: McGraw-Hill.

46. Walker, R. A., & Darby, J. B. (1970). Thermodynamic properties of solid nickel-platinum alloys. *Acta Metallurgica*, *18*(12), 1261-1266.

47. Wiley, B., Sun, Y., & Xia, Y. (2007). Synthesis of silver nanostructures with controlled shapes and properties. *Accounts of Chemical Research*, *40*(10), 1067-1076.

48. Lu, Z. W., Wei, S. H., & Zunger, A. (1991). Long-range order in binary late-transition-metal alloys. *Physical review letters*, *66*(13), 1753.

49. Shang, S. L., Wang, Y., Kim, D. E., Zacherl, C. L., Du, Y., & Liu, Z. K. (2011). Structural, vibrational, and thermodynamic properties of ordered and disordered $Ni_{1-x}Pt_x$ alloys from first-principles calculations. *Physical Review B*, *83*(14), 144204.

50. Tian, N., Zhou, Z. Y., Sun, S. G., Ding, Y., & Wang, Z. L. (2007). Synthesis of tetrahexahedral platinum nanocrystals with high-index facets and high electro-oxidation activity. *science*, *316*(5825), 732-735.

51. Jin, M., Zhang, H., Xie, Z., & Xia, Y. (2011). Palladium Concave Nanocubes with High-Index Facets and Their Enhanced Catalytic Properties. *Angewandte Chemie International Edition*, *50*(34), 7850-7854.

52. Zhang, L., Zhang, J., Kuang, Q., Xie, S., Jiang, Z., Xie, Z., & Zheng, L. (2011). Cu^{2+}-assisted synthesis of hexoctahedral Au–Pd alloy nanocrystals with high-index facets. *Journal of the American Chemical Society*, *133*(43),

17114-17117.

53. Zhang, H., Jin, M., & Xia, Y. (2012). Noble-Metal Nanocrystals with Concave Surfaces: Synthesis and Applications. *Angewandte Chemie International Edition*, *51*(31), 7656-7673.

54. Zhang, J., Langille, M. R., Personick, M. L., Zhang, K., Li, S., & Mirkin, C. A. (2010). Concave cubic gold nanocrystals with high-index facets. *Journal of the American Chemical Society*, *132*(40), 14012-14014.

55. Huang, X., Zhao, Z., Fan, J., Tan, Y., & Zheng, N. (2011). Amine-assisted synthesis of concave polyhedral platinum nanocrystals having {411} high-index facets. *Journal of the American chemical Society*, *133*(13), 4718-4721.

56. Yu, T., Kim, D. Y., Zhang, H., & Xia, Y. (2011). Platinum concave nanocubes with high‐index facets and their enhanced activity for oxygen reduction reaction. *Angewandte Chemie*, *123*(12), 2825-2829.

57. Xu, X., Zhang, X., Sun, H., Yang, Y., Dai, X., Gao, J., ... & Sun, S. G. (2014). Synthesis of Pt–Ni Alloy Nanocrystals with High‐Index Facets and Enhanced Electrocatalytic Properties. *Angewandte Chemie*, *126*(46), 12730-12735.

58. Snyder, J., & Erlebacher, J. (2010). Kinetics of crystal etching limited by terrace dissolution. *Journal of The Electrochemical Society*, *157*(3), C125-C130.

59. van der Vliet, D., Strmcnik, D. S., Wang, C., Stamenkovic, V. R., Markovic, N. M., & Koper, M. T. (2010). On the importance of correcting for the uncompensated Ohmic resistance in model experiments of the Oxygen Reduction Reaction. *Journal of Electroanalytical Chemistry*, *647*(1), 29-34.

Chapter 3 Biomimetic synthesis of an ultrathin platinum nanowire network with a high twin density for enhanced electrocatalytic activity and durability

Introduction

As discussed in Chapter 2, fuel cells have attracted much research interest as they are promising candidates for providing clean energy. And one of the most critical challenges for fuel-cell applications is the sluggish reduction kinetics of the oxygen reduction reaction (ORR) at the cathode.[1] So far, platinum and Pt-based nanomaterials are recognized as the most effective electrocatalysts for the ORR.[1,2] Current state-of-the-art electrocatalysts rely almost exclusively on Pt black or Pt nanoparticles (2-5 nm) dispersed onto a carbon black support (Pt/C).[1,2] However, the practical large-scale commercialization of fuel cells is still a great challenge because of the loss of electrochemical surface area (ECSA) and the decrease of catalytic activity over time.[3,4] Another important issue of fuel-cell applications is the anodic reaction, that is, the oxidation of hydrogen or alcohols (for example, methanol or ethanol).[1] The direct methanol fuel cell is particularly attractive due to its high volumetric energy density and its ease of storage and transport compared to the hydrogen fuel cell.[5] Similar to the cathode, Pt-based nanomaterials are currently used as the most efficient electrocatalysts for the methanol oxidation reaction (MOR), which unfortunately suffers from the same problems including poor reaction kinetics and poisoning.[5-7] Therefore, the development of electrocatalysts with improved catalytic activity and durability is highly desirable but remains a significant challenge. The control on

nanomaterial structures provides a sensitive knob to tune the properties and improve the functions.[8,9] Nanostructured Pt with various morphologies has been extensively exploited in the search to improve the electrocatalytic performance.[10-14] To this end, one-dimensional (1D) nanostructures, such as nanowires, represent an important research direction because 1D nanostructures possess unique advantages compared to their zero-dimensional (0D) counterparts. For example, the structural anisotropy can slow down the ripening process; and the display of long segments of low-index crystalline planes along the nanowire is particularly beneficial for the ORR.[5,15,16] As a result, various methods including both top-down and bottom-up have been developed to synthesize Pt 1D nanostructures.[17-25] Most prior studies reported the production of single-crystalline Pt nanowires.[18,21,23-25] Meanwhile, twinning of materials has been shown to greatly affect the physical and chemical material properties, including various surface adsorption, heterogeneous catalytic, and electrocatalytic processes.[26-29] While nanotwins have been widely employed to enhance mechanical properties, very limited effort has been devoted to engineering of twin defects in nanomaterials for improved catalysis and electrocatalysis.[30,31]

Results and Discussions

An ultrathin Pt multiple-twinned nanowire network (MTNN) was synthesized as an efficient electrocatalyst, which exhibits a higher ECSA and much improved activity toward both ORR and MOR when compared to current state-of-the-art commercial

Pt/C electrocatalysts. Furthermore, it shows significantly improved durability with much less decay of ECSA at prolonged reaction times. The unique feature of the nanowire in our studies is its high density of twin planes, which have been proposed to play a significant role in the promotion of the electrocatalytic performance.[28,29]

The Pt MTNN was synthesized by biomimetic synthesis using a specific Pt-binding peptide (amino acid sequence Ac-TLHVSSY-CONH2, named BP7A, identified through phage display).[32,33] Peptide-directed biomimetic syntheses have emerged as a new synthetic route and demonstrated the potential to maneuver nanomaterial structures and functions in a controllable manner under mild environmental-benign conditions.[34-38] Particularly, peptide BP7A has been demonstrated to lead to exclusive formation of twinned Pt nanoparticles, which is uncommon in conventional syntheses.[38] Here, we further exploit its potential for the synthesis of 1D Pt nanowire with dense twin defects. Although nanowires with twin defects have been observed before, the occurrence of twinning appeared relatively random and rare.[18-25] This is the first report on synthesis of Pt nanowires that are ultrathin yet show a high twin population.

The synthesis was carried out at room temperature in aqueous solution using the peptide BP7A as the surfactant molecule. The Pt precursor H_2PtCl_6 (1 mM) was first mixed with the peptide in solution (100 μgmL^{-1}), followed by introduction of reducing agents ascorbic acid (5 mM) and sodium borohydride (0.8 mM). Then, more

Pt precursor K_2PtCl_4 (0.5 mM) was added after sodium borohydride to sustain complete growth of the nanowire. The as-synthesized Pt MTNN is shown in Figure 3.1a and b. The low-magnification TEM image (Figure 3.1a) shows the abundant wavy Pt nanowires interconnected with each other forming nanowire networks. The higher-magnification TEM image (Figure 3.1b) shows an individual nanowire with a thin diameter of about 2 nm. The structure of Pt MTNN was further characterized with high-resolution TEM (HRTEM, Figure 3.1c-g). The measured lattice spacing of 0.23 nm is consistent with the {111} lattice plane of Pt. The nanowire shows relative long segments of crystal planes as compared to those ultrasmall Pt nanoparticles, and the majority of the displayed facets are low-index {111} planes (Figure 3.1c), which have been shown to be more active towards the ORR than the {100} planes in acidic media.[39,40] The typical growth direction of the nanowire is along <111>, but it may change from one particular <111> direction to another <111> direction, as indicated by the white arrows in Figure 3.1d,e,g. This change in growth direction contributes to the zigzag wavy morphology of the nanowire (Figure 3.1d,e), and also to the branching of the nanowire (Figure 3.1g). Twin defects were frequently observed cross-sectioning the nanowire, as indicated by the blue arrows (Figure 3.1c,f), and also at joints where the nanowire changes growth direction (Figure 3.1d). Along with twin defects, surface defects such as corner and edge atoms as well as high-index facets are observed along the nanowire, which would potentially contribute to the ORR activity.[39,40] The occurrence of abundant twinning may be the result of the attachment growth mode of the nanowire mediated by the peptide, which will be

discussed in the following; and also comes from the specific stabilization of the peptide to twinning defects as previously reported.[38] More mechanistic studies regarding the stabilization of the peptide to twinning defects are under way. Despite its ultrathin and twin-rich nature, the crystallinity of Pt MTNN was confirmed by powder X-ray diffraction (Figure 3.1h). Diffraction peaks were indexed to (111), (200), (220), and (311) reflections of face-centered cubic (fcc) Pt (JCPDS no. 87-0647). All diffraction peaks are broadened, indicating nanoscale structural features. In addition, energy-dispersive X-ray spectroscopy (EDS) was performed on a random selection of the sample, showing these Pt MTNNs are composed only of platinum (Figure 3.1i). The Cu signals arise from the TEM grid.

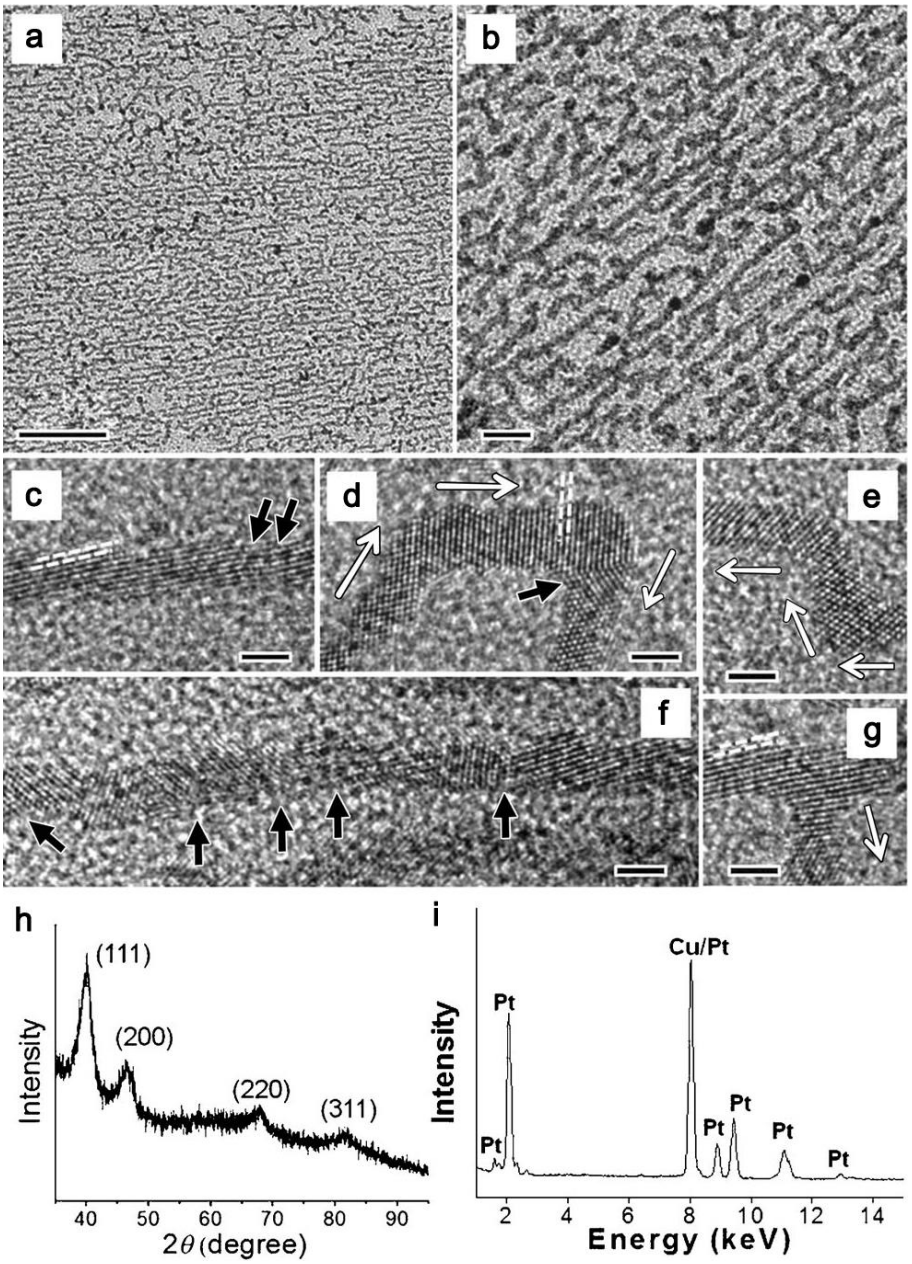

Figure 3.1 (a and b) Low- and high-magnification TEM images of Pt MTNN. (c-g) High-resolution TEM images of Pt MTNN. Black arrows indicate the presence of twin defects; whereas white arrows indicate the growth directions. (h) X-ray diffractogram of Pt MTNN. (i) EDX of Pt MTNN. The sale bares are 50 (a), 10 (b), and 2 nm (c-g). The interlayer distance given by dashed lines in (c, d, and g) is 0.23 nm.

The dynamics of the Pt MTNN formation process was studied by TEM and HRTEM (Figure 3.2). Both small primary particles and short wires formed at the initial stage of the reaction (Figure 3.2a). With increasing reaction time, network morphology started to appear (Figure 3.2b). The width of nanowires changed very little throughout the growth process, suggesting that nanowires grow from primary nanoparticles through oriented attachment.[41] Nanowires formed at the initial stage were closely examined under HRTEM (Figure 3.2c-f and Figure 3.3). Figure 3.2c-f show various number (2-4) of primary nanoparticles attached together leading to lengthening of the nanowires. As indicated by the black arrows, twinning was already frequently observed in these initially formed short wires. Figure 3.3 shows in more detail the appearance of joint area between two primary particles, and a twin plane formed between two primary particles. Previous studies have suggested both lattice-matched and lattice-mismatched attachment modes in nanowire growth, with the lattice-matched attachment leading to a single-crystal structure and the lattice-mismatched attachment leading to twin planes in the wire.[42] Also, reconstruction and rearrangement during the growth process would results in the disappearance of twin defects.[42] The abundance of twin defects observed in the final product suggests lattice-mismatched attachment is enhanced and preserved with the existence of peptide molecule, possibly due to the specific stabilization of twin sites by the BP7A peptides.[38] The peptide concentration was also found to be a critical parameter in the formation of nanowires. Nanowires form at sufficient peptide concentration, while only nanoparticles form at lower peptide concentration (Figure

3.4). This may be attributed to stronger confinement on primary particles at higher peptide concentration, and stronger intermolecular interactions between peptides which drives the assembly process.[43]

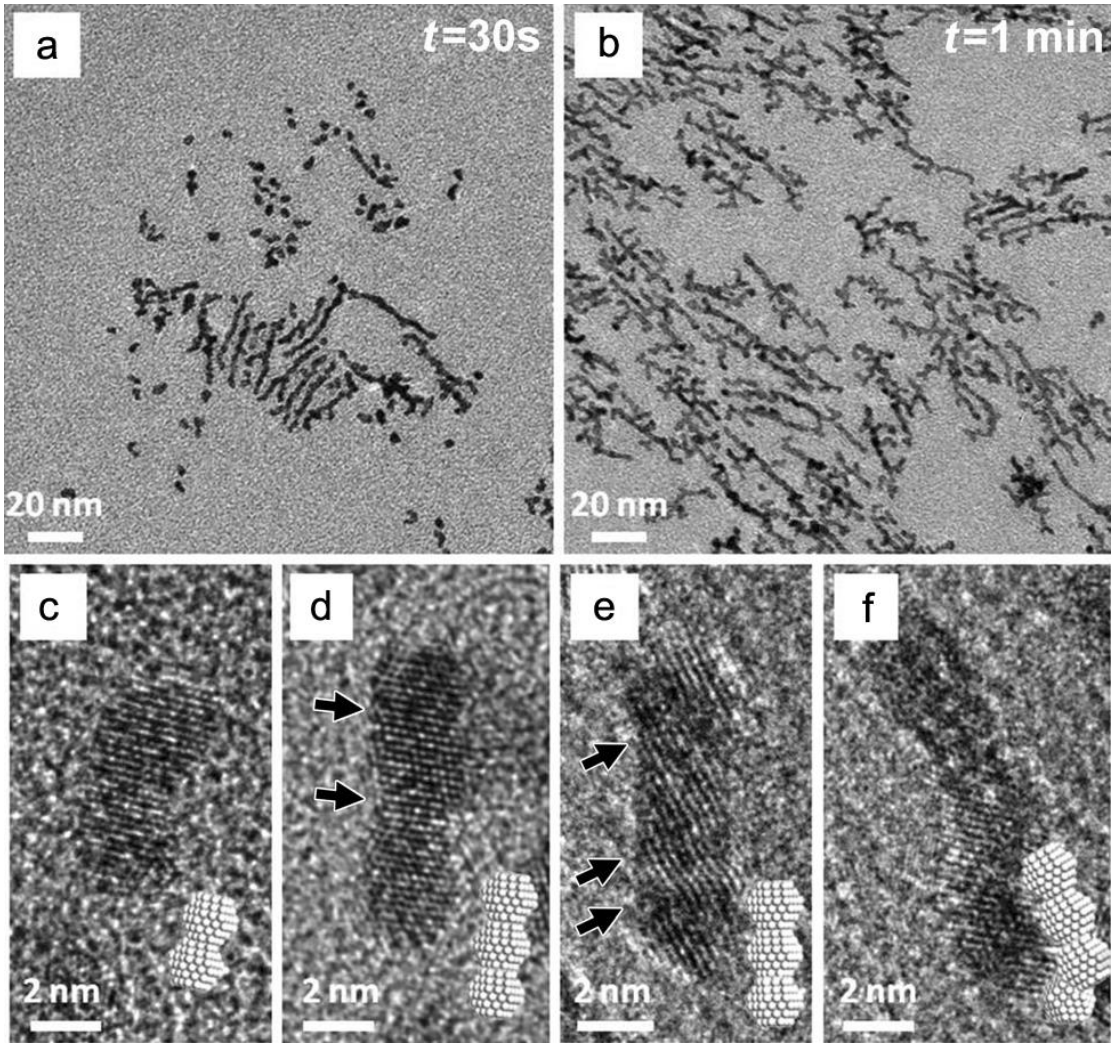

Figure 3.2 (a and b) TEM images of Pt MTNN formed after 30 s and 1 minute, respectively. (c-f) High-resolution TEM images of Pt MTNN formed after 30 s. Black arrows indicate presence of twin defects.

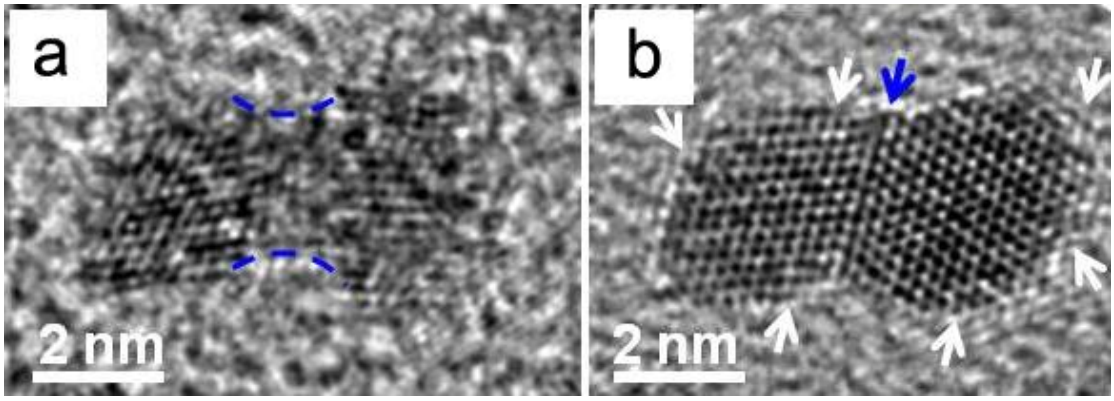

Figure 3.3 High resolution TEM images of (a) Two Pt nanoparticles attached together forming a joint area indicated by blue dashed curves. (b) Two Pt nanoparticles attached together forming a twin plane indicated by the blue arrow. White arrows indicate surface step and edge atoms.

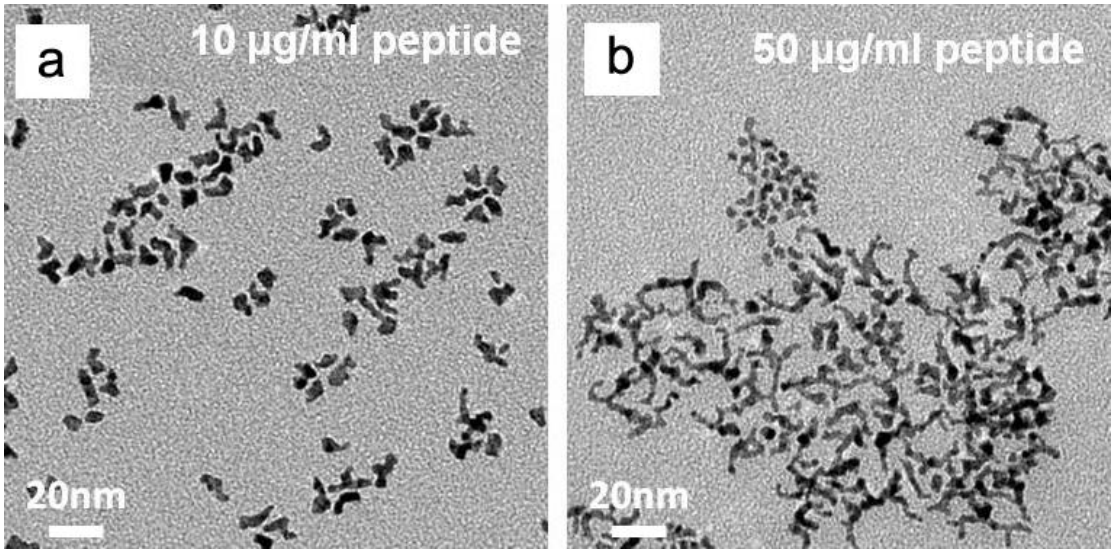

Figure 3.4 Pt nanoparticles synthesized at various BP7A peptide concentrations: (a) 10 µg/mL. (b) 50 µg/mL.

With the unique structural features, Pt MTNN was evaluated as an electrocatalyst, and benchmarked against current state-of-the-art commercial Johnson Matthey (JM) Pt/C catalyst. Pt MTNN was loaded onto carbon black nanoparticles through a previously

established process (Figure 3.5) and washed repeatedly before the measurement (see the Supporting Information for experimental details).[44] The electrocatalytic activity was first probed using cyclic voltammetry (CV) recorded at room temperature in a nitrogen-purged 0.1 M $HClO_4$ solution at a sweep rate of 50 mVs^{-1} (Figure 3.6a). CV curves show typical peaks associated with hydrogen adsorption/desorption (Figure 3.6a).[11] The ECSA was calculated by measuring the charge associated with hydrogen adsorption/desorption between 0 and 0.4 V and assuming Q_{ref} = 0.21 $mCcm^{-2}$ for the adsorption of a hydrogen monolayer. Notably, Pt MTNN showed an even higher specific ECSA (80.36 m^2g^{-1}) than the JM Pt/C catalyst (77.77 m^2g^{-1}). This may result from the ultrathin nature of the nanowires.

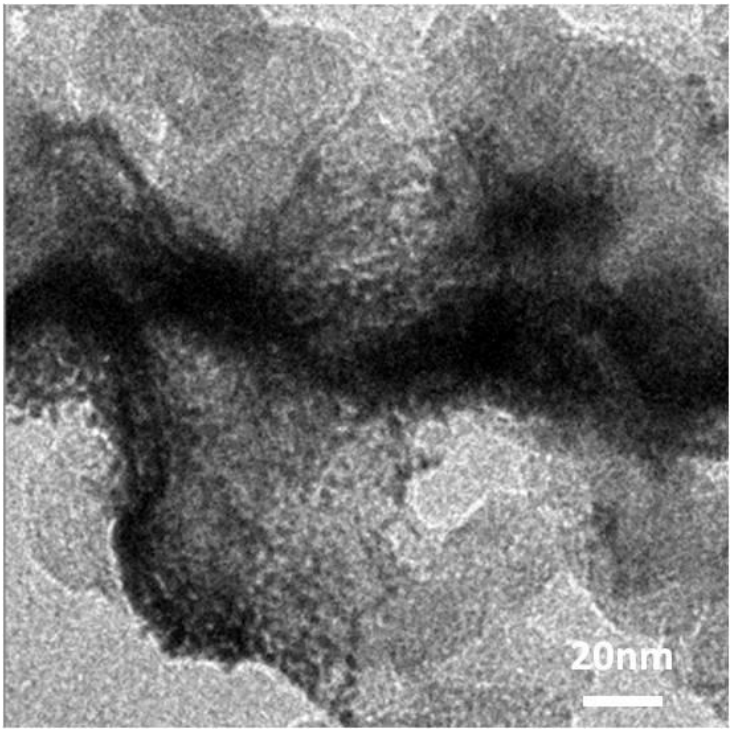

Figure 3.5 TEM image of Pt MTNN loading onto carbon black.

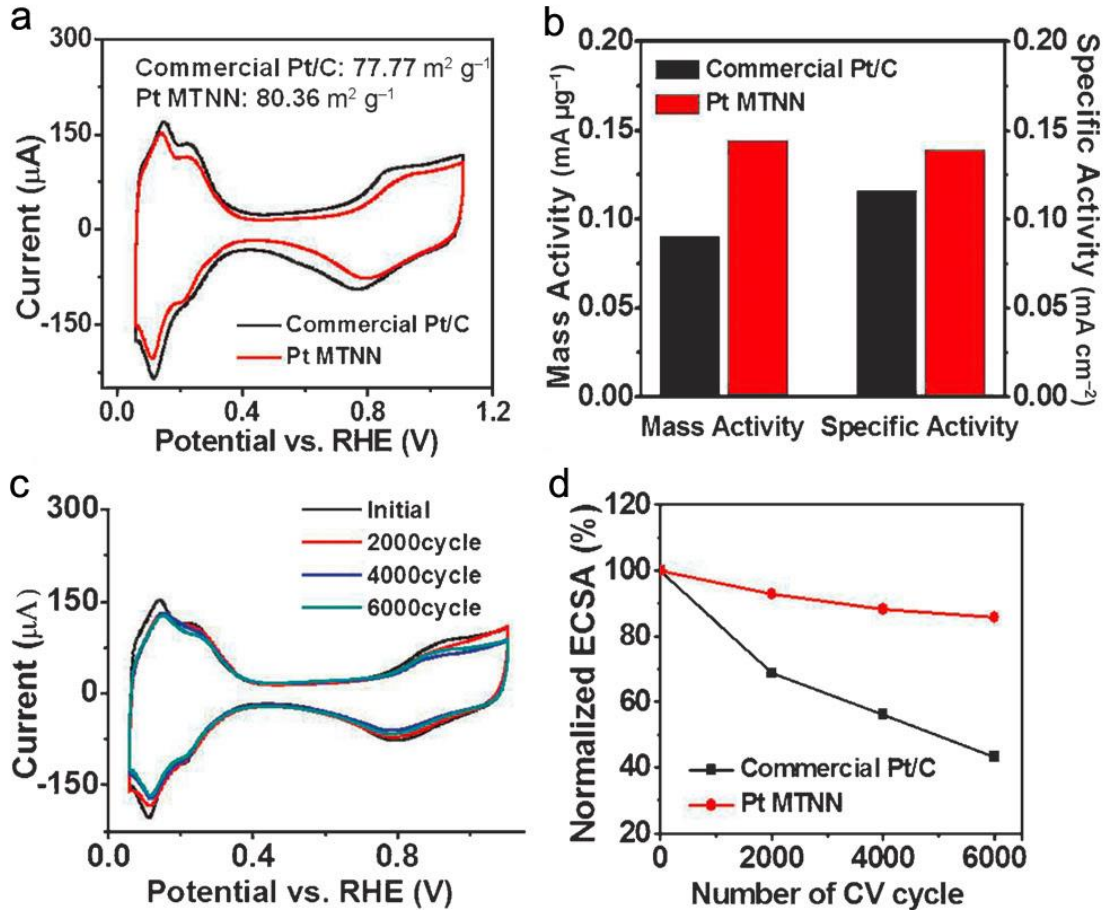

Figure 3.6 (a) CV curves of the JM Pt/C and Pt MTNN catalysts in a deoxygenated 0.1m $HClO_4$ solution at a scan rate of 50 mVs^{-1}. (b) Corresponding mass activities and specific activities at 0.9 V of JM Pt/C and Pt MTNN, respectively. (c) CV curves of Pt MTNN before and after an accelerated durability test. The test was carried out at room temperature in an O_2-saturated 0.1m $HClO_4$ solution with cyclic potentials sweeping between 0.6 and 1.1 V at a sweep rate of 50 mVs^{-1}. (d) Loss of ECSA of JM Pt/C and Pt MTNN as a function of the cycling number.

The ORR catalytic activity was tested using a rotating disk electrode (RDE) in an oxygen-saturated 0.1 M $HClO_4$ solution at a sweep rate of 10 mVs^{-1} and at a rotation

rate of 1600 rpm. The polarization curves show ORR onsets between 0.8 and 0.9 V (vs. the reversible hydrogen electrode, RHE) consistent with nanostructured platinum electrocatalysts (Figure 3.7).[11,15] Notably, Pt MTNN shows a slight shift toward higher potential compared with the JM Pt/C catalyst, suggesting a decrease in the ORR overpotential,[1] which can be attributed to the rich long segments of the {111} planes on the nanowire surface. The measured kinetic current density at 0.9 V was normalized over the Pt loading weight and ECSA to yield the mass activity and specific activity, respectively (Figure 3.6b). Pt MTNN showed a mass activity of 0.144 $mAmg^{-1}$, a 58.2% increase compared with the JM Pt/C catalyst (0.091 $mAmg^{-1}$). Although with a higher ECSA, Pt MTNN still shows a higher specific activity (0.139 $mAmg^{-1}$) compared with the JM Pt/C catalyst (0.116 $mAmg^{-1}$). To further explore the kinetics of the ORR, we carried out a Koutecky-Levich (K-L) plot at various potentials (Figure 3.8). The kinetic current density versus rotation speed plotted at varying potentials all show a linear relationship with a consistent slope, suggesting that the ORR catalyzed by Pt MTNN closely follows the highly desirable $4e^-$ process.[15]

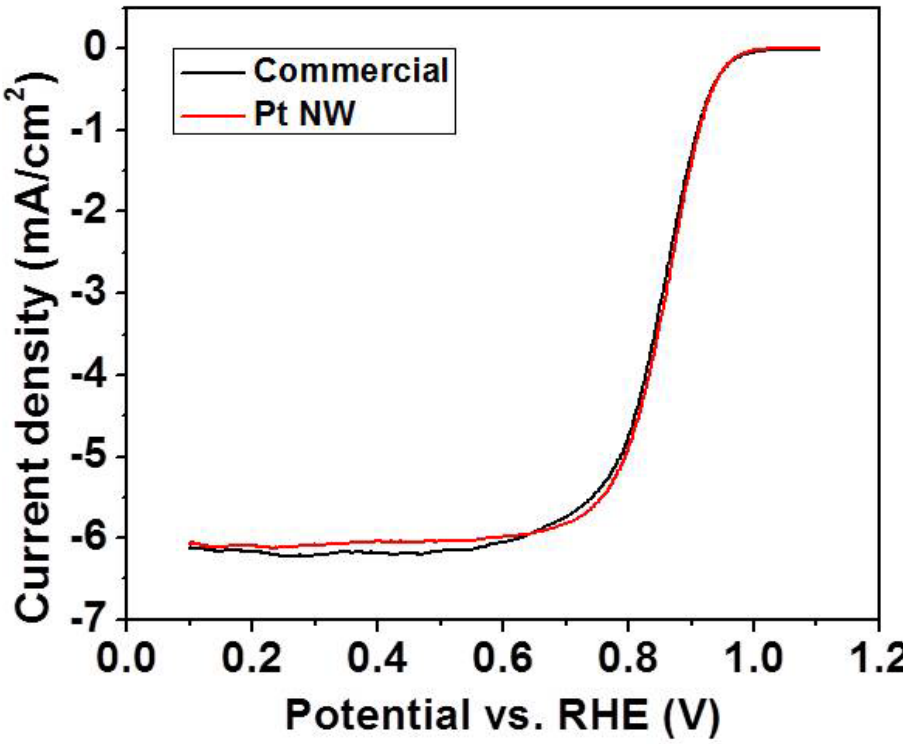

Figure 3.7 Polarization curves of JM Pt/C and Pt MTNN catalysts recorded at room temperature in an O_2-saturated 0.1 M $HClO_4$ solution with a sweep rate of 10 mV/s and a rotation rate of 1600 rpm.

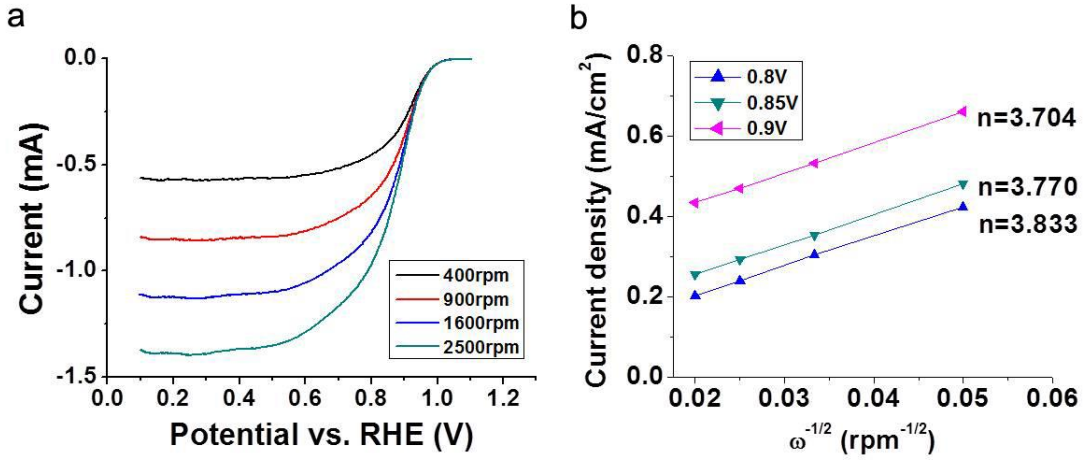

Figure 3.8 (a) Polarization curves of Pt MTNN recorded at room temperature in an O_2-saturated 0.1 M $HClO_4$ with a scan rate of 10 mV/s at different rotation rates. (b) Koutecky-Levich plots at different potentials derived from data in (a).

Since the decay of the electrocatalyst at the electrode remains an important issue for fuel-cell applications, we further examined the stability of Pt MTNN by an accelerated durability test (ADT). ADT was conducted at room temperature in O_2-saturated 0.1 M HClO4 solutions by applying cyclic potential sweeps between 0.6 and 1.1 V versus RHE at a sweep rate of 50 mVs^{-1} (Figure 3.6c,d). Pt MTNN showed excellent stability and a little drop of the ECSA during the test (Figure 3.6c), while JM Pt/C showed a much faster decrease of ESCA (Figure 3.9). The ECSA drops of Pt MTNN and JM Pt/C were normalized to their initial ECSA, respectively (Figure 3.6d). After 6000 cycles, Pt MTNN lost 14.2% of its initial ECSA, whereas the JM Pt/C catalyst suffered a severe degradation of 56.7% loss of its initial ECSA. We suggest the stability of the nanowires may come from its unique structure, that is, an ultrathin 1D structure which could slow down the ripening and dissolution process. Moreover, nanotwins have been observed to slow down the atomic transport process, which might also contribute to the overall stability of the nanowires.[31] The morphology changes of Pt MTNN and JM Pt/C before and after ADT were investigated by TEM (Figure 3.10). The Pt nanoparticle size of the JM Pt/C catalyst increased from 2-5 nm to 5-25 nm, suggesting considerable nanoparticle ripening and aggregation. Although having some increase in diameter and becoming shorter, Pt MTNN remained its 1D morphology, and the twin planes remain frequently observed (Figure 3.11).

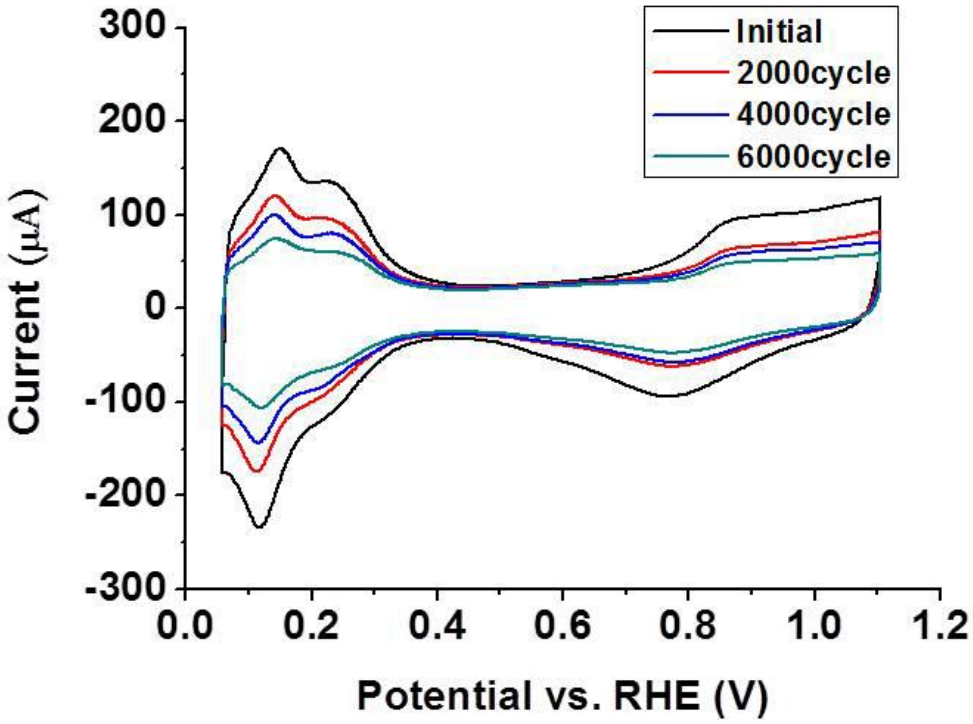

Figure 3.9 CV curves of JM Pt/C before and after accelerated durability test. The test was carried out at room temperature in an O_2-saturated 0.1 M $HClO_4$ solution with cyclic potentials sweeping between 0.6 and 1.1 V at a sweep rate of 50 mV/s.

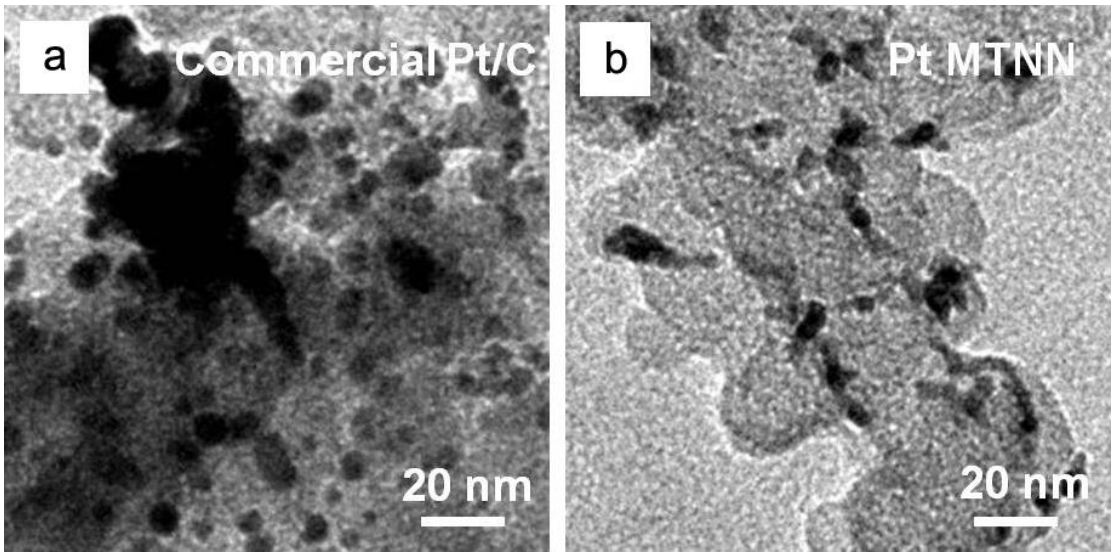

Figure 3.10 TEM images of (a) JM Pt/C and (b) Pt MTNN catalysts after accelerated durability test.

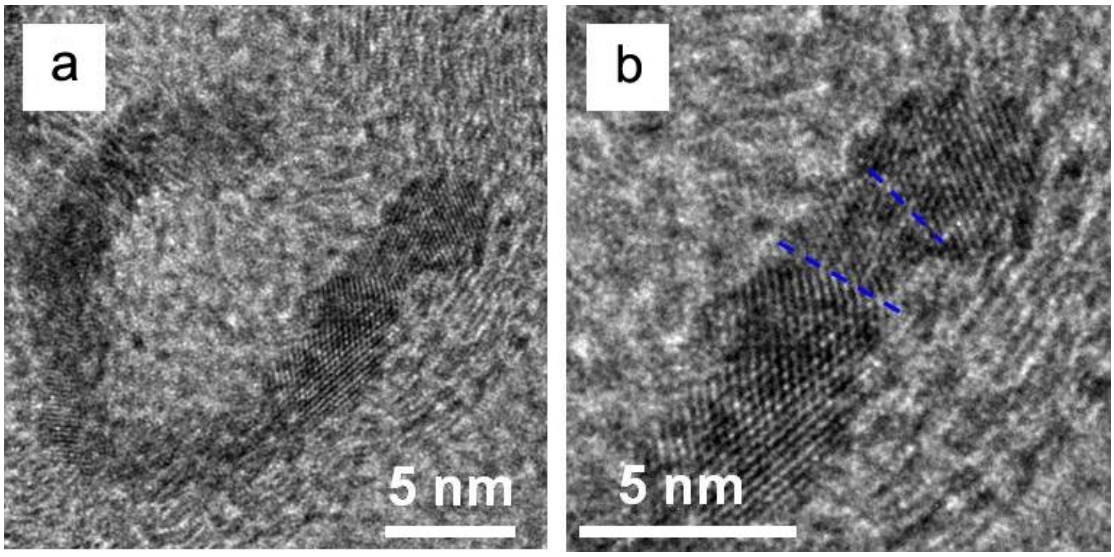

Figure 3.11 HRTEM images of Pt MTNN after accelerated durability test. Blue lines indicate twin planes.

We further evaluated the electrocatalytic performance of Pt MTNN in MOR, using CV measurement recorded in 0.1 M H_2SO_4 electrolyte with 0.5 M methanol at a sweep rate of 50 mVs^{-1} (Figure 3.12a). There are two oxidation peaks for methanol oxidation, that is, a 0.94 V peak (vs. RHE) in the anodic scan and a 0.7 V peak (vs. RHE) in the cathodic scan which is commonly assigned to the oxidation of partially oxidized species that adsorb onto the Pt surface after the anodic scan.[5] The current density can be directly related to the catalytic activity. As shown in Figure 3.12a, the catalytic activity of Pt MTNN exceeds that of the JM Pt/C catalyst in both forward and backward scan. The forward-current peak density of Pt MTNN is 580.97 $mAmg^{-1}$, which is 148.5% higher than that of the JM Pt/C catalyst (237.77 $mAmg^{-1}$). The backward peak current density is 764.04 $mAmg^{-1}$, which is 182.8% higher than that of the JM Pt/C catalyst (270.19 $mAmg^{-1}$). Emergence of grain boundaries at the surface

has been proposed to serve as active sites with greatly improved MOR activity.[28,29] The presence of high-density twin defects cross-sectioning the nanowire may create more surface-active sites and therefore facilitate the oxidation process.

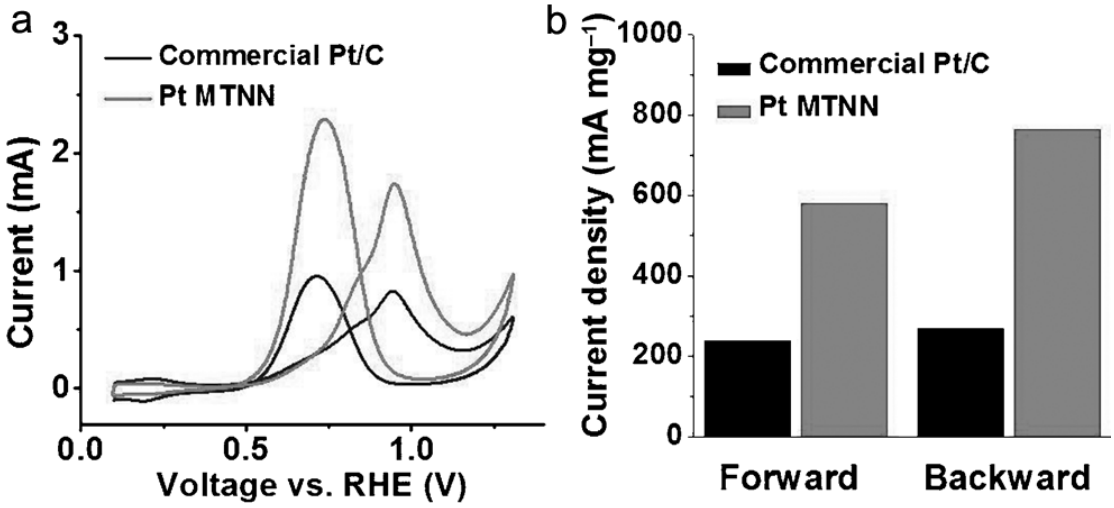

Figure 3.12 (a) CV curves of JM Pt/C and Pt MTNN catalysts in a deoxygenated 0.5 M H_2SO_4 solution containing 1 M methanol at a scan rate of 50 mVs^{-1}. (b) Corresponding mass activities of JM Pt/C and Pt MTNN.

Summary

A 1D Pt nanowire network structure with a high density of twin planes was developed as an efficient electrocatalyst for fuel-cell applications. Our studies demonstrate that the nanostructure shows much enhanced activity in both ORR and MOR. Moreover, they show a greatly improved durability in the ORR at prolonged reaction times. The electrocatalytic performance improvement is attributed to the unique structure of the nanowire, that is, an ultrathin 1D morphology with a large population of twin planes. This unique structure demonstrates that engineering of structural defects can be used

to design next-generation electrocatalysts. Moreover, defects have also been shown to have significant influence on many surface-sensitive catalysis processes, for example, defect sites have been found to greatly increase the catalytic activity in the reduction of nitrophenol or potassium ferricyanide.[45] More research effort could be devoted to defect engineering in the design of novel catalysts.[46] Taken together, our studies demonstrate control on the production of unique nanostructures and structure-enhanced properties, which is the focal point of designing nanomaterials for various applications.

Experimental Details

Nanowire synthesis: Pt MTNN was synthesized under aqueous condition using the strong reducing agent $NaBH_4$ to induce nucleation and the weak reducing agent ascorbic acid to sustain growth in the presence of BP7A peptide. In a typical synthesis, 0.5 mL H_2PtCl_6 stock solution (10 mM), 0.5 mL peptide stock solution (1 mg/mL), and 3.5 mL H_2O were premixed in a glass vial. The $NaBH_4$ solution (50 mM) and ascorbic acid solution (50 mM) were freshly prepared each time before use. 0.5 mL ascorbic acid solution was first introduced into the reaction vial, followed by the injection of 0.08 mL $NaBH_4$ solution. 1 minute after the injection of $NaBH_4$, another 0.5 mL of K_2PtCl_4 stock solution (10 mM) was added. The final product was obtained at 1 hour. For reactions with varying peptide concentrations, different amounts of peptide stock solutions were introduced to meet the desired peptide concentrations,

and the water amount was adjusted correspondingly to maintain final solution volume at 5 mL.

Loading Pt MTNN onto carbon black: Pt MTNN was loaded onto carbon black nanoparticles through a previously established process.[44] First, 5 mL of the pristine Pt MTNN solution was mixed with 7.5 mL IPA solvent and sonicated for 5 minutes. Then, carbon black (Vulcan XC72R carbon) was dissolved in IPA in 2 mg/mL concentration and sonicated until well dispersed. To load Pt MTNN onto carbon black, the Pt MTNN solution and certain amount of carbon black solution were mixed in 1:4 weight ratios (Pt weight quantified through ICP) and sonicated for 30 minutes in ice water bath. The mixture was stirred overnight, then centrifuged at 8000 rpm to collect the catalyst, and washed with water for 2 times, acetone for 2 times and IPA for 2 times to remove residues in the solution.

Electrochemical measurements: A glassy carbon rotating disk electrode (RDE, Pine Research Instrumentation) connected to a bipotentiostat (Pine Research Instrumentation, model AFCBP1) was used. A leak-free AgCl/Ag/NaCl (3 M) electrode (BASi, MF-2052) was used as the reference. All potentials were converted to values with reference to a reversible hydrogen electrode (RHE). The counter electrode was a platinum wire. The electrolyte was 0.1 M perchloric acid diluted from 70% (VERITAS, double distilled) using Millipore ultrapure water.

Preparation of working electrode: For commercial Pt/C catalyst (20 wt% Pt on Vulcan XC72R carbon support; Johnson Matthey, termed JM Pt/C) and Pt MTNN (amount based on ICP-OES measurement), an aqueous dispersion was prepared and sonicated. An appropriate amount was then transferred onto the glassy carbon RDE with a geometric area of 0.196 cm^2. Generally the loading amount of metal for Pt/C catalyst and Pt MTNN was always around 3-3.5 μg Pt without a dramatic difference. After drying in air, the electrode was covered with 10 μL of 0.05 wt% Nafion solution. After dring, the electrode was put under vacuum for 2 h before measurement.

Cyclic voltammetry (CV) measurements: Cyclic voltammetry (CV) measurements were carried out in 0.1 M $HClO_4$ solutions (For oxygen reduction reaction) or 0.5 M H_2SO_4 (for methanol oxidation reaction) under a flow of N_2 (ultrahigh purity) at a sweep rate of 50 mV/s. The charge associated with H adsorption/desorption (Q_H, take average of adsorption and desorption) between 0.05 and 0.4V (vs. RHE) is measured after double-layer correction and assuming 210 μC/cm^2 for the adsorption of a monolayer of hydrogen on a Pt surface (q_H). Then, the specific ECSA was calculated:

$$ECSA = \frac{Q_H}{q_H}$$

Oxygen reduction reaction (ORR): The ORR measurements were performed in 0.1 M $HClO_4$ solutions under flow of O_2 (ultrahigh purity) using the glassy carbon RDE at a rotation rate of 1600 rpm and a sweep rate of 10 mV/s. In order to produce a clean electrode surface, several potential sweeps between 0.1 and 1.1 V versus RHE were

applied to the electrode prior to the ORR measurement. In the ORR polarization curve, current densities were normalized in reference to the geometric area of the glassy carbon RDE (0.196 cm^2). For the ORR at a RDE, the Koutecky-Levich equation can be described as follows:

$$\frac{1}{i} = \frac{1}{i_K} + \frac{1}{i_{l,c}}$$

where i is the experimentally measured current, $i_{l,c}$ is the diffusion-limiting current, and i_K is the kinetic current. Then, the kinetic current can be calculated. For each catalyst, the kinetic current was normalized to loading amount of metal and ECSA in order to obtain mass and specific activities, respectively.

Accelerated durability tests: The accelerated durability tests were performed at room temperature in O_2-saturated 0.1 M $HClO_4$ solutions by applying cyclic potential sweeps between 0.6 and 1.1 V versus RHE at a sweep rate of 50 mV/s for a given number of cycles.

Methanol electrooxidation: The methanol electrooxidation measurements were performed in the solution of 1 M CH_3OH in 0.5 M H_2SO_4 under flow of N_2 (ultrahigh purity) using stationary electrode cyclic voltammograms on a glassy carbon RDE at a sweep rate at 50 mV/s.

References

1. Debe, M. K. (2012). Electrocatalyst approaches and challenges for automotive fuel cells. *Nature*, *486*(7401), 43.
2. Tian, N., Zhou, Z. Y., & Sun, S. G. (2008). Platinum metal catalysts of high-index surfaces: from single-crystal planes to electrochemically shape-controlled nanoparticles. *The Journal of Physical Chemistry C*, *112*(50), 19801-19817.
3. Shao, Y., Yin, G., & Gao, Y. (2007). Understanding and approaches for the durability issues of Pt-based catalysts for PEM fuel cell. *Journal of Power Sources*, *171*(2), 558-566.
4. Rabis, A., Rodriguez, P., & Schmidt, T. J. (2012). Electrocatalysis for polymer electrolyte fuel cells: recent achievements and future challenges. *Acs Catalysis*, *2*(5), 864-890.
5. Koenigsmann, C., & Wong, S. S. (2011). One-dimensional noble metal electrocatalysts: a promising structural paradigm for direct methanol fuel cells. *Energy & Environmental Science*, *4*(4), 1161-1176.
6. Zhou, X. W., Zhang, R. H., Zhou, Z. Y., & Sun, S. G. (2011). Preparation of PtNi hollow nanospheres for the electrocatalytic oxidation of methanol. *Journal of Power Sources*, *196*(14), 5844-5848.
7. Yin, A. X., Min, X. Q., Zhang, Y. W., & Yan, C. H. (2011). Shape-selective synthesis and facet-dependent enhanced electrocatalytic activity and durability of monodisperse sub-10 nm Pt− Pd tetrahedrons and cubes. *Journal of the American Chemical Society*, *133*(11), 3816-3819.

8. Chen, J., Lim, B., Lee, E. P., & Xia, Y. (2009). Shape-controlled synthesis of platinum nanocrystals for catalytic and electrocatalytic applications. *Nano Today*, *4*(1), 81-95.
9. Zhou, K., & Li, Y. (2012). Catalysis Based on Nanocrystals with Well‐Defined Facets. *Angewandte Chemie International Edition*, *51*(3), 602-613.
10. Peng, Z., & Yang, H. (2009). Designer platinum nanoparticles: Control of shape, composition in alloy, nanostructure and electrocatalytic property. *Nano Today*, *4*(2), 143-164.
11. Bing, Y., Liu, H., Zhang, L., Ghosh, D., & Zhang, J. (2010). Nanostructured Pt-alloy electrocatalysts for PEM fuel cell oxygen reduction reaction. *Chemical Society Reviews*, *39*(6), 2184-2202.
12. Yu, X., Wang, D., Peng, Q., & Li, Y. (2011). High performance electrocatalyst: Pt–Cu hollow nanocrystals. *Chemical Communications*, *47*(28), 8094-8096.
13. Yin, A. X., Min, X. Q., Zhu, W., Wu, H. S., Zhang, Y. W., & Yan, C. H. (2012). Multiply twinned Pt–Pd nanoicosahedrons as highly active electrocatalysts for methanol oxidation. *Chemical Communications*, *48*(4), 543-545.
14. Guo, S., Dong, S., & Wang, E. (2009). Three-dimensional Pt-on-Pd bimetallic nanodendrites supported on graphene nanosheet: facile synthesis and used as an advanced nanoelectrocatalyst for methanol oxidation. *ACS nano*, *4*(1), 547-555
15. Koenigsmann, C., Scofield, M. E., Liu, H., & Wong, S. S. (2012). Designing enhanced one-dimensional electrocatalysts for the oxygen reduction reaction: Probing size-and composition-dependent electrocatalytic behavior in noble metal

nanowires. *The Journal of Physical Chemistry Letters*, *3*(22), 3385-3398.

16. Sun, S., Zhang, G., Geng, D., Chen, Y., Li, R., Cai, M., & Sun, X. (2011). A highly durable platinum nanocatalyst for proton exchange membrane fuel cells: multiarmed starlike nanowire single crystal. *Angewandte Chemie*, *123*(2), 442-446.
17. Menke, E. J., Thompson, M. A., Xiang, C., Yang, L. C., & Penner, R. M. (2006). Lithographically patterned nanowire electrodeposition. *Nature materials*, *5*(11), 914.
18. Chen, J., Herricks, T., Geissler, M., & Xia, Y. (2004). Single-crystal nanowires of platinum can be synthesized by controlling the reaction rate of a polyol process. *Journal of the American Chemical Society*, *126*(35), 10854-10855.
19. Ruan, L., Zhu, E., Chen, Y., Lin, Z., Huang, X., Duan, X., & Huang, Y. (2013). Biomimetic synthesis of an ultrathin platinum nanowire network with a high twin density for enhanced electrocatalytic activity and durability. *Angewandte Chemie International Edition*, *52*(48), 12577-12581.
20. Song, Y., Garcia, R. M., Dorin, R. M., Wang, H., Qiu, Y., Coker, E. N., ... & Shelnutt, J. A. (2007). Synthesis of platinum nanowire networks using a soft template. *Nano letters*, *7*(12), 3650-3655.
21. Zhang, L., Li, N., Gao, F., Hou, L., & Xu, Z. (2012). Insulin amyloid fibrils: an excellent platform for controlled synthesis of ultrathin superlong platinum nanowires with high electrocatalytic activity. *Journal of the American Chemical Society*, *134*(28), 11326-11329.

22. Hu, L., Cao, X., Chen, L., Zheng, J., Lu, J., Sun, X., & Gu, H. (2012). Highly efficient synthesis of aromatic azos catalyzed by unsupported ultra-thin Pt nanowires. *Chemical Communications*, *48*(28), 3445-3447.

23. Hu, L., Cao, X., Ge, D., Hong, H., Guo, Z., Chen, L., ... & Gu, H. (2011). Ultrathin Platinum Nanowire Catalysts for Direct C N Coupling of Carbonyls with Aromatic Nitro Compounds under 1 Bar of Hydrogen. *Chemistry-A European Journal*, *17*(50), 14283-14287.

24. Xia, B. Y., Ng, W. T., Wu, H. B., Wang, X., & Lou, X. W. D. (2012). Self‐Supported Interconnected Pt Nanoassemblies as Highly Stable Electrocatalysts for Low‐Temperature Fuel Cells. *Angewandte Chemie*, *124*(29), 7325-7328.

25. Xia, Bao Yu, et al. "Ultrathin and ultralong single-crystal platinum nanowire assemblies with highly stable electrocatalytic activity." *Journal of the American chemical Society* 135.25 (2013): 9480-9485.

26. Rendulic, K. D., Winkler, A., & Steinrück, H. P. (1987). The role of surface defects in the adsorption and sesorption of hydrogen on Ni (111). *Surface Science*, *185*(3), 469-478.

27. Vidruk, R., Landau, M. V., Herskowitz, M., Talianker, M., Frage, N., Ezersky, V., & Froumin, N. (2009). Grain boundary control in nanocrystalline MgO as a novel means for significantly enhancing surface basicity and catalytic activity. *Journal of Catalysis*, *263*(1), 196-204.

28. Lebedeva, N. P., Koper, M. T. M., Feliu, J. M., & Van Santen, R. A. (2002). Role of crystalline defects in electrocatalysis: Mechanism and kinetics of CO adlayer

oxidation on stepped platinum electrodes. *The Journal of Physical Chemistry B*, *106*(50), 12938-12947.

29. Cherstiouk, O. V., Gavrilov, A. N., Plyasova, L. M., Molina, I. Y., Tsirlina, G. A., & Savinova, E. R. (2008). Influence of structural defects on the electrocatalytic activity of platinum. *Journal of Solid State Electrochemistry*, *12*(5), 497-509.
30. Wang, Y., Chen, M., Zhou, F., & Ma, E. (2002). High tensile ductility in a nanostructured metal. *Nature*, *419*(6910), 912.
31. Chen, K. C., Wu, W. W., Liao, C. N., Chen, L. J., & Tu, K. N. (2008). Observation of atomic diffusion at twin-modified grain boundaries in copper. *Science*, *321*(5892), 1066-1069.
32. Li, Y., Whyburn, G. P., & Huang, Y. (2009). Specific peptide regulated synthesis of ultrasmall platinum nanocrystals. *Journal of the American Chemical Society*, *131*(44), 15998-15999.
33. Li, Y., & Huang, Y. (2010). Morphology‐controlled synthesis of platinum nanocrystals with specific peptides. *Advanced Materials*, *22*(17), 1921-1925.
34. Dickerson, M. B., Sandhage, K. H., & Naik, R. R. (2008). Protein-and peptide-directed syntheses of inorganic materials. *Chemical reviews*, *108*(11), 4935-4978.
35. Chiu, C. Y., Ruan, L., & Huang, Y. (2013). Biomolecular specificity controlled nanomaterial synthesis. *Chemical Society Reviews*, *42*(7), 2512-2527.
36. Briggs, B. D., & Knecht, M. R. (2012). Nanotechnology meets biology: peptide-based methods for the fabrication of functional materials. *J. Phys. Chem.*

Lett, *3*(3), 405-418.

37. Chiu, C. Y., Li, Y., Ruan, L., Ye, X., Murray, C. B., & Huang, Y. (2011). Platinum nanocrystals selectively shaped using facet-specific peptide sequences. *Nature chemistry*, *3*(5), 393-399.
38. Ruan, L., Chiu, C. Y., Li, Y., & Huang, Y. (2011). Synthesis of platinum single-twinned right bipyramid and {111}-bipyramid through targeted control over both nucleation and growth using specific peptides. *Nano letters*, *11*(7), 3040-3046.
39. Markovic, N. M., Gasteiger, H. A., & Ross Jr, P. N. (1995). Oxygen reduction on platinum low-index single-crystal surfaces in sulfuric acid solution: rotating ring-Pt (hkl) disk studies. *The Journal of Physical Chemistry*, *99*(11), 3411-3415.
40. Markovic, N. M., Schmidt, T. J., Stamenkovic, V., & Ross, P. N. (2001). Oxygen reduction reaction on Pt and Pt bimetallic surfaces: a selective review. *FUEL CELLS-WEINHEIM-*, *1*(2), 105-116.
41. Peng, Z., You, H., & Yang, H. (2010). Composition-dependent formation of platinum silver nanowires. *ACS nano*, *4*(3), 1501-1510.
42. Yuk, J. M., Park, J., Ercius, P., Kim, K., Hellebusch, D. J., Crommie, M. F., ... & Alivisatos, A. P. (2012). High-resolution EM of colloidal nanocrystal growth using graphene liquid cells. *Science*, *336*(6077), 61-64.
43. Gao, B., Arya, G., & Tao, A. R. (2012). Self-orienting nanocubes for the assembly of plasmonic nanojunctions. *Nature nanotechnology*, *7*(7), 433-437.
44. Li, Y., Li, Y., Zhu, E., McLouth, T., Chiu, C. Y., Huang, X., & Huang, Y. (2012).

Stabilization of high-performance oxygen reduction reaction Pt electrocatalyst supported on reduced graphene oxide/carbon black composite. *Journal of the American Chemical Society*, *134*(30), 12326-12329.

45. Qin, G. W., Pei, W., Ma, X., Xu, X., Ren, Y., Sun, W., & Zuo, L. (2010). Enhanced catalytic activity of Pt nanomaterials: from monodisperse nanoparticles to self-organized nanoparticle-linked nanowires. *The Journal of Physical Chemistry C*, *114*(15), 6909-6913.
46. Lee, I., Albiter, M. A., Zhang, Q., Ge, J., Yin, Y., & Zaera, F. (2011). New nanostructured heterogeneous catalysts with increased selectivity and stability. *Physical Chemistry Chemical Physics*, *13*(7), 2449-2456.

Chapter 4 Anisotropic nanocrystal growth and assembly driven by molecular structural transformation

Introduction

As mentioned in Chapter 2 and 3, specific surfactant molecules have been widely employed to manipulate the morphologies and assemblies of nanostructures.[1-3] To move beyond the conventional trial-and-error approach and to accelerate the discovery of suitable material-specific molecules for exquisite synthetic control of material structures, methods inspired from molecular evolution in biochemistry have been devised to effectively identify artificial biomolecules which have highly specific surface recognition properties, leading to excellent morphology control of nanocrystals (NCs).[4-11] Beyond morphology control to hierarchical assembly of NCs is another significant challenge in nanotechnology.[16-23] Several excellent strategies, involving DNA linkers[24,25], block co-polymers[26,27] or patchy particle[18,28,29], have led to NC assemblies which were hardly accomplished before. Nevertheless, most efforts have been focusing on the discovery and utilization of the primary structure of material specific (bio)molecules in the control of crystal morphology. The roles of HOS remain largely unexplored in material structure creation.[12-15]

Results and Discussions

Pt{100}-specific peptide and its HOSs was shown to play important roles in both the

shape control of cubic NC growth and their following anisotropic assembly into long-range one-dimensional (1-D) lines. (Figure 4.1) To our knowledge, this is the first demonstration showing HOSs of biomolecules can be harvested to impact material structure formation. The Pt{100}-facet-specific peptide T7 (sequence Ac-TLTTLTN-$CONH_2$; T, Threonine; L, Leucine; N, Asparagine) was identified using phage display technique.[10] However, calculation based on the primary structure of T7 gives a positive adsorption energy (~ +13 kcal/mol) between T7 and extended Pt{100} facet, indicating T7 does not favor Pt{100}.[35] Such conflict between the experiment and the simulation points out that other factors exist dominating the Pt{100} specificity of T7. On the other hand, independently folded HOSs, besides the commonly seen random coils,[36] are structurally viable in short peptides.[37-42] Indeed, our experimental results show that ST-turn HOS dominates in T7 at low peptide concentration while β-sheet HOS is favored at high concentration. (Figure 4.1) Taking the ST-turn HOS into account, the calculated Pt{100} adsorption energy of T7 renders a negative value of -1.46±0.96 kcal/mol, (Figure 4.2) suggesting preferential T7-Pt{100} binding and encourages the cube growth of Pt NCs. We further observe that after cubic NCs are synthesized, long-range 1-D assemblies with the average length reaching tens of micrometers (10s' μm) can be obtained by simply increasing the T7 concentration, much longer than those previously reported.[16-22] Both the crystal growth and assembly process are directed by the molecular-NC specific interactions and can be controlled *in-situ* without involving complicated surface modification of the NCs. The coordinate system is assigned as in Figure 4.1, where the 1-D

assemblies are in *x*-*y* plane and assembled along *y* direction.

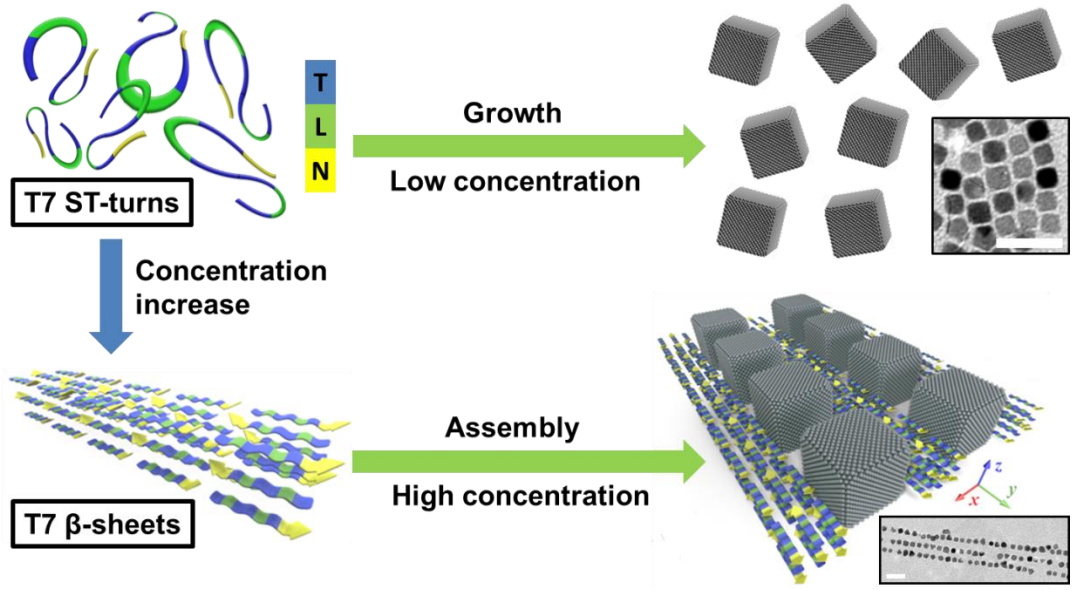

Figure 4.1 T7 conformation change from low concentration (ST-turns, leading to Pt cube synthesis) to high concentration (β-sheets, leading to Pt cube 1-D assembly). Blue represents T, green L, and yellow N. The scale bars are 20 nm.

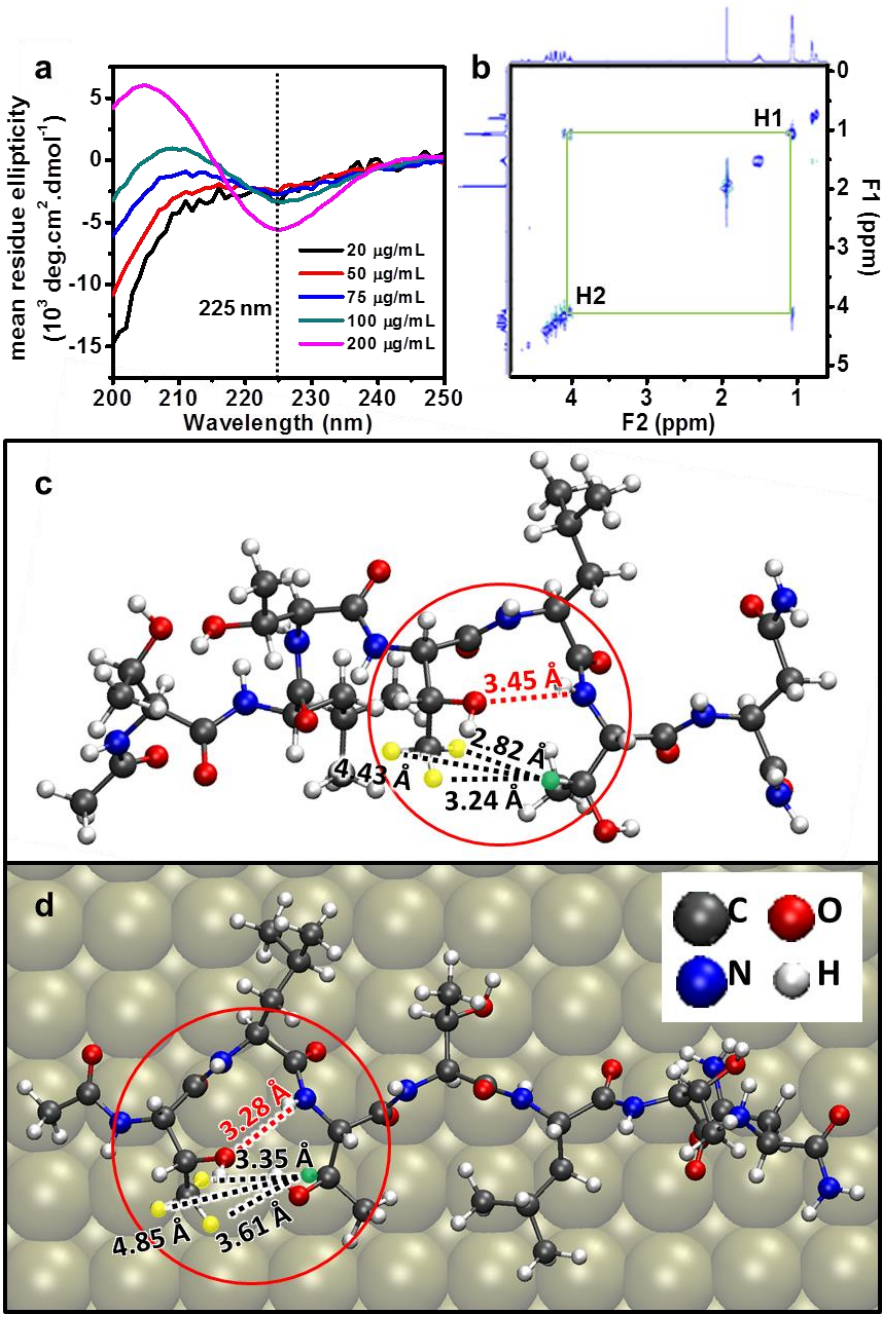

Figure 4.2 T7 adopts ST-turns under low concentration. (a) the CD spectra of T7 in H_2O at different concentrations. (b) NOESY of 20 μg/mL T7 in D_2O. (c-d) Simulated T7 peptide structures relaxed (c) in H_2O, and (d) on Pt {100} facets. ST-turns are highlighted in red circles. Distances between N and O in the hydrogen bonds are represented with red dashed lines. Distances between H2 (green) and multiple H1's (yellow) involved in NOE are represented with black dashed lines. Adsorption energy

of T7 on Pt{100} is -1.46±0.96 kcal/mol.

The presence and dominance of T7 turn structures at low concentration are suggested by the valley at ~225 nm (Figure 4.2a) in the circular dichroism (CD) spectra (aqueous T7 solutions from 20 μg/mL to 200 μg/mL, room temperature, pH=7),[43] and confirmed by the amide I band of 100 μg/mL T7 in Fourier transform infrared spectroscopy (FTIR), where the wavenumber of the deconvoluted peaks clearly show the dominance of turn as the secondary structure.[44] (Figure 4.3a) Since a single TLT unit has two threonine residues at both ends, T7 is very likely to form an ST-turn structure within each TLT unit and expresses the characteristic spatial relationship of two close threonines as confirmed by the nuclear Overhauser effect spectroscopy (NOESY), where the cross peaks of H1 in one threonine and H2 in another threonine (Figure 4.2b and 4.2c) at 20 μg/mL of T7 in D_2O suggest that the hydrogen atoms are spatially close. This spatial adjacency automatically excludes the possibility of β-turns due to steric hindrance. Our simulation results, consistent with experimental observations (Figure 4.4), demonstrate a stable ST-turn conformation with H-bonds formed within a TLT unit for T7 molecules both relaxed in water (3.45 Å H-bond in ST-turn, 2.82-4.43 Å H1-H2 distance, Figure 4.2c) and on Pt{100} surface (3.28 Å H-bond in ST-turn, 3.35-4.85 Å H1-H2 distance, Figure 4.2d).

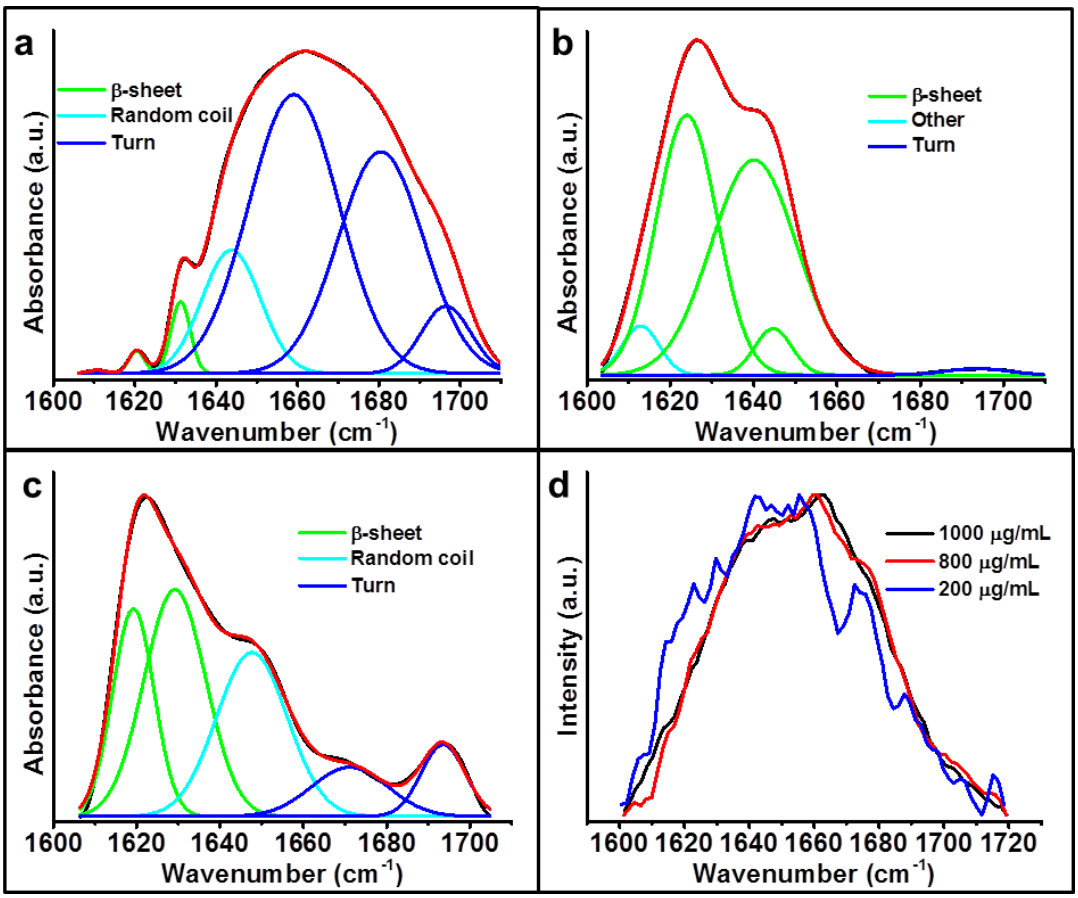

Figure 4.3 Raman spectroscopies and Fourier self-deconvolution (FSD) processed Fourier transform infrared spectroscopies (FTIR) of T7 in different states. (a) The amide I band in the FTIR of 100 μg/mL T7 frozen in liquid ethane and freeze-dried. (b) The amide I band in the FTIR of slowly dried T7 sheets. (c) The amide I band in the FTIR of linearly aligned NCs embedded in T7 sheets. (d) *In-situ* UV-Raman spectra of aqueous T7 at different concentrations.

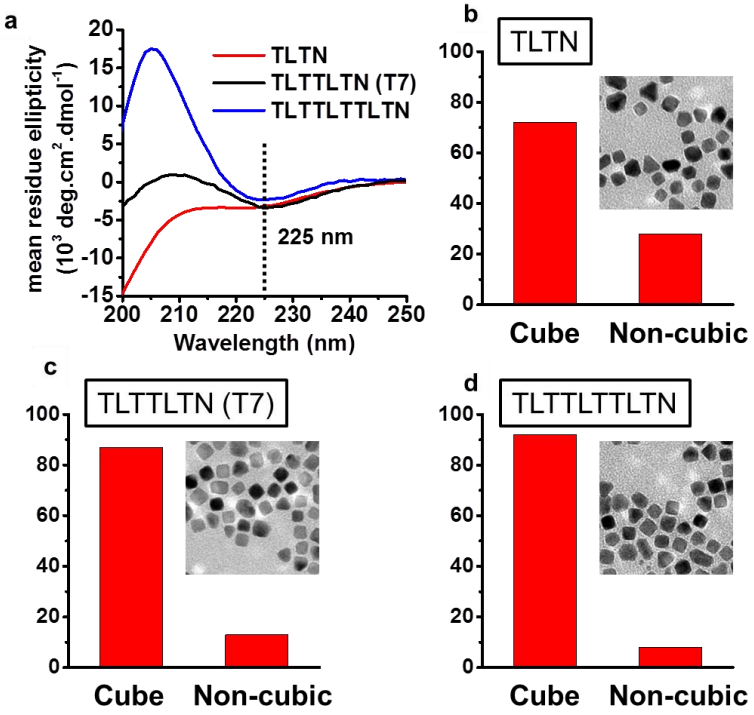

Figure 4.4 Positive correlation of the amounts of ST turns and TLT units. (a) CD spectra of the peptides (100 μg/mL). (b-d) Ratios of different morphologies of each peptide with corresponding TEM images of NCs all synthesized in 20 ug/mL peptides.

Nuclear Overhauser effect spectroscopy (NOESY) shows that H bonds are formed between two threonines in T7. In one scenario (Scenario 1), the threonines forming H-bonds are within individual TLT units and the number of H-bonds formed is proportional to the number of TLT units. In another scenario (Scenario 2), the threonines forming H-bonds are across individual TLT units and only 1 H-bond are formed in each peptide no matter how many TLT units exist.

T7 variants with different number of TLT units (Ac-TLTN-$CONH_2$, M_w=488.54,

termed $T_1$7; Ac-(TLT)$_2$N-CONH$_2$, M_w=803.9, T7; Ac-(TLT)$_3$N-CONH$_2$, M_w=1119.27, termed $T_3$7) were designed to determine where the H-bonds were formed in the ST-turns (Figure S2). ST-turn structure was demonstrated to yield cubic NCs in the synthesis so the percentage of cubic NCs was used as an indicator to refer how many ST-turns were formed in the peptide.[6] During the synthesis of NCs, a constant mass concentration (20 ug/mL) is kept for all peptides.

In Scenario 2, the ratio of the ST-turn formed in $T_1$7, T7 and $T_3$7 should be:

$$\frac{1}{488.54}:\frac{1}{803.9}:\frac{1}{1119.27} = 1:0.61:0.44$$

It's decreasing from $T_1$7 to $T_3$7. However as shown in Figure S2, the ratio of the percentage of cubic NCs in $T_1$7, T7 and $T_3$7 is:

$$72:87:92 = 1:1.21:1.28$$

It's increasing from $T_1$7 to $T_3$7. Thus Scenario 2 is not reasonable and gets excluded.

In Scenario 1, the ratio of the ST-turn formed in $T_1$7, T7 and $T_3$7 should be:

$$\frac{1}{488.54}:\frac{2}{803.9}:\frac{3}{1119.27} = 1:1.22:1.31$$

It's increasing from $T_1$7 to $T_3$7. The ratio of the percentage of cubic NCs from $T_1$7 to $T_3$7 is:

$$72:87:92 = 1:1.21:1.28$$

They have the same increasing trend and the ratios matches well with each other. Thus Scenario 1 is reasonable and accepted. It demonstrates the H-bonds are formed within individual TLT units.

Additional experiments were performed to further confirm that the ST-turn in T7 directly leads to Pt{100} specific binding and Pt cubic NC formation. First, we tested the temperature dependence of Pt NC formation. As expected with increasing reaction temperature, Pt nanocube morphology gradually disappear while entropy-favored random coils emerge instead of the peptide ST-turns, as well as, hampering the formation of cubic NCs.[46] (Figure 4.5). This is consistent with prior studies showing that proteins[45] and short peptides[39-41] will unfold due to the break of H-bonds when temperature increases. As temperature variation may directly impact peptide binding strength to Pt surface, we deliberately designed a set of T7 variants to investigate the contributions of amino acid residues on ST-turn formation and on peptide's recognition to platinum {100} recognition at room temperature (25 ºC). (Figure 4.6) The two leucine residues in T7 were replaced with other amino acids with different hydrophobicities and steric hindrances, such as valine (Ac-TVTTVTN-$CONH_2$, termed T7-V), alanine (Ac-TATTATN-$CONH_2$, termed T7-A) and glycine (Ac-TGTTGTN-$CONH_2$, termed T7-G) to examine the effect of hydrophobic aliphatic amino acids (Figure 4.6a). With the CD spectra (Figure 4.6g), T7-V was found similar to T7, adopting ST-turns, while T7-A and T7-G were mostly random coils. The structural distinction implied that the isopropyl groups in L and V were decisive in terms of high hydrophobicity and steric hindrance. All four T7 variants were then used to synthesize Pt NCs under the same reaction condition. The T7-V-mediated NCs were characterized as cubes by transmission electron microscopy

(TEM) whereas cuboctahedra prevailed in the T7-A- and T7-G-mediated NCs. (Figure 4.6b-e) The characterization results and our assertion that the cubic morphology of NCs is favored by ST-turns rather than random coils strongly agreed. The variant T7-S (Ac-SLSSLSN-$CONH_2$) was also employed (Figure 4.6a) to examine the role of T. In this case, the secondary structure is no longer ST-turn but random coil, meaning that T is more critical in ST-turn formation than S. The hydroxyl group in the side chain of T was pushed to a position in favor of the formation of H-bonds to overcome the steric hindrance due to the methyl group on the beta carbon. (Figure 2c-d) TEM images also showed that T7-S yielded cuboctahedral instead of cubic NCs, (Figure 4.6f) confirming the correlation between ST-turns and Pt{100} recognition in cube production. The structures of those variants (T7-V, T7-G, T7-A and T7-S) were also relaxed on Pt {100} facets in simulation, the results also indicates only T7-V still preserve ST-turn. (Figure 4.7)

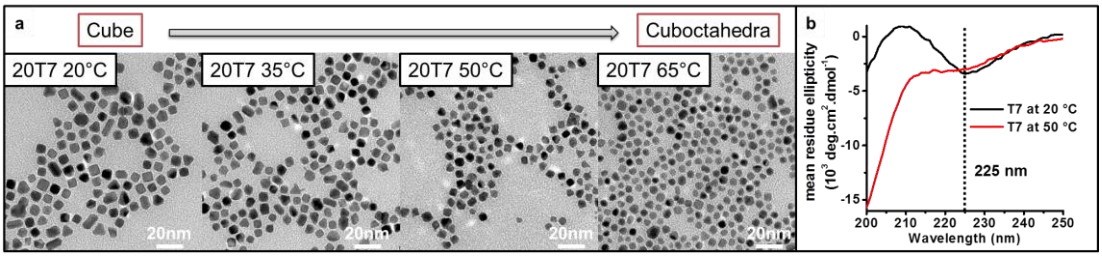

Figure 4.5 NC morphologies change from cubic to cuboctahedral and the turn structure fades as temperature increases. (a) TEM images of NCs all synthesized in 20 ug/mL T7 under different temperatures. (b) CD spectra of T7 (100 μg/mL) at 20 ºC (turn) and 50 ºC (random coil).

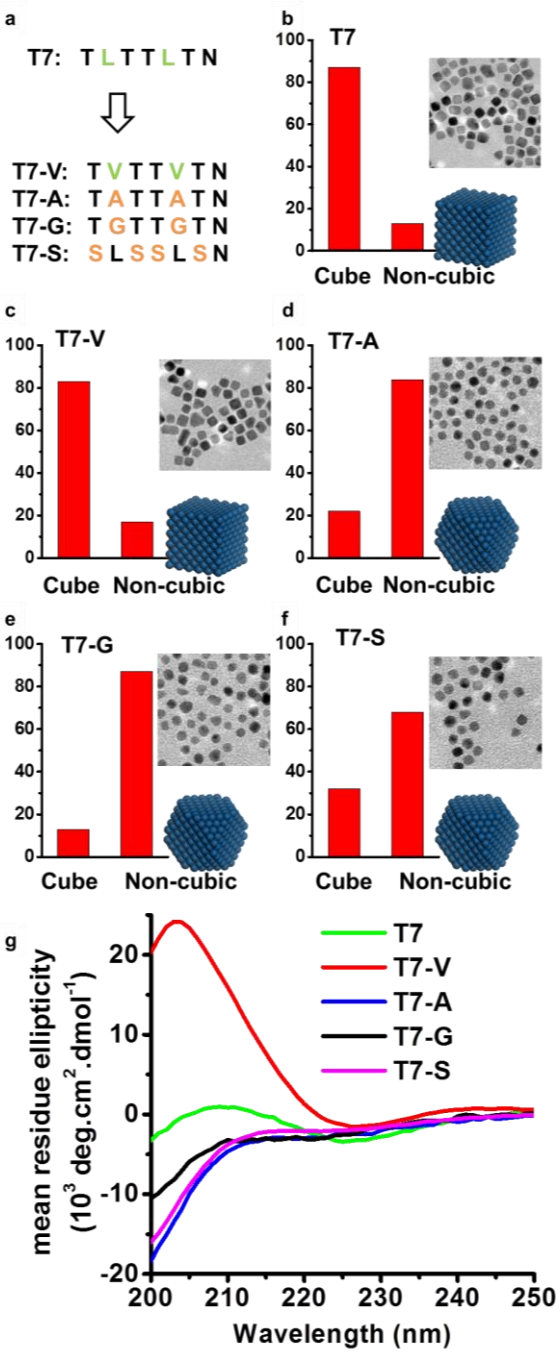

Figure 4.6 Illustration of the impacts of peptide primary structure to peptide HOS conformation and NC morphology. (a) T7 variants with different hydrophobic residues (V, A, and G) substituting L or with S substituting T. (b-f) Ratios of different morphologies of each peptide with corresponding TEM images of NCs. (g) CD spectra of T7 and T7 variants (100 μg/mL).T7 and T7-V have typical turn structures and T7-A, T7-G, T7-S are random coils.

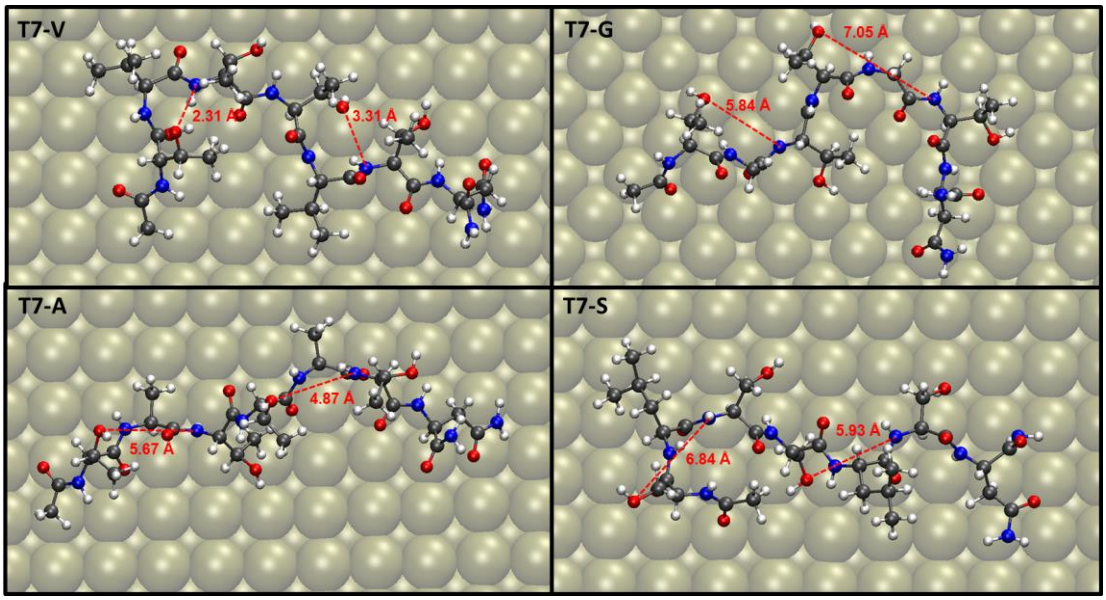

Figure 4.7 Simulated T7 variants' structures relaxed on Pt {100} facets. Distances between N and O in the hydrogen bonds are represented with red dashed lines. T7-V shows ST-turn structures while in T7-A, T7-G and T7-S the N-O distance is too far to form ST-turns, instead they have random coil structure.

More interestingly, with increased T7 concentration, *in-situ* UV-Raman spectroscopy of aqueous T7 solution shows high wavenumber shift and bolsters that the secondary structure of T7 switches from ST-turns to β-sheets as the concentration goes up. (Figure 4.3d) The shift of the amide I band from the low wavenumber at 200 μg/mL T7 to the high wavenumbers at 800 μg/mL and 1000 μg/mL indicates the transformation from ST-turns to β-sheets.[47] This concentration-dependent transformation is also confirmed by the amide I bands in FTIR, where the wavenumbers of the deconvoluted peaks clearly show the dominance of turn in 100 μg/mL T7 changes to β-sheet in slowly dried T7.[44] (Figure 4.3a-b) We suggested that

ST-turns form at low T7 concentration because the peptide molecules are at a distance so that most hydrogen bonds are intramolecular and the effect of intermolecular forces is negligible. However, at high T7 concentration the intermolecular hydrogen bonds dominates, and as a result large β-sheets become energetically favorable. Indeed the fringes of dry T7 β-sheets are clearly observable under high resolution TEM (HRTEM). (Figure 4.8) The TEM image of slowly dried T7 β-sheets in Figure 3a shows a characteristic striped pattern. The striped pattern comprises of well aligned β-strand structures whose linearity can be identified by the two conspicuous opposite points in the diffraction pattern of β-sheets (Figure 4.8c). The HRTEM images of T7 β-sheets (Figure 4.8b, d, e) further showed that the average distance between two adjacent strands is 0.49±0.1 nm (Figure 4.8d), approximately equal to our simulation result (Figure 4.8e) and the reported value of the length of hydrogen bonds between amide groups ~ 0.5 nm.[50]

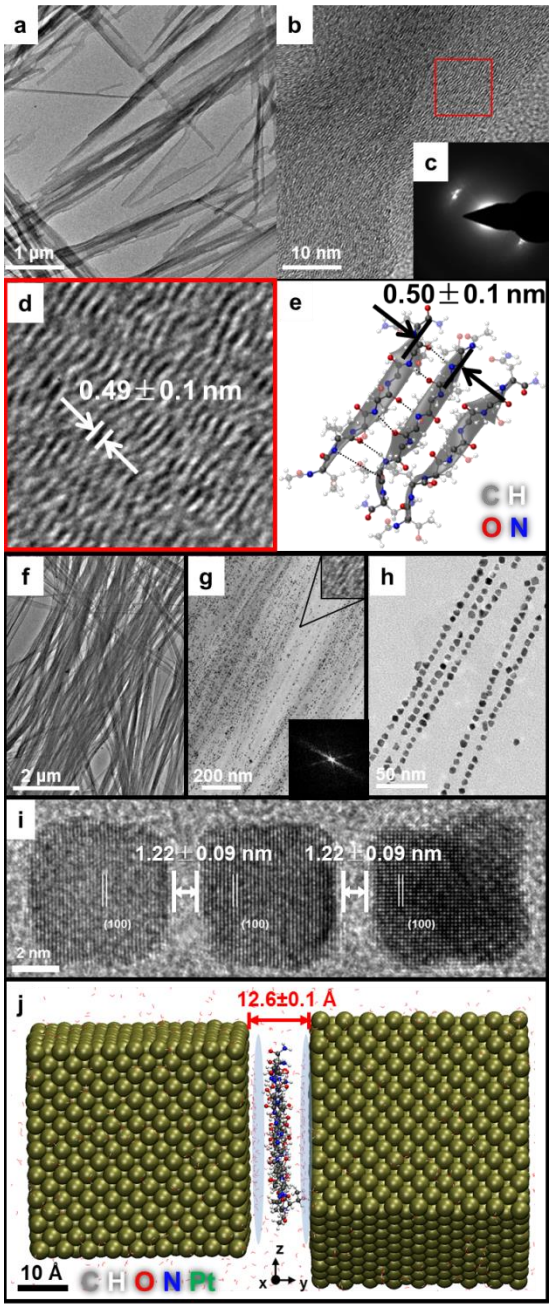

Figure 4.8 T7 serving as templates to directionally align NCs in the <100> direction. (a) TEM image of slowly dried T7 β-sheets. (b) HRTEM image of slowly dried T7 β-sheets. (c) Diffraction pattern of (b). (d) Magnified HRTEM image of the area squared red in (b). (e) Ball-and-stick model of (d). (f-h) TEM images of 1-D assembled NCs under different magnifications. The bottom-right inlet in (g) is the corresponding FFT. The top-right inlet in (g) is the striped pattern of β-sheets. (i)

HRTEM image of adjacent nanoparticles linear assembled along <100> with regular intercrystal spacing. (j) 2 Pt nanocubes adsorbed together in simulation. Water molecules form a strongly adsorbed interlayer between metal surfaces and peptides (highlighted in blue shading). The distance between the two adsorbed Pt NCs is 12.6±0.1 Å.

The large scale assembly of T7 into β-sheets driven by pure H-bond formation is interesting. We note there are reports of lucid approaches leading to peptide assembly based on π-π stacking to acquire complicated ordered biomolecule macrostructures.[49] In natural biosystems nevertheless H-bonds rather than π-π stacking is the typical construction mechanism that drives the formation of hierarchical assemblies. Using H-bonds to drive assembly of molecules and materials also provides added advantages of its configurability by simply pH tuning. For example, at pH=3 and 500 μg/mL T7 mainly exist as ST-turns while at pH=12 they form β-sheets. (Figure 4.9) The threonine hydroxyl group with an acid dissociation constant (pKa) of ~13 can be ionized in a pH=12 environment and form ionic bonds rather than hydrogen bonds which are necessary in forming ST-turns.[48] Consequently even with a relatively low T7 concentration predominance of β-sheets is possible at high pH. This provides us expanded space to regulate molecular assembly and molecular-directed materials assembly.

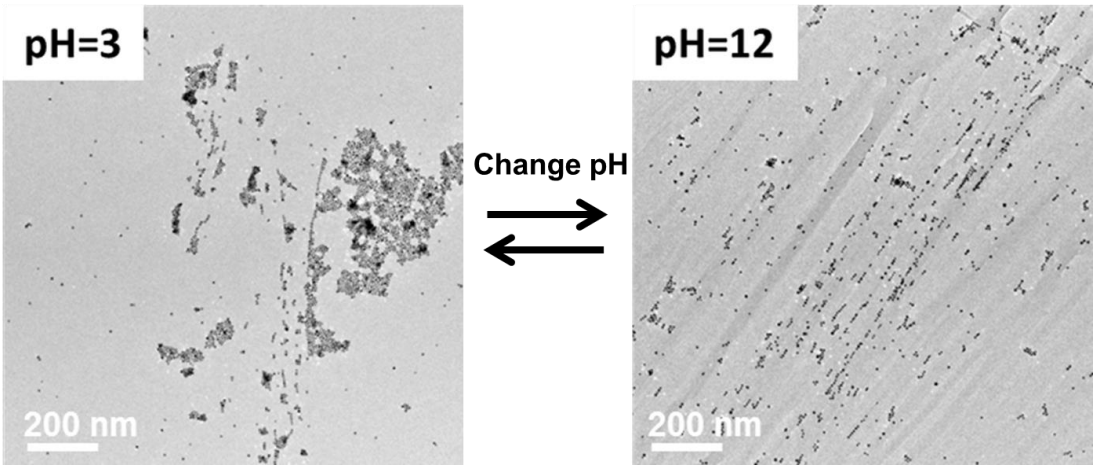

Figure 4.9 Superstructures of NCs incubated in 500 μg/mL T7 under different pH. The assembly and the disassembly of NCs are reversible as pH changes.

Significantly, when T7 under high concentration self-assemble into β-sheets, this process automatically assembles Pt NCs into long 1-D chains. Well-dispersed cubic Pt NCs incubated in 1000 μg/mL T7 with temperature dropping from 45 ºC to 20 ºC in 2 hours will gradually align in the [100] direction with evident linearity (Figure 4.8f-i, 4.10). The average length of the assemblies is about tens of micrometers, which is much longer than previous reported numbers.[16-22] 200 sets of two closely neighboring nanocrystals were examined and the spacing between two closely packed nanocrystals was estimated at 1.22±0.09 nm (Figure 4.8h-i). However, two neighboring NCs are not necessarily "close-packed" and their spacing can be much greater than 1.22 nm. Interestingly, the appearance of distant non-closely-packed spacing does not prevent NCs from displaying a perfectly straight linear structure (Figure 4.8h). The cryo-TEM image of samples made from frozen solutions, confirm that NCs indeed assemble homogeneously in the solution rather than heterogeneously on solid surface during the

drying process. (Figure 4.11) In addition, FTIR of a slowly dried sample including T7 and Pt NCs shows β-sheets still dominate as the T7 secondary structure, indicating the 1-D assemblies of Pt NCs were guided/templated by T7 β-sheets. (Figure 4.3c)

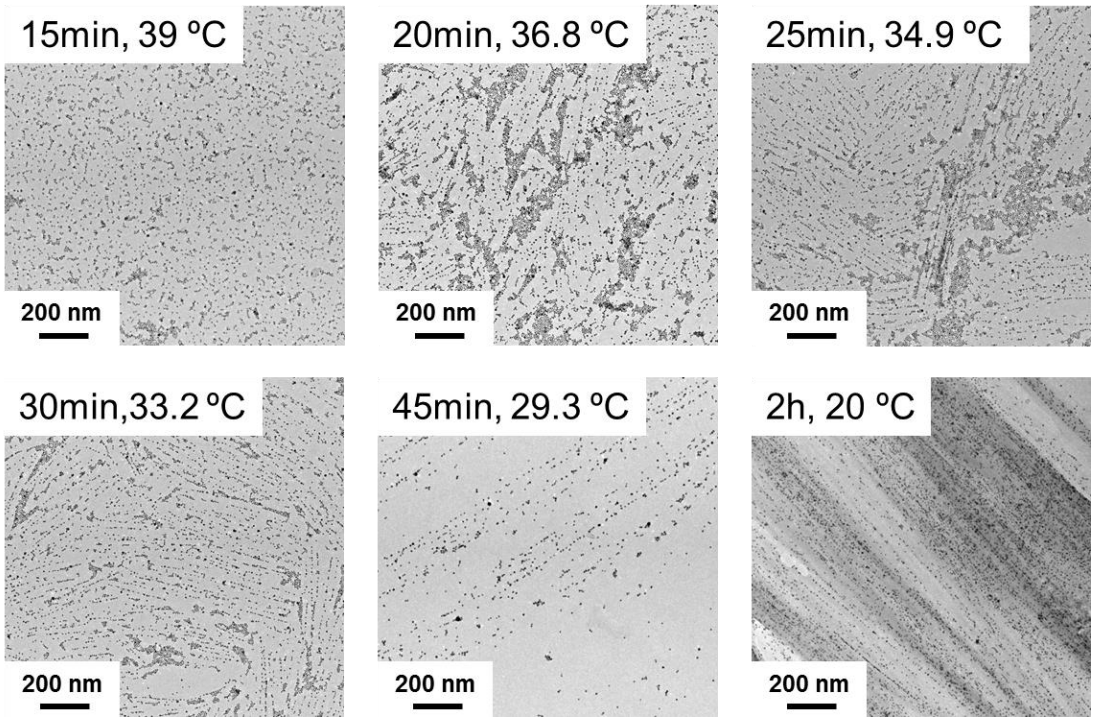

Figure 4.10 Time evolution study indicates how the 1-D assemblies are formed during the annealing process from 45 ºC to 20 ºC in 2 hours.

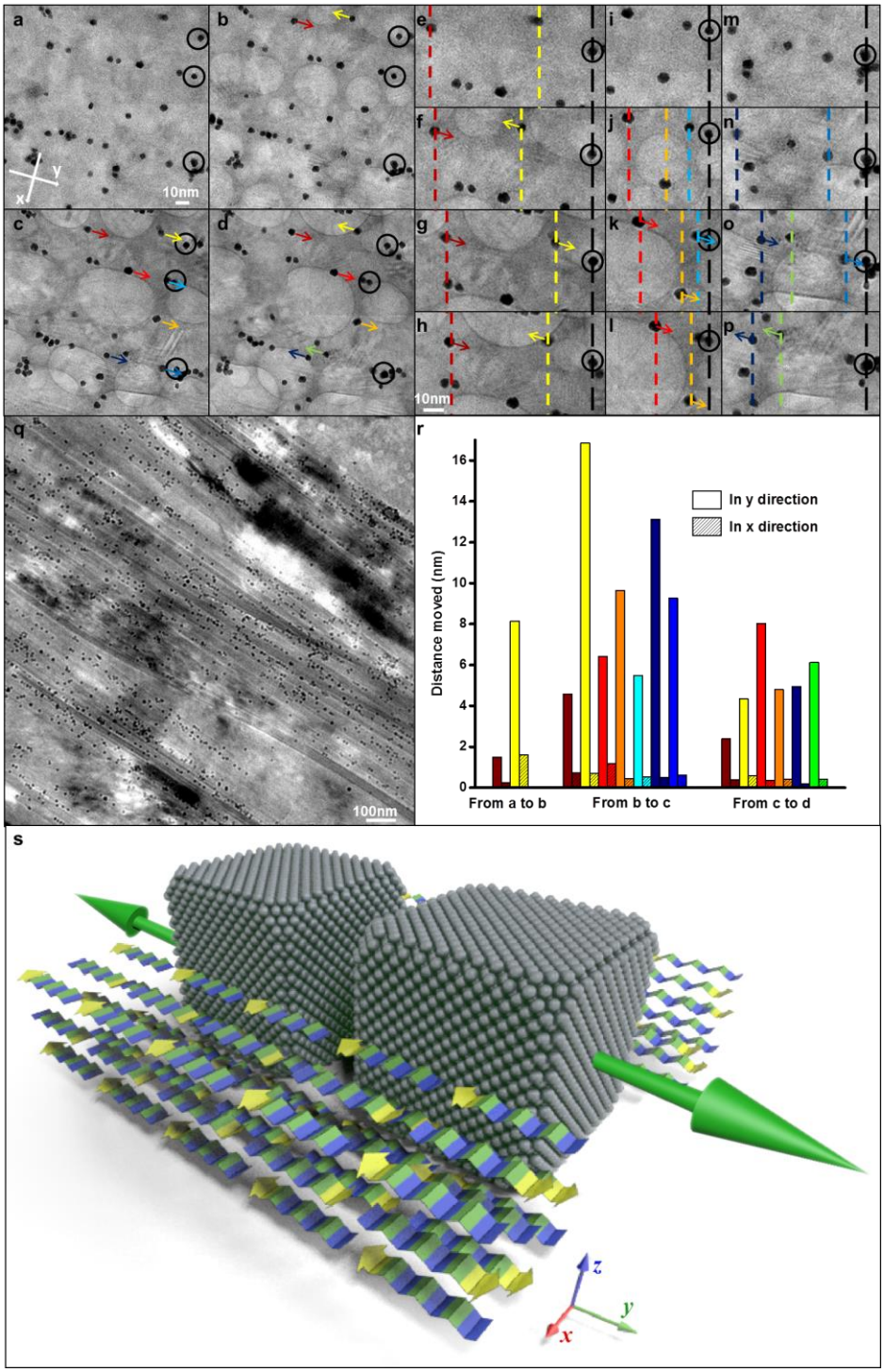

Figure 4.11 Cryo-TEM images, statistical data, and a slide model showing NCs assemble in solution and can move along one-dimensionally the linear assemblies as in a T7 β-sheets slideway. (a-d) Chronological cryo-TEM images of 1-D assembled NCs. Slow melting of the frozen sample exposed to high-energy incident electron beam enables NCs to move. The coordinate system is indicated in (a) with the

assembly directions along the *y* axis. Position reference NCs are circled and lined up with black dashed lines for comparisons of chronological positions of selective NCs in images (e-h) (wine and yellow), (i-l) (red, orange, and cyan), and (m-p) (navy, green, and blue). (q) A cryo-TEM image at lower magnification. The linearity of NC assemblies and peptides is conspicuous. (r) Statistics of the NC displacements show a highly preferred *y*-oriented (i.e. assembly direction oriented) movement. (s) A slide model. T7 β-sheets are constituted into a slideway in which NCs can move freely. Flexible T7 ST-turns on the NC surfaces (not marked) serve as the "lubricant" between the slideway and NCs.

Concisely, three factors largely determine the assembly of NCs, T7 concentration (Figure 4.12), pH (Figure 4.9) and temperature (Figure 4.13). Cubic Pt NCs cannot align neatly to form linear structures at high temperature or in an environment with either a T7 concentration lower than 800 μg/mL or low pH because adverse effects on β-sheets formation emerge. When temperature is high, entropy dominates and hydrogen bonds are disturbed. β-sheets therefore are no longer competitive with entropy-favored structures such as random coils.[45] As temperature gradually decreases while cubic Pt NCs are being incubated, a low temperature gradient could prevent rapid β-sheet formation and enable better relaxation of the interaction between NCs and T7, (Figure 4.10) while a high temperature gradient (from 45 ºC to 20 ºC in 3 min), on the contrary, only yields NCs without distinguishable assembly structures due to insufficient relaxation time. (Figure 4.13) Remarkably, it is found that with

temperature varying between 45 °C and 20 °C or at a pH from 3 to 12, the NC assembly process is reversible (Figure 4.9-4.10).

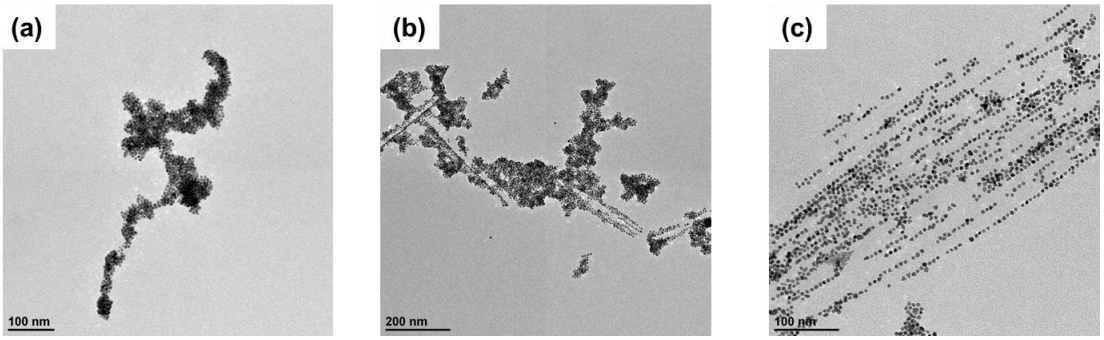

Figure 4.12 NCs assemblies at 20 ˚C and (a) 100 μg/mL, (b) 300 μg/mL, (c) 800 μg/mL T7. Linear structures appear only when the peptide concentration is high enough.

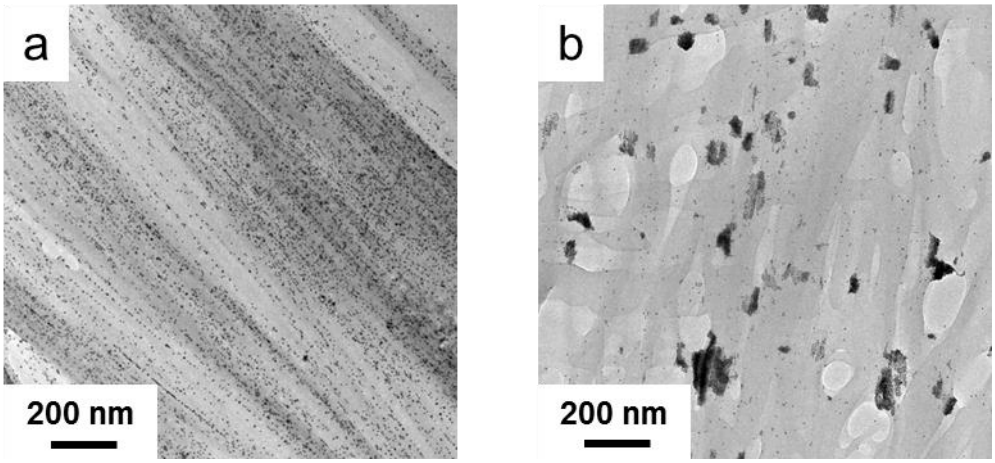

Figure 4.13 Incubation of NCs in 1000 μg/mL T7 with temperature dropping form 45 ºC to 20 ºC in (a) 2h (b) 3 min. Different incubating temperature gradients lead to different T7 structures and NC patterns.

The linear 1-D assemblies of Pt NCs are evidenced by observing the NC 1-D

movement along the assembly direction (*y* axis) in cryo-TEM, further confirming directional interactions between the Pt nanocube surface and T7 β-sheets. (Figure 4.11) Simulation studies were performed to shed light on the interactions between T7 β-sheets and the Pt cube assembly. Two possible interaction directions were studied. In one model cubic NCs approach β-sheets in the direction that Pt-{100} surface is perpendicular to the β-sheets (side chains of beta strand are parallel to the surface), in the other model the β-sheets are parallel to the {100} surface (side chains of beta strand are perpendicular to the surface). Experimentally the perpendicular β-sheets are believed to be adopted because the assembly has the same direction with the β-sheet strip of which the configuration is directly observed under HRTEM. (Figure 4.8d, 4.8e and 4.8g) The computational studies show that the perpendicular β-sheets are more stable on Pt-{100} surface. (Figure 4.14) The parallel side chains in perpendicular β-sheets take less room in *x* direction, which facilitates H-bond formation between two peptides backbones allowing them to stack in *x* direction. Interestingly, it was found that the bottom T7 layer of the β-sheets on bare Pt-{100} surface spontaneously change from the initially given β-sheet structure to ST-turn structure after relaxation (Figure 4.15), which is consistent with that ST-turn is the stable T7 structure on Pt{100} (Figure 4.2d). Such parallel side chain conformation in perpendicular β-sheets hence also favors the hydrogen bonds with the T7 ST-turns on Pt NC surface to stabilize the entire system. (Figure 4.2d) Simulation studies conducted on two close-packed adjacent cubic NCs suggested that the close-packed Pt cubic NCs most likely assemble with a layer of T7 ST-turns with parallel side chain to Pt{100}

surfaces between them, (Figure 4.16) wherein the distance between the two NCs is 12.6±0.1 Å, corresponding well with the TEM observation of 12.2±0.9 Å. (Figure 4.8j, Figure 4.17-4.18) These studies indicate that in order to guide Pt NC assembly in 1-D not only the assembly of T7 into β-sheet structure is important, but the specific interactions between the Pt{100} and T7 is also important. Indeed, our control experiments of incubating T7 with S7 wrapped-Pt nanotetrahedra, render no 1-D assemblies of Pt nanotetrahedra lines (Figure 4.19), possibly due to the nonmatching interfacial interactions between S7-T7. To expand the ability of T7 assembly we artificially wrapped Au and Pd NCs in T7 using C-T7 (CTLTTLTN), and examined their assembly behaviors. We showed that the well-dispersed uniform gold (Au) and palladium (Pd) NCs can be synthesized and assembled with C-T7 (Figure 4.20). Herein, the C residue of C-T7 contains a thiol group and readily binds to Au and Pd NC surfaces, while the T7 can interact with the T7 β-sheets, assisting 1-D alignment of Pd and Au NCs.

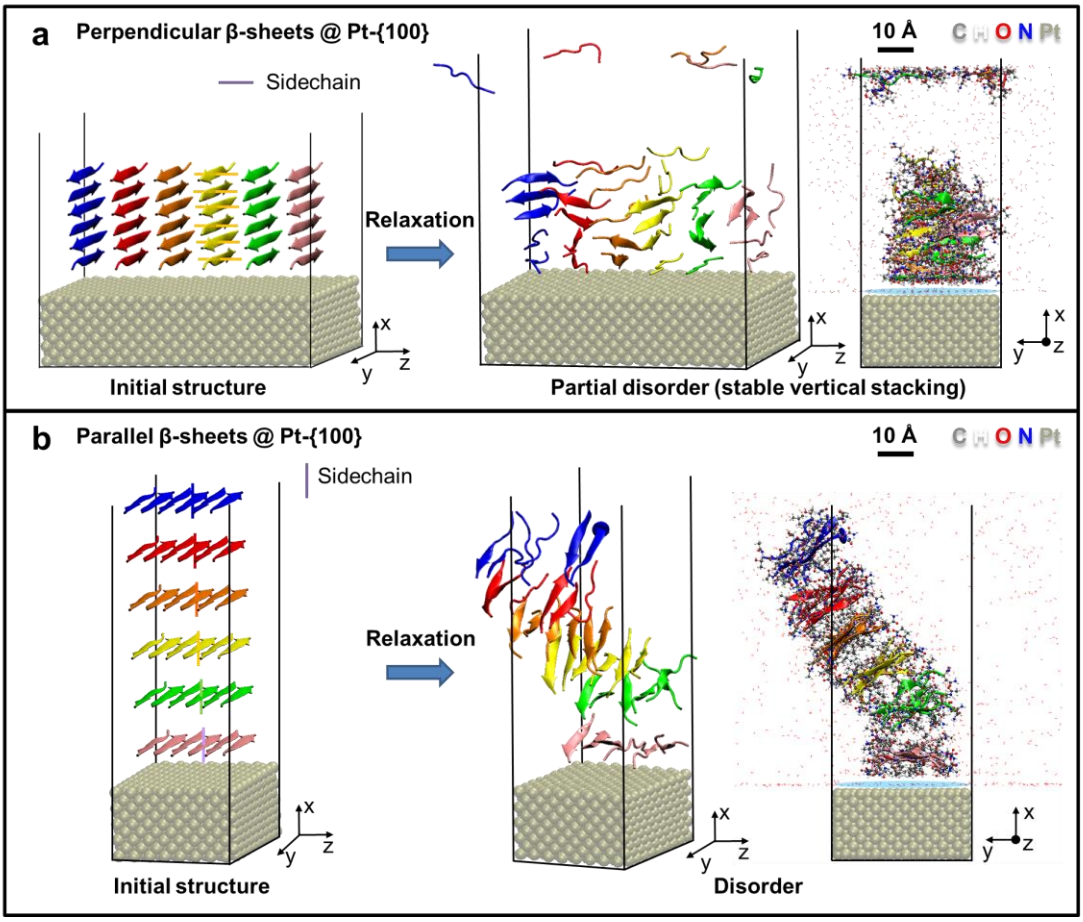

Figure 4.14 Comparison of T7 secondary structures on Pt-{100} surfaces. (Pt NCs are aligned in the *y* direction) (a) Six perpendicular T7 β-sheets and (b) six parallel T7 β-sheets are relaxed on Pt {100} extended surfaces. Sidechains of the yellow peptide strands are shown in the initial structures. A layer of water highlighted in light blue is between the Pt NC surface and the peptides in both (a) and (b). At equilibrium, (a) perpendicular β-sheets largely retain their stacking in the *x* direction, but (b) parallel β-sheets, except the very inner tier, are detached from NCs and diffuse into the solution. Representative snapshots are shown in two view angles. Water molecules are hidden for visual clarity in some snapshots.

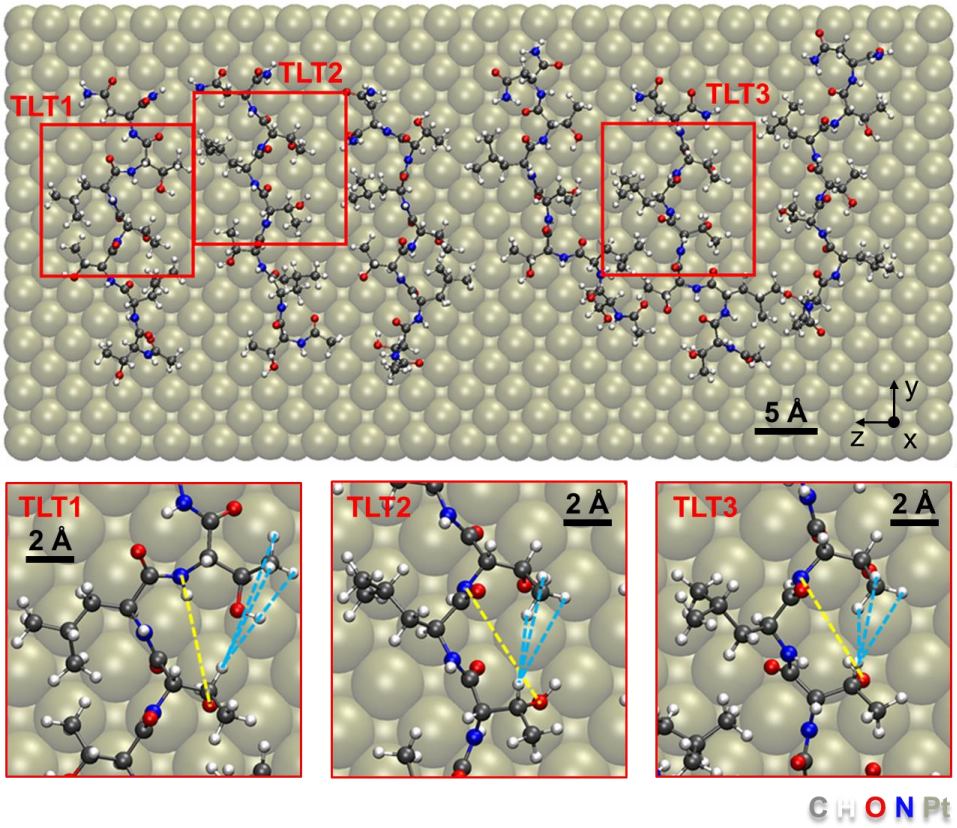

	TLT1	TLT2	TLT3	Ideal ST-turn	NOESY expectation
D (N-O)/Å	5.4±0.2	5.3±0.3	5.1±0.2	<4	NA
D (H1-H2)/Å	3.7±0.3	3.2±0.3	2.4±0.3	NA	<5

Figure 4.15 Representative snapshots of the first layer of peptides on Pt-{100} surface after relaxation in the simulation of perpendicular β-sheets. A layer of water is between the Pt surface and the peptides but hidden for visual clarity. Three of the six T7 molecules transform from initial β-strands to quasi-ST-turns ("quasi" because of the templating effect of the surface) which are squared in red and labeled as TLT1, 2, 3. The N-O and H1-H2 distances, marked respectively with yellow and blue dashed lines in the zoomed-in snapshots, are shown in the table.

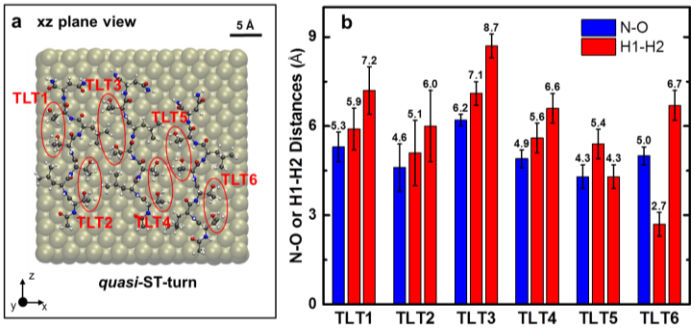

	D (N-O)/Å	D (H1-H2)/Å	
TLT1	5.3±0.5	5.9±0.7	7.2±0.8
TLT2	4.6±0.8	5.1±1.1	6.0±1.2
TLT3	6.2±0.2	7.1±0.4	8.7±0.4
TLT4	4.9±0.3	5.6±0.5	6.6±0.5
TLT5	4.3±0.4	5.4±0.5	4.3±0.4
TLT6	5.0±0.3	2.7±0.4	6.7±0.5
Ideal ST-turn	<4	NA	
NOESY expectation	NA	<5	

Figure 4.16 Preferred conformation of T7 molecules between Pt NCs of a 1-D assembly. (a) Representative quasi-ST-turn conformations of T7 peptides on the Pt-{100} surfaces from figure 3j. (b) Equilibrated N-O and H1-H2 distances in all TLT units labeled in (a). Note that each TLT unit has 1 N-O pair and 2 pairs of H1-H2. Water molecules are for visual clarity.

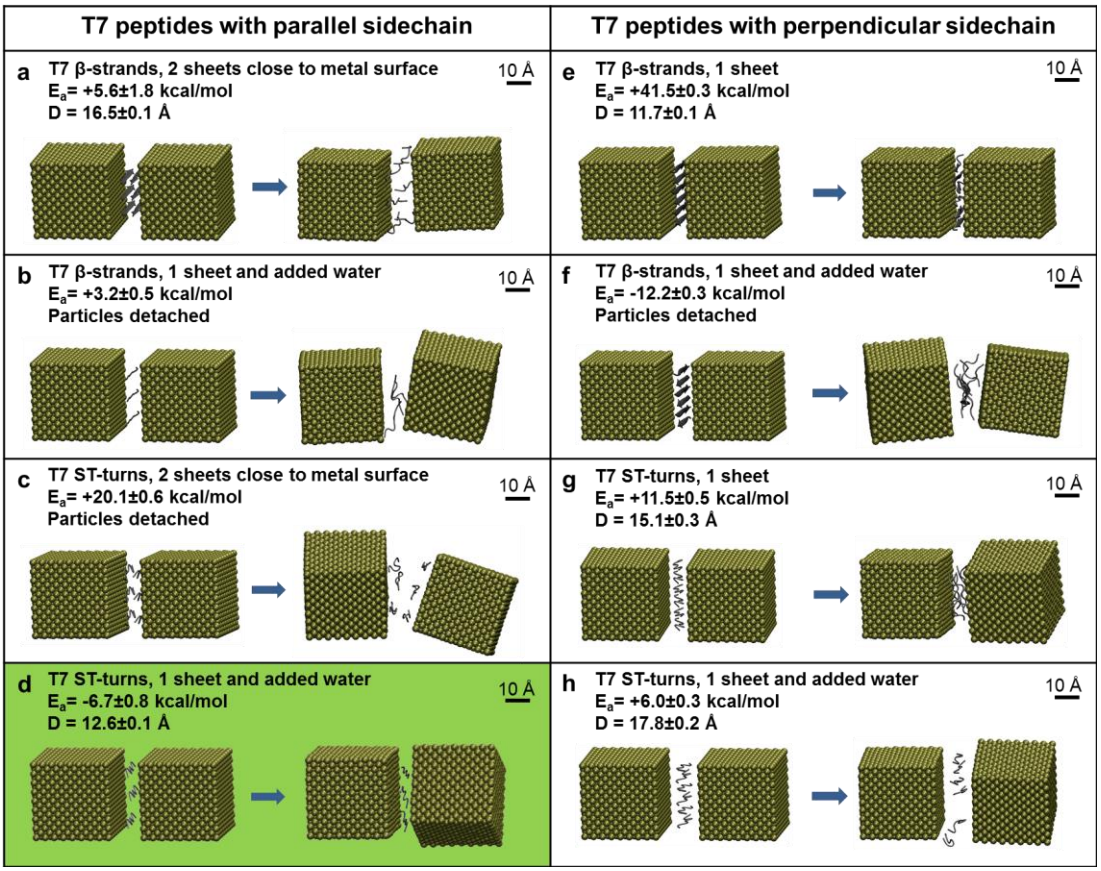

Figure 4.17 Alternative T7 conformations between Pt NCs from the initial to the equilibrated states in the direction of 1D assembly. Each panel shows an entire view

of the system from the initial setup to the equilibrated status (peptides shown as newcartoon representations). Four cases of β-strands as the assumed conformation of intercrystal peptides with either (a,b) parallel or (e,f) perpendicular sidechains to the Pt {100} surfaces, (b,f) with or (a,e) without a layer of water between peptides and NC surfaces are initially put between the two Pt NCs. And four cases of ST-turns as the assumed conformation with (c,d) parallel or (g,h) perpendicular sidechains, (d,h) with or (c,g) without water are initially put between the two Pt NCs. Cases a, b, c, g and h result in both positive adsorption energies and large nanoparticle spacing distances thus are impractical. In e, the intercrystal spacing is reasonable, but the large positive adsorption energy indicates that the system is highly energetically disfavored. In f, the adsorption energy is negative but the two particles detach after the simulation. The only satisfying simulation results are from case d giving an adsorption energy of -6.7 kcal/mol and an intercrystal spacing of 12.6 Å which is consistent with the experimental results of 12.2 Å, cf. Figure 3i. Water molecules are hidden for visual clarity.

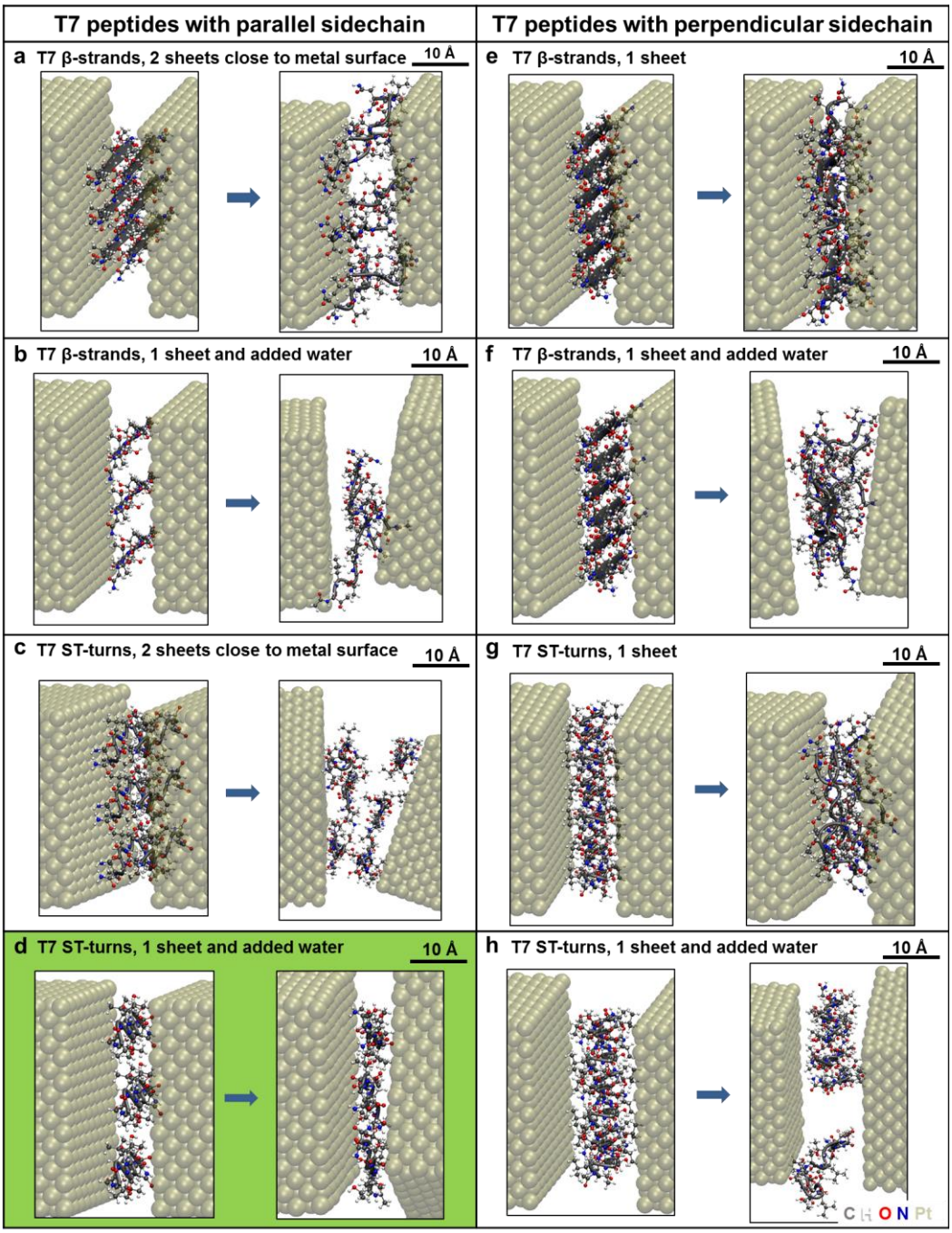

Figure 4.18 Zoom-in snapshots showing the change of alternative T7 conformations between Pt NCs from the initial to the equilibrated states. (a-h) correspond respectively to (a-h) in Figure S15. Peptides are shown as both newcartoon and CPK representations and Pt NCs are shown transparently to avoid peptides being hided by NCs. Water molecules are hidden for visual clarity.

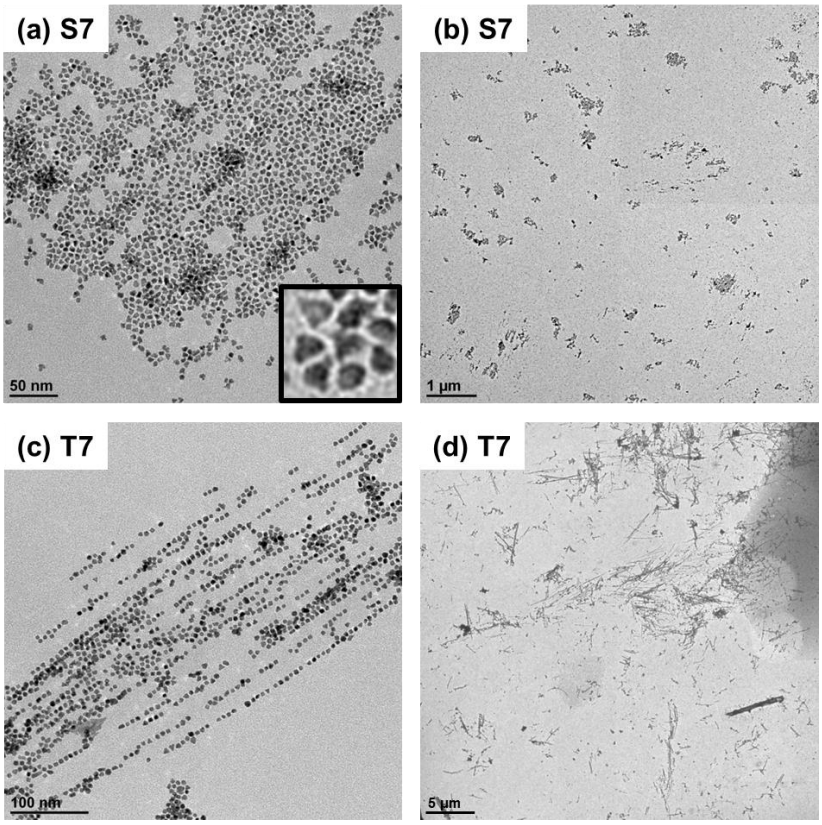

Figure 4.19 ST turns on NC surfaces are necessary for assembly in 800 µg/mL T7. (a,b) S7-covered NCs (synthesized in 30 µg/mL S7) do not assemble. (c,d) T7-covered NCs (synthesized in 10 µg/mL T7) do assemble.

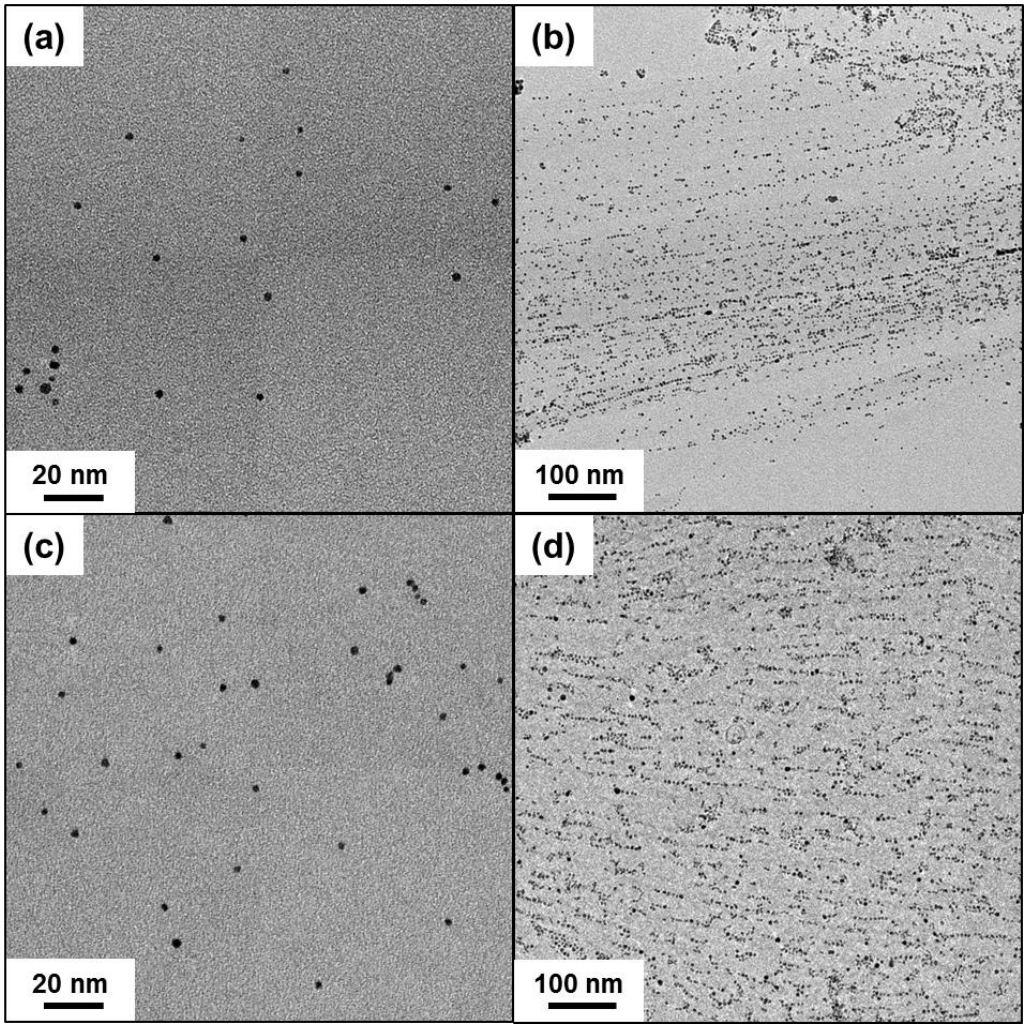

Figure 4.20 The T7 assembly method extended to Au and Pd NC systems. Well-dispersed (a) gold NCs and (c) palladium NCs with uniform sizes are synthesized adopting C-T7 as the surfactant. (b) gold NCs and (d) palladium NCs assembled one-dimensionally in 1000 μg/mL T7.

Adsorption energies of T7 were computed with molecular dynamics simulation to reason NC assembly. (Table 1) The system where the assembly happens is a mechanical system in thermal equilibrium with a heat bath at a fixed temperature, which can be treated as a canonical ensemble. So the distribution will obey Boltzmann distribution. The concentration we have for T7 is m_{T7} = 1000 μg/mL. From

the in-situ Raman, the threshold above which β-sheets will dominate is some number between 200 μg/mL to 800 μg/mL. Here we can approximately take the threshold m_{Th}=500 μg/mL. The molecular weight for T7 is M_{T7}=803.9 g/mol. Thus the concentration of β-strands:

$$c_\beta = \frac{m_{T7} - m_{Th}}{M_{T7}} = 0.622 \text{ mM}$$

The precursor H_2PtCl_6 used in the system is c_{Pt}=1 mM. Since the reducing agent $NaBH_4$ is strong and ascorbic acid is excess so here we take 100% Pt reduced to atoms. Each nanocube synthesized has length of side L_{cube}=6 nm. The lattice parameter for Pt fcc is a=0.3921 nm, where each fcc lattice have 4 atoms. From Figure 2d, the length of the T7 ST-turn projected on Pt{100} is l=2.67 nm while the width is w=1.16 nm. The approximate number of T7 ST-turn each nanocube surface can accommodate is:

$$n = \frac{L_{cube}^2}{l \times w} = 11.62$$

The concentration of the available binding sites on nanocubes is:

$$c_{cube} = \frac{6 \times c_{pt} \times n}{4 \times \left(\frac{L_{cube}}{a}\right)^3} = 0.004866 \text{ mM}$$

The adsorption energy for peptide-peptide in β-sheets is $E_{ads(p\text{-}p)}$=-4 kcal/mol and the adsorption energy for perpendicular peptide-Pt(100) is $E_{ads(p\text{-}Pt)}$=-6.5 kcal/mol. T is temperature where T= 300 K. N_A is the Avogadro constant. k is the Boltzmann constant. Thus the Boltzmann distribution for peptide-peptide in β-sheets is:

$$F_{p-p} \propto e^{-\frac{E_{ads(p-p)}}{N_A kT}}$$

The Boltzmann distribution for perpendicular peptide-Pt(100) is:

$$F_{p-Pt} \propto e^{-\frac{E_{ads(p-Pt)}}{N_A kT}}$$

The ratio of the possibility to form peptide-peptide in β-sheets and the possibility to form perpendicular peptide-Pt(100) is:

$$r = \frac{F_{p-p} \times c_\beta}{F_{p-Pt} \times c_{cube}} = \frac{e^{-\frac{E_{p-p}}{N_A kT}} \times c_\beta}{e^{-\frac{E_{p-Pt}}{N_A kT}} \times c_{cube}} = \frac{513}{266.82} = 1.92$$

That means the possibility to form peptide-peptide in β-sheets and the possibility to form perpendicular peptide-Pt(100) are in the same order. Thus at the beginning there are two kinds of dominative units to start with, the β-sheet fragments and nanocubes with perpendicular peptide-Pt(100). As shown in Table 2, starting from those two units, the combinations of the units in *x*-*y* plane is always favored due to the formation of more H-bonds at the joint. In *y* direction they can form close packed assembly as well as assemblies with spaces between two adjacent NCs. The β-sheet between the two NCs will stabilize the space and still linearize the NCs on both sides of the space. The β-sheet forms a rail which also allows NCs to move in *y* direction. (Figure S8) In *x* direction, there is no close packed assembly since there will always be β-sheet structure between the NCs, which makes the 1-D NC assemblies (along *y* direction) have certain spaces in *x* direction. Those β-sheets also block the movement of NC in *x* direction. In *z* direction, there are no H-bonds formed when the units combined to provide a driving force, making assembly in *z* direction not favored.

Table 1: Molecular dynamics simulation of T7 adsorption energies

	Peptide-Peptide	Peptide-Nanocube		NC-Peptide-NC
		Perpendicular β-sheets	Parallel β-sheets	
E_{ads} (kcal/mol per T7)	-4.0±0.3	-6.5±0.3	-1.1±0.2	-6.7±0.8

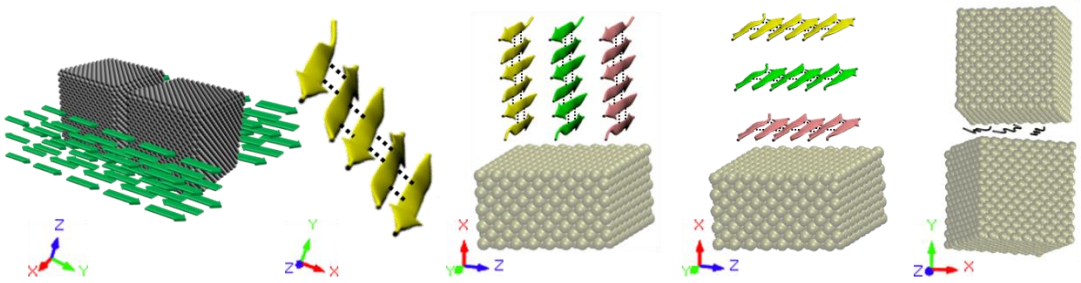

Table 2: Schematics of different situations from start units to 1-D assembly

Start unit	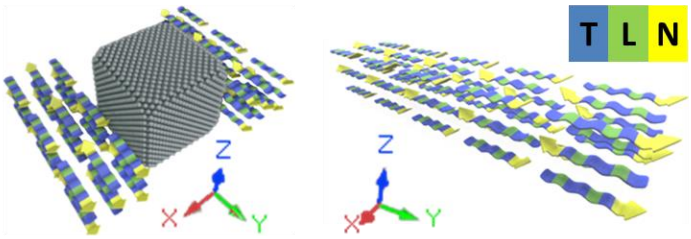
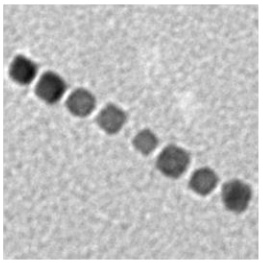	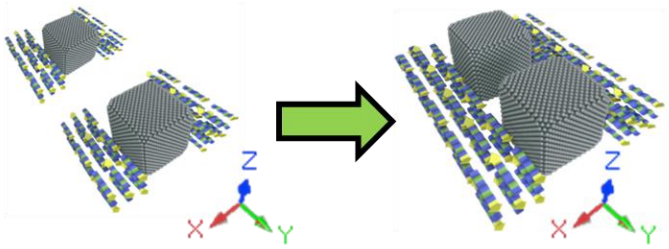
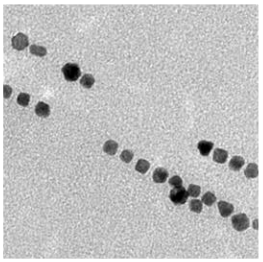	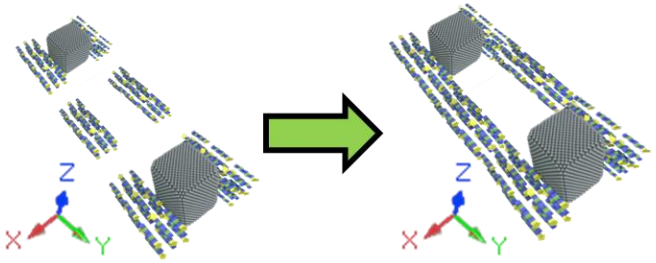
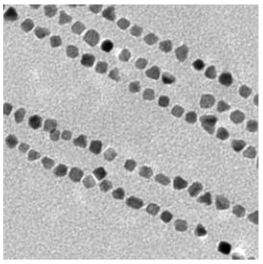	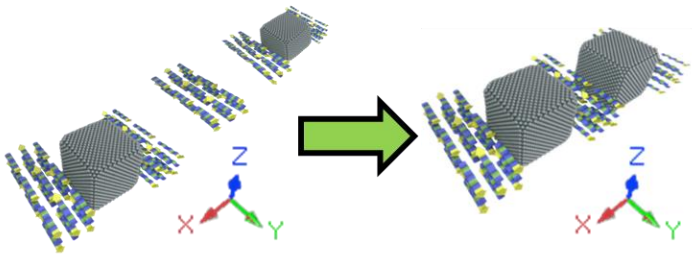
No driving force along *z*	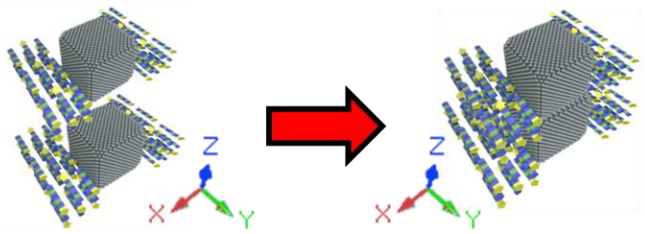

To investigate the uncertainty in r subjected to different sources of uncertainty in the inputs, we performed the sensitivity analysis. The threshold m_{Th} may vary from 200 μg/mL to 800 μg/mL. Pt reduced to atoms from precursor may vary from 70% to

100%. The L_{cube} may vary from 5 nm to 7 nm. l may vary from 2.5 nm to 2.8 nm. w may vary from 1.0 nm to 1.3 nm. $E_{ads(p\text{-}p)}$ may vary from -4.3 kcal/mol to -3.7 kcal/mol. $E_{ads(p\text{-}Pt)}$ may vary from -6.8 kcal/mol to -6.2 kcal/mol. T may vary from 297 K to 317 K. Taking all the uncertainty into account the range of r will vary from 0.13 to 17.75 and in this range it is still valid for our assumption to have 2 start units.

Summary

The origin of the peptide recognition toward Pt {100} surfaces was investigated by examining the influence of the secondary structures to the selective binding of T7, a Pt {100} specific peptide, and its variants to Pt facets in a colloidal system. The ST-turn has been identified and experimentally proven to be the effective motif to create the binding contrast for the recognition process. The fact that the ST-turn structures of differently structured peptide molecules can lead to selective binding of Pt{100} shows unambiguously its predominant role in guiding molecular recognition. We also demonstrated that with a higher concentration, higher pH and lower temperature, T7 will spontaneously change from ST-turn to β-sheet. Importantly, we have further utilized the interaction between the peptides with ST-turn on the {100} facets of Pt and peptides with β-sheet in the solution to assemble the synthesized nanocubes into 1-D assembly along specific <100> direction. The demonstration that one can indeed understand and hence control the organic-inorganic interfacial interactions through rational molecular design based on the secondary structures of

the peptides opens up opportunities for fundamental interfacial studies that can benefit wide range of applications. The self-assembly of non-close-packed shaped nanoparticle groupings that adopt specific interparticle orientations and spaces in such a long range will also benefit wide range of applications. And by rationally designing T7-like peptides, the assembly strategy can be easily extended to other metal NC systems.

Experimental Details

Peptide synthesis and characterization: Peptides were synthesized according to the fmoc solid phase peptide synthesis protocol using a CS 336X synthesizer (C S Bio). The N and C-terminals were acylated and amidated respectively to reduce interfering electrostatic interactions. In brief, 0.5 g fmoc-rink amide MBHA resin was deprotected using piperidine/DMF (1:4), followed by coupling amino acids in reverse order using fmoc-protected amino acid/HBTU/DIEA/DMF (2.5:2.25:5:90.25). Then, the N-terminal was acylated using $(Ac)_2O$/DIEA/DMF (5:5:90). Finally, the peptides were cleaved from the resin using phenol/H_2O/TIPS/TFA (5:5:2:88). The cleavage solution was drained into diethyl ether to precipitate peptides. The peptides were washed with diethyl ether five times and dried under vacuum. Then, they were dissolved in water and freeze-dried.

Synthesis of Pt NCs: Pt NCs were synthesized under aqueous condition using the

strong reducing agent $NaBH_4$ to induce the nucleation and the weak reducing agent ascorbic acid to sustain the growth in the presence of peptides. In a typical synthesis, 0.5 mL H_2PtCl_6 stock solution (10 mM), 1 mL peptide stock solution (0.1 mg/mL), and 3.3 mL H_2O were premixed in a glass vial. The $NaBH_4$ solution (80 mM) and ascorbic acid solution (100 mM) were freshly prepared each time before use. 0.15 ml ascorbic acid solution was first introduced into the reaction vial, followed by the injection of 0.05 mL $NaBH_4$ solution. The final solution volume was 5 mL, and the final concentrations were 1 mM for H_2PtCl_6, 20 μg/mL for peptide, 3 mM for ascorbic acid, and 0.8 mM for $NaBH_4$, respectively. The NCs were allowed to grow 30 minutes before transmittance electron microscopy (TEM) characterization.

For reactions with varying peptide concentrations, different amounts of peptide stock solutions were introduced to meet the desired peptide concentrations, and the water amount was adjusted correspondingly to maintain the final solution volume at 5 mL. For time dependent studies of NC morphology evolution, aliquots of reaction solutions were taken out at required time points to prepare TEM samples immediately.

FTIR sample preparation: To maintain the structure of aqueous peptides to the greatest extent for FTIR spectroscopy, the peptide solution was rapidly dropped into liquid ethane that has been cooled to liquid nitrogen temperature (freezing rate on the order of 1000000 K/sec) by droplets about 2 μL in volume. The fast cooling prevents the formation of ice crystals so the peptide structure is maintained thanks to no phase

segregation. Then freeze-drying was conducted with a -8 ºC sample temperature in primary drying to avoid the structure change. Secondary drying was conducted with sample in room temperature. The powder then was mixed with KBr and a transparent pellet was pressed for FTIR spectroscopy.

Models in theoretical calculation: Models of T7 peptides, Pt-{100} extended surfaces, Pt nanocubes, and water molecules (TIP3P model) were prepared in all-atom resolution using the Materials Studio software. The peptides were protected by acyl and amide groups at the N and C terminal ends respectively, and contained no ionic groups as in the experimental studies. T7 peptides of specific secondary structures (β-strand and ST-turn) were constructed according to the structure definitions. Models of Pt-{100} extended surfaces were prepared from multiples of unit cells. The dimensions of Pt-{100} surface slabs applied in calculating adsorption energy of single ST-turn T7 peptide, perpendicular 6×6 β-sheets, parallel 6×6 β-sheets, and 6×6 β-sheets pointing towards Pt surface were 39.2360×27.4652×15.6944 $Å^3$, 74.5484×35.3124×15.6944 $Å^3$, 31.3888×35.3124×15.6944 $Å^3$, and 74.5484×31.3888×15.6944 $Å^3$, respectively. The model of a Pt nanocube was prepared using an 8×8×8 supercell of a Pt-{100} unit cell and removal of periodic conditions, corresponding to a side length of 31.3888 Å.

Simulation protocol: The molecular dynamic simulation were carried out in the NPT ensemble using the Nanoscale Molecular Dynamics program (NAMD) and the

CHARMM-INTERFACE force filed. This force field is equivalent to the CHARMM-METAL force field[51] with extended parameters for other compounds,[52,53] based on a classical Hamiltonian and thermodynamically consistent Lennard-Jones (LJ) parameters for fcc metals[52] embedded in the CHARMM force field. The temperature and pressure was maintained at 293.15K and 1 atm, which are in consistent with experimental conditions.

Adsorption energy calculation in Peptide-peptide interaction. The method of determining the adsorption energy between two β-strands in the β-sheet can be illustrated in Figure 4.21. Two simulation boxes containing the same amount of water molecules and peptides were constructed. The only difference between the two boxes was the equilibrated peptide structure, that in the first box the peptides adopted β-sheet structure and in the second box peptides were random coil. Multiple runs were conducted by using β-sheet consisting of different number of β-strands (N=2 to 10) in the first simulation box. The adsorption energy of each run can be determined by Figure S 4.21, and the final adsorption energy was the average of adsorption energies from each run.

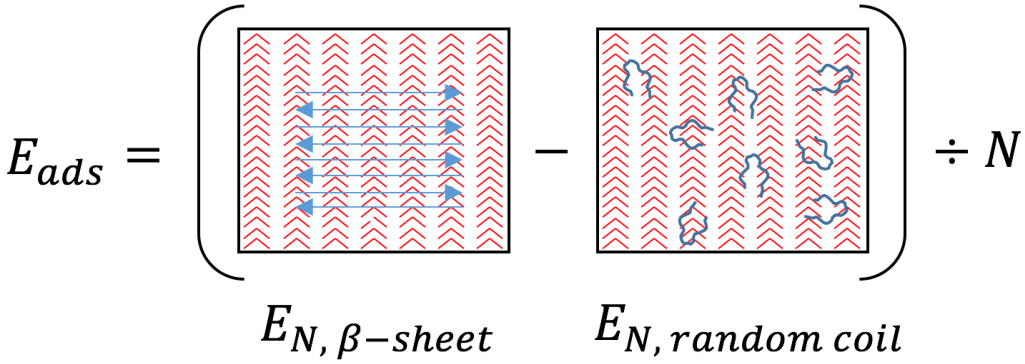

Figure 4.21 Method of determining the adsorption energy between two β-strands in the β-sheet. Number of water molecules and peptides are all same in the two simulation boxes. Here, N=8 is taken as an example.

Adsorption energy calculation in Peptide-platinum interaction. The adsorption energies between peptides and Pt-{100} extended surfaces or Pt nanocubes involved in this paper were determined by the two-box method.[54] Similar to the method of exploring interactions between peptides in the previous section, the same number of peptide T7 of same initial structures, same slab of Pt-{100} extended surface or Pt nanocubes, and same amount of water molecules were put into 2 simulation boxes. In the calculations of peptides adsorption on Pt-{100} extended surfaces, the only difference between the two simulation boxes was that the peptides was put close to the surface in one simulation box (E_{close} box), while in the other box the peptide was put far from the surface (E_{far} box), shown as Figure 4.22a. The distance between peptide and surface should be large enough (>15 Å) to avoid any interaction between them. As for exploring interactions between peptides and Pt nanocubes, the E_{close} box and E_{far} box were all the same except that in the E_{close} box the two Pt nanocubes were

put close to each other with the sandwiched pepetides, and in the E_{far} box the two nanocubes were separated with peptides adsorbed on them, as indicated in Figure 4.22b. Again, in the E_{far} box the two nanocubes should be far enough from each other to avoid any interaction between them, and the distance between the adsorbed peptides should be at least 15 Å. After the two systems were equilibrated, the adsorption energy can be determined as the subtraction of two energies (Figure 4.22). The final reported adsorption energies were normalized by the peptide number, in a unit of kcal/mol per peptide T7.

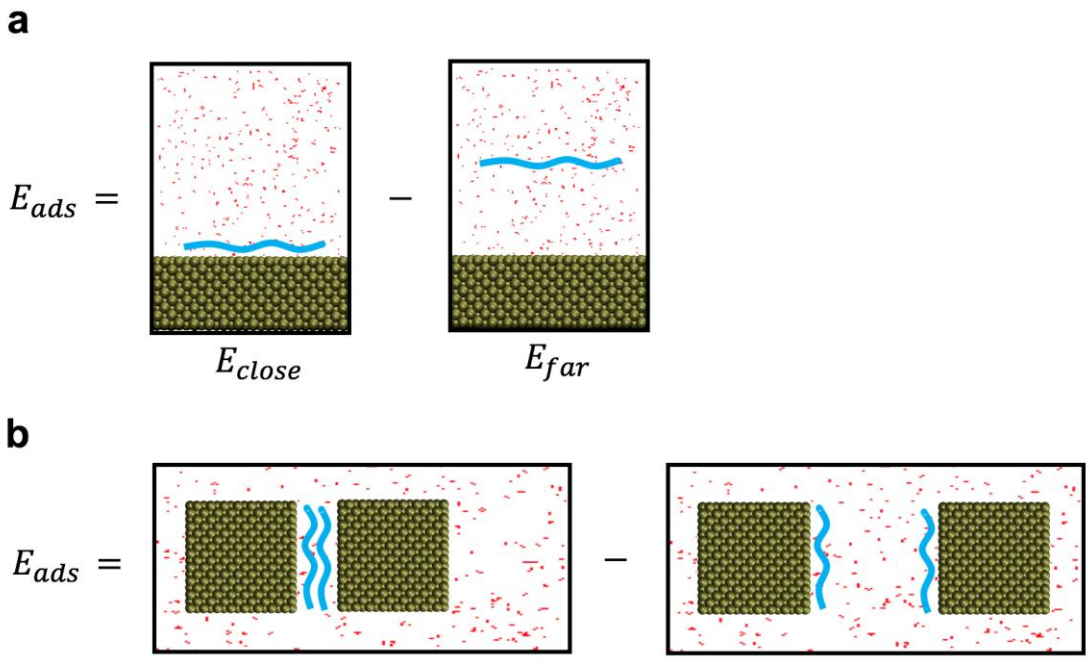

Figure 4.22 Method of determining the adsorption energy between peptides and (a) Pt-{100} extended surfaces and (b) peptides and Pt nanocubes. The blue curves indicate the peptides. Note that in (b), if two peptide sheets were put between the two Pt nanocubes, then each sheet came with one nanocube when they were separated. If there was only one peptide sheet between the two Pt nanocubes and they cannot be

evenly divided, e.g. three peptides, then one peptide was attached to one nanocube and the other two peptides were attached to another nanocube when separated.

Calculations of distances. Distances between β-strands backbones, N-O and H1-H2 in ST-turns, and Pt nanocubes were carried out using the Visual Molecular Dynamics (VMD) software.[55] The distance between β-strands backbones can be determined by averaging out the distances between the hydrogen bonded nitrogen atom from -NH- in one β-strands and carbon atom from -CO- group in another β-strands along the equilibrated trajectories. Similarly, the calculations of N-O and H1-H2 distances applied the same method. To determine the Pt nanocubes inter-particle space, average distances between randomly selected middle-position atoms of the sandwiched peptides to the two nanocubes facets were first calculated at each equilibrated trajectory snapshot, then the final reported distances between the two Pt nanocubes were the sum of the two distances averaged along the whole equilibrated trajectories.

References

1. Tao, A. R., Habas, S., & Yang, P. (2008). Shape control of colloidal metal nanocrystals. *small*, *4*(3), 310-325.
2. Xia, Y., Xiong, Y., Lim, B., & Skrabalak, S. E. (2009). Shape‐controlled synthesis of metal nanocrystals: Simple chemistry meets complex physics?. *Angewandte Chemie International Edition*, *48*(1), 60-103.
3. Yin, Y., & Alivisatos, A. P. (2005). Colloidal nanocrystal synthesis and the organic-inorganic interface. *Nature*, *437*(7059), 664.
4. Whaley, S. R., English, D. S., Hu, E. L., Barbara, P. F., & Belcher, A. M. (2000). Selection of peptides with semiconductor binding specificity for directed nanocrystal assembly. *Nature*, *405*(6787), 665.
5. Ruan, L., Zhu, E., Chen, Y., Lin, Z., Huang, X., Duan, X., & Huang, Y. (2013). Biomimetic synthesis of an ultrathin platinum nanowire network with a high twin density for enhanced electrocatalytic activity and durability. *Angewandte Chemie International Edition*, *52*(48), 12577-12581.
6. Ruan, L., Ramezani-Dakhel, H., Chiu, C. Y., Zhu, E., Li, Y., Heinz, H., & Huang, Y. (2013). Tailoring molecular specificity toward a crystal facet: a lesson from biorecognition toward Pt {111}. *Nano letters*, *13*(2), 840-846.
7. Naik, R. R., Stringer, S. J., Agarwal, G., Jones, S. E., & Stone, M. O. (2002). Biomimetic synthesis and patterning of silver nanoparticles. *Nature materials*, *1*(3), 169.
8. Gugliotti, L. A., Feldheim, D. L., & Eaton, B. E. (2004). RNA-mediated

metal-metal bond formation in the synthesis of hexagonal palladium nanoparticles. *Science*, *304*(5672), 850-852.

9. Chung, W. J., Kwon, K. Y., Song, J., & Lee, S. W. (2011). Evolutionary screening of collagen-like peptides that nucleate hydroxyapatite crystals. *Langmuir*, *27*(12), 7620-7628.
10. Chiu, C. Y., Li, Y., Ruan, L., Ye, X., Murray, C. B., & Huang, Y. (2011). Platinum nanocrystals selectively shaped using facet-specific peptide sequences. *Nature chemistry*, *3*(5), 393-399.
11. Aizenberg, J. (2010). New nanofabrication strategies: inspired by biomineralization. *MRS bulletin*, *35*(4), 323-330.
12. Vallee, A., Humblot, V., & Pradier, C. M. (2010). Peptide interactions with metal and oxide surfaces. *Accounts of Chemical Research*, *43*(10), 1297-1306.
13. Slocik, J. M., & Naik, R. R. (2010). Probing peptide–nanomaterial interactions. *Chemical Society Reviews*, *39*(9), 3454-3463.
14. Sanchez, C., Arribart, H., & Guille, M. M. G. (2005). Biomimetism and bioinspiration as tools for the design of innovative materials and systems. *Nature materials*, *4*(4), 277.
15. Liang, M. K., Deschaume, O., Patwardhan, S. V., & Perry, C. C. (2011). Direct evidence of ZnO morphology modification via the selective adsorption of ZnO-binding peptides. *Journal of Materials Chemistry*, *21*(1), 80-89.
16. Gao, B., Arya, G., & Tao, A. R. (2012). Self-orienting nanocubes for the assembly of plasmonic nanojunctions. *Nature nanotechnology*, *7*(7), 433-437.

17. Kuzyk, A., Schreiber, R., Fan, Z., Pardatscher, G., Roller, E. M., Högele, A., ... & Liedl, T. (2012). Dna-based self-assembly of chiral plasmonic nanostructures with tailored optical response. *Nature*, *483*(7389), 311-314.

18. DeVries, G. A., Brunnbauer, M., Hu, Y., Jackson, A. M., Long, B., Neltner, B. T., ... & Stellacci, F. (2007). Divalent metal nanoparticles. *Science*, *315*(5810), 358-361.

19. Polavarapu, L., & Xu, Q. H. (2008). Water-soluble conjugated polymer-induced self-assembly of gold nanoparticles and its application to SERS. *Langmuir*, *24*(19), 10608-10611.

20. Yang, M., Chen, G., Zhao, Y., Silber, G., Wang, Y., Xing, S., ... & Chen, H. (2010). Mechanistic investigation into the spontaneous linear assembly of gold nanospheres. *Physical Chemistry Chemical Physics*, *12*(38), 11850-11860.

21. Warner, M. G., & Hutchison, J. E. (2003). Linear assemblies of nanoparticles electrostatically organized on DNA scaffolds. *Nature materials*, *2*(4), 272.

22. Chen, C. L., Zhang, P., & Rosi, N. L. (2008). A new peptide-based method for the design and synthesis of nanoparticle superstructures: construction of highly ordered gold nanoparticle double helices. *Journal of the American Chemical Society*, *130*(41), 13555-13557.

23. Zhang, X., Lv, L., Ji, L., Guo, G., Liu, L., Han, D., ... & Dong, A. (2016). Self-assembly of one-dimensional nanocrystal superlattice chains mediated by molecular clusters. *J. Am. Chem. Soc*, *138*(10), 3290-3293.

24. Xu, X., Rosi, N. L., Wang, Y., Huo, F., & Mirkin, C. A. (2006). Asymmetric

functionalization of gold nanoparticles with oligonucleotides. *Journal of the American Chemical Society*, *128*(29), 9286-9287.

25. Millstone, J. E., Georganopoulou, D. G., Xu, X., Wei, W., Li, S., & Mirkin, C. A. (2008). DNA-Gold Triangular Nanoprism Conjugates. *Small*, *4*(12), 2176-2180.
26. Yao, L. I. N., Boker, A., He, J., & Sill, K. (2005). Self-directed self-assembly of nanoparticle/copolymer mixtures. *Nature*, *434*(7029), 55.
27. Shenhar, R., Norsten, T. B., & Rotello, V. M. (2005). Polymer‐Mediated Nanoparticle Assembly: Structural Control and Applications. *Advanced Materials*, *17*(6), 657-669.
28. Nie, Z., Fava, D., Kumacheva, E., Zou, S., Walker, G. C., & Rubinstein, M. (2007). Self-assembly of metal-polymer analogues of amphiphilic triblock copolymers. *Nature materials*, *6*(8), 609.
29. Caswell, K. K., Wilson, J. N., Bunz, U. H., & Murphy, C. J. (2003). Preferential end-to-end assembly of gold nanorods by biotin-streptavidin connectors. *Journal of the American Chemical Society*, *125*(46), 13914-13915.
30. Devouard, B., Posfai, M., Hua, X., Bazylinski, D. A., Frankel, R. B., & Buseck, P. R. (1998). Magnetite from magnetotactic bacteria: Size distributions and twinning. *American Mineralogist*, *83*(11), 1387-1398.
31. Lesné, S., Koh, M. T., Kotilinek, L., Kayed, R., Glabe, C. G., Yang, A., ... & Ashe, K. H. (2006). A specific amyloid-[beta] protein assembly in the brain impairs memory. *Nature*, *440*(7082), 352.
32. Hartgerink, J. D., Beniash, E., & Stupp, S. I. (2001). Self-assembly and

mineralization of peptide-amphiphile nanofibers. *Science*, *294*(5547), 1684-1688.

33. Pouget, E., Dujardin, E., Cavalier, A., Moreac, A., Valéry, C., Marchi-Artzner, V., ... & Artzner, F. (2007). Hierarchical architectures by synergy between dynamical template self-assembly and biomineralization. *Nature materials*, *6*(6), 434-439.
34. Alivisatos, P. (2004). The use of nanocrystals in biological detection. *Nature biotechnology*, *22*(1), 47.
35. Ramezani-Dakhel, H., Ruan, L., Huang, Y., & Heinz, H. (2015). Molecular Mechanism of Specific Recognition of Cubic Pt Nanocrystals by Peptides and of the Concentration‐Dependent Formation from Seed Crystals. *Advanced Functional Materials*, *25*(9), 1374-1384.
36. Daura, X. (2006). Molecular dynamics simulation of peptide folding. *Theoretical Chemistry Accounts*, *116*(1-3), 297-306.
37. Sewald, N., & Jakubke, H. D. (2015). *Peptides: chemistry and biology*. John Wiley & Sons.
38. Ramírez-Alvarado, M., Blanco, F. J., & Serrano, L. (1996). De novo design and structural analysis of a model β-hairpin peptide system. *Nature Structural & Molecular Biology*, *3*(7), 604-612.
39. Honda, S., Yamasaki, K., Sawada, Y., & Morii, H. (2004). 10 residue folded peptide designed by segment statistics. *Structure*, *12*(8), 1507-1518.
40. Fesinmeyer, R. M., Hudson, F. M., & Andersen, N. H. (2004). Enhanced hairpin stability through loop design: the case of the protein G B1 domain hairpin.

Journal of the American Chemical Society, *126*(23), 7238-7243.

41. Cochran, A. G., Skelton, N. J., & Starovasnik, M. A. (2001). Tryptophan zippers: Stable, monomeric β-hairpins. *Proceedings of the National Academy of Sciences*, *98*(10), 5578-5583.
42. Blanco, F. J., Rivas, G., & Serrano, L. (1994). A short linear peptide that folds into a native stable β-hairpin in aqueous solution. *Nature Structural & Molecular Biology*, *1*(9), 584-590.
43. Brahms, S., & Brahms, J. (1980). Determination of protein secondary structure in solution by vacuum ultraviolet circular dichroism. *Journal of molecular biology*, *138*(2), 149-178.
44. Yang, H., Yang, S., Kong, J., Dong, A., & Yu, S. (2015). Obtaining information about protein secondary structures in aqueous solution using Fourier transform IR spectroscopy. *Nature protocols*, *10*(3), 382.
45. Baldwin, R. L., & Rose, G. D. (1999). Is protein folding hierarchic? I. Local structure and peptide folding. *Trends in biochemical sciences*, *24*(1), 26-33.
46. Anfinsen, C. B. (1973). Principles that govern the folding of protein chains. *Science*, *181*(4096), 223-230.
47. Williams, R. W., & Dunker, A. K. (1981). Determination of the secondary structure of proteins from the amide I band of the laser Raman spectrum. *Journal of Molecular Biology*, *152*(4), 783-813.
48. Gutteridge, A., & Thornton, J. M. (2005). Understanding nature's catalytic toolkit. *Trends in biochemical sciences*, *30*(11), 622-629.

49. Nam, K. T., Shelby, S. A., Choi, P. H., Marciel, A. B., Chen, R., Tan, L., ... & Kisielowski, C. (2010). Free-floating ultrathin two-dimensional crystals from sequence-specific peptoid polymers. *Nature materials*, *9*(5), 454.

50. Fraser, R. D. B., MacRae, T. P., Stewart, F. H. C., & Suzuki, E. (1965). Poly-L-alanylglycine. *Journal of molecular biology*, *11*(4), 706IN1-712.

51. Feng, J., Pandey, R. B., Berry, R. J., Farmer, B. L., Naik, R. R., & Heinz, H. (2011). Adsorption mechanism of single amino acid and surfactant molecules to Au {111} surfaces in aqueous solution: design rules for metal-binding molecules. *Soft Matter*, *7*(5), 2113-2120.

52. Heinz, H., Vaia, R. A., Farmer, B. L., & Naik, R. R. (2008). Accurate simulation of surfaces and interfaces of face-centered cubic metals using 12-6 and 9-6 Lennard-Jones potentials. *The Journal of Physical Chemistry C*, *112*(44), 17281-17290.

53. Heinz, H., Lin, T. J., Kishore Mishra, R., & Emami, F. S. (2013). Thermodynamically consistent force fields for the assembly of inorganic, organic, and biological nanostructures: the INTERFACE force field. *Langmuir*, *29*(6), 1754-1765.

54. Heinz, H. (2010). Computational screening of biomolecular adsorption and self‐assembly on nanoscale surfaces. *Journal of computational chemistry*, *31*(7), 1564-1568.

55. Humphrey, W., Dalke, A., & Schulten, K. (1996). VMD: visual molecular dynamics. *Journal of molecular graphics*, *14*(1), 33-38.